



저작자표시-비영리-변경금지 2.0 대한민국

이용자는 아래의 조건을 따르는 경우에 한하여 자유롭게

- 이 저작물을 복제, 배포, 전송, 전시, 공연 및 방송할 수 있습니다.

다음과 같은 조건을 따라야 합니다:



저작자표시. 귀하는 원저작자를 표시하여야 합니다.



비영리. 귀하는 이 저작물을 영리 목적으로 이용할 수 없습니다.



변경금지. 귀하는 이 저작물을 개작, 변형 또는 가공할 수 없습니다.

- 귀하는, 이 저작물의 재이용이나 배포의 경우, 이 저작물에 적용된 이용허락조건을 명확하게 나타내어야 합니다.
- 저작권자로부터 별도의 허가를 받으면 이러한 조건들은 적용되지 않습니다.

저작권법에 따른 이용자의 권리는 위의 내용에 의하여 영향을 받지 않습니다.

이것은 [이용허락규약\(Legal Code\)](#)을 이해하기 쉽게 요약한 것입니다.

[Disclaimer](#)

공학박사 학위논문

제일원리를 이용한 다중산 이온계
전이금속 화합물 기반 이차전지전극
소재 및 물분해촉매에 관한 연구

**First Principles Study on the Polyanion based
Transition Metal Oxide Materials as Rechargeable
Battery Electrode and Water Oxidation Catalyst**

2017 년 2 월

서울대학교 대학원

재료공학부

박 인 철

Abstract

First Principles Study on the Polyanion based Transition Metal Oxide Materials as Rechargeable Battery Electrode and Water Oxidation Catalyst

Park, Inchul

Department of Materials Science and Engineering

College of Engineering

Seoul National University

Endless increase in energy demand and the depletion of fossil fuels has accelerated progress in the development of alternative energy sources. To cope the ever-growing energy requirements and to provide sustainable energy, large energy storage systems (ESS) have become an important research area in recent years. Among the various candidates, chemical energy storage systems are regarded as the optimum choice for these applications because of the pollution free operation, the high throughput efficiency, and the flexible power and energy characteristics to meet different functions, long cycle life, and low maintenance. In this context, the search for new

materials for ESSs based on cost-effective redox couples has been intensively implemented in recent years. For better materials for ESSs, my main interest is in designing new polyanionic compounds with desirable properties.

In **Chapter 2**, introduce a new method to remove anti-site defects in olivine crystals for lithium ion battery (LIB), using electrochemical charge carrier injection process at a room temperature. The Fe anti-site defects in LiFePO_4 are effectively reduced by the electrochemical recombination of Li/Fe anti-sites. The healed crystal structure of lithium iron phosphate recovers its specific capacity and high-power capabilities. In this chapter, various configuration of anti-site defects and its recombination mechanisms are discussed.

In **Chapter 3**, a new iron-based mixed polyanion compound, $\text{Na}_4\text{Fe}_3(\text{PO}_4)_2(\text{P}_2\text{O}_7)$, for NIBs is introduced. Structural characterization of a newly synthesized mixed-polyanion compound with three-dimensional Na pathways was performed using combined X-ray and neutron diffraction studies. The electrode exhibited average potential ~ 3.2 V (vs. Na^+/Na) and energy density of 320 Wh kg^{-1} . Also, the reversible electrode operation was found from ion-exchanged sample of $\text{Li}_3\text{NaFe}_3(\text{PO}_4)_2(\text{P}_2\text{O}_7)$ in Li-ion cells. The electrode delivers about 92 % of theoretical capacity ($\sim 140 \text{ mAh g}^{-1}$) with an average voltage of 3.4 V (vs. Li^+/Li). This research firstly suggested that a significant opportunity exists to explore new open-framework electrodes for NIBs with high electrochemical performances by combination of $(\text{PO}_4)^{3-}$ and $(\text{P}_2\text{O}_7)^{4-}$ polyanions.

In **Chapter 4**, investigated the electrochemical mechanism of $\text{Na}_x\text{Fe}_3(\text{PO}_4)_2(\text{P}_2\text{O}_7)$ ($1 \leq x \leq 4$) in Na-ion cells using first principles calculations and experiments. I discovered that the de/sodiation of the $\text{Na}_x\text{Fe}_3(\text{PO}_4)_2(\text{P}_2\text{O}_7)$ electrode occurs *via* one-phase reaction with a reversible $\text{Fe}^{2+}/\text{Fe}^{3+}$ redox reaction. The electrode accompanies an exceptionally small volumetric change of less than 4% during electrochemical cycling, which is attributed to the open framework of polyanion compounds with flexible P_2O_7 dimer in the structure. Although the structural distortion in $\text{NaFe}_3(\text{PO}_4)_2(\text{P}_2\text{O}_7)$ reduces Na de/intercalation kinetics at the last step of charge resulting in incomplete utilization of Na ($\sim 82\%$ of theoretical capacity), high rate capability was confirmed with the negligible capacity reduction from C/20 to C/5. Also, stable cycle retention up to 20 cycles were confirmed. *In situ* X-ray diffraction (XRD) and differential scanning calorimetry (DSC) revealed that the partially charged electrodes, $\text{Na}_x\text{Fe}_3(\text{PO}_4)_2(\text{P}_2\text{O}_7)$ ($1 \leq x \leq 4$), are thermally stable up to 530°C . The understanding of electrochemical mechanism of $\text{Na}_x\text{Fe}_3(\text{PO}_4)_2(\text{P}_2\text{O}_7)$ ($1 \leq x \leq 4$) shown here will give a direction to the optimization of the new $\text{Na}_4\text{Fe}_3(\text{PO}_4)_2(\text{P}_2\text{O}_7)$ electrode for Na rechargeable batteries.

In **Chapter 5**, introduce an amorphous cobalt phyllosilicate (ACP) with layered crystalline motif prepared by a simple room-temperature precipitation as a new efficient OER catalyst for hydrogen fuel; this material exhibits a remarkably low overpotential (η) among cobalt-based catalysts as well as long-term stability. A structural investigation based on X-ray absorption spectroscopy and Fourier-transform infrared spectra reveals that the silicate layer maintains its structure after

electrolysis. In addition, density functional theory calculations indicate that the layered crystalline motif in the ACP, which is similar to that in CoOOH, is responsible for the OER mechanism; however, the local environment of the active site is significantly modulated by the silicate group, leading to a substantial reduction in the OER η . This work proposes that a new material group of phyllosilicates could be efficient OER catalysts and that tuning of the catalytic activity by controlling the redox-inert groups can pave an explored avenue toward the design of novel high-performance catalysts.

Keywords : Energy Storage, Lithium rechargeable battery, Sodium rechargeable battery, water oxidation catalyst, polyanion compound, Density Functional Theory

Student Number : 2012-30157

Table of Contents

Abstract	i
Table of Contents	v
List of Figures	viii
List of Tables	xviii
Chapter 1. Introduction	1
1.1 General Background	1
1.2 Lithium ion Battery system	2
1.3 Sodium ion Battery system	3
1.4 Electrochemical Water Splitting for Hydrogen Fuel	5
1.5 References	8
Chapter 2. Anti-site reordering in LiFePO₄ using charge carrier injection	15
2.1 Introduction	15
2.2 Experimental	18
2.3 Results and Discussion	21
2.4 Conclusion	44
2.5 References	45

Chapter 3. New iron-Based Mixed-Phosphate Cathodes for Lithium and Sodium Rechargeable Batteries	49
3.1 Introduction	49
3.2 Experimental	52
3.3 Results and Discussion	56
3.4 Conclusion	81
3.5 References	82
Chapter 4. Understanding the electrochemical mechanism of the new iron-based mixed-phosphate $\text{Na}_4\text{Fe}_3(\text{PO}_4)_2(\text{P}_2\text{O}_7)$ in a Na rechargeable battery	86
4.1 Introduction	86
4.2 Experimental	89
4.3 Results and Discussion	93
4.4 Conclusion	127
4.5 References	128
Chapter 5. Amorphous cobalt phyllosilicate with layered crystalline motifs as water oxidation catalyst	131
5.1 Introduction	131
5.2 Experimental	134
5.3 Results and Discussion	141

5.4 Conclusion	192
5.5 References	193
Chapter 6. Summary	201
Abstract in Korean	203

List of Figures

Figure 2-1. Calculated formation energy of anti-site defect in LiFePO_4 and its configuration corresponding to the distance between Li^+ on Fe^{2+} site and Fe^{2+} on Li^+ site. Near anti-site defect has lower formation energy. (a) Edge-shared anti-site defect with the lowest formation energy (about 390 meV) (b), (c) Corner-shared anti-site defect with the formation energy of about 490 meV.

Figure 2-2. Formation energies for 45 different vacancy-Fe defect configurations of the single-phase $\text{Li}_{1-x}\text{FePO}_4$ from first principles calculations. The most stable energy is observed in (a) the corner-shared configuration and the second most stable configurations is shown as (b) the edge-shared configuration.

Figure 2-3. Energy curve and schematics of the Fe-Li cation site re-ordering process during discharge. The black line is the Fe/Li recombination route with no charge carrier injection. The red line is the hypothetical Fe/Li recombination route with a charge carrier (electron) injection. Schematics 1 – 4 schematics are Fe-Li cation site re-ordering processes at each point.

Figure 2-4. The $15 \sim 55^\circ$ high resolution powder diffraction patterns of prepared by hydrothermal synthesis

Figure 2-5. (a) Magnified (200) peak of high resolution powder diffraction patterns of the prepared samples. (b) Rietveld refinement results of solid-solution $\text{Li}_{0.9}\text{FePO}_4$. The inset figure is an SEM image of micro-size $\text{Li}_{0.9}\text{FePO}_4$.

Figure 2-6. Rietveld refinement of hydrothermally prepared LiFePO_4 .

Figure 2-7. Rietveld refinement result of electrochemically treated LiFePO_4 .

Figure 2-8. Defect characterization (a) Black: GITT result of $\text{Li}_{0.9}\text{FePO}_4$, red: quasi-OCV result of $\text{Li}_{0.9}\text{FePO}_4$, blue: quasi-OCV of conventional LiFePO_4 . (b) Lattice parameters, volume and anti-site ratio of prepared samples. The detailed Rietveld refinement results are provided in supporting Figure S3 – S5. (c) *a*-lattice parameter

change as a function of anti-site ratio. The inset figure is shown the unit cell volume change as a function of anti-site ratio. Red line : trend line, blue line : confidence band, green line : prediction band. The interval coverage probability is set as 95 %. The star points symbolized stand for hydrothermal synthesized LiFePO_4 and electrochemically treated LiFePO_4 . The data are taken from references 20, 30, 40 and 42. (d) FT-IR results of prepared samples PO_4^{3-} spectra.

Figure 2-9. Lattice parameter with change modification with anti-site ratio at room temperature. Red line: trend line, blue line: confidence band, green line: prediction band. The interval coverage probability is set as 95 %. This figure used reference number 25, 35, 47 and 49.

Figure 2-10. The electrochemical profile of solid-solution $\text{Li}_{0.9}\text{FePO}_4$ at C/100. The 1st discharge profile showed unexpected high polarization, however, the 2nd profile did not show overpotential during charging/discharging.

Figure 2-11. $15 \sim 55^\circ$ XRD patterns of prepared by solid-state method samples (left) and magnified (200) peak of samples (right). red line: (200) peak of LiFePO_4 , blue line: (200) peak of FePO_4 . All samples are well synthesized without remarkable impurities.

Figure 2-12. SEM image of prepared LiFePO_4 . (a) Hydrothermal synthesis LiFePO_4 (b) 380°C heated hydrothermal synthesis $\text{Li}_{0.9}\text{FePO}_4$ (c) 600°C solid-state synthesis LiFePO_4 (d) 380°C heated solid-state 600°C synthesis $\text{Li}_{0.9}\text{FePO}_4$.

Figure 2-13. (a) First charge/discharge profile at C/200 of electrochemically treated micro- LiFePO_4 and hydrothermally grown micro- LiFePO_4 . (b) C-rate capability of electrochemically treated nano- LiFePO_4 (red) and conventional nano- LiFePO_4 (black).

Figure 3-1. Thermogravimetric analysis and differential scanning calorimetry (TGA/DSC) of the precursor used for the solid-state synthesis of $\text{Na}_4\text{Fe}_3(\text{PO}_4)_2(\text{P}_2\text{O}_7)$.

Figure 3-2. (a) Schematic representation of $\text{Na}_4\text{Fe}_3(\text{PO}_4)_2(\text{P}_2\text{O}_7)$. (b) Rietveld refinement of the neutron diffraction patterns of $\text{Na}_4\text{Fe}_3(\text{PO}_4)_2(\text{P}_2\text{O}_7)$. The observed

and calculated intensities are represented by the red markers and the black solid line, respectively. The bottom blue line represents the difference between the observed and calculated patterns. Bragg positions for $\text{Na}_4\text{Fe}_3(\text{PO}_4)_2(\text{P}_2\text{O}_7)$ are represented as green markers, and the NaFePO_4 (~4%) impurity is shown as purple markers. (c) The 3D sodium diffusion paths in the $\text{Na}_4\text{Fe}_3(\text{PO}_4)_2(\text{P}_2\text{O}_7)$ structure.

Figure 3-3. Detailed schematics of the Na channel along the b - c plane and the diphosphate connection between the $[\text{Fe}_3\text{P}_2\text{O}_{13}]_\infty$ layers are presented in (a). The sodium sites along the a - and b -axes in the structure of $\text{Na}_4\text{Fe}_3(\text{PO}_4)_2(\text{P}_2\text{O}_7)$ are shown in (b) and (c), respectively. The four different Na sites in the structure of $\text{Na}_4\text{Fe}_3(\text{PO}_4)_2(\text{P}_2\text{O}_7)$ are shown in (d).

Figure 3-4. *In-situ* high-temperature X-ray diffraction (XRD) patterns of $\text{Na}_4\text{Fe}_3(\text{PO}_4)_2(\text{P}_2\text{O}_7)$ in the temperature range of 25–650°C under an Ar atmosphere. The NaFePO_4 peaks start to significantly evolve above 550°C.

Figure 3-5. Calculated main diffusion motion along the b -axis as illustrated in (a) and (b). (c) The activation barrier of sodium from one Na1 site to another Na1 site.

Figure 3-6. (a) Galvanostatic charge/discharge profiles of $\text{Na}_4\text{Fe}_3(\text{PO}_4)_2(\text{P}_2\text{O}_7)$ under a C/40 rate and the calculated average voltage at each region. The inset shows the dQ/dV curve of initial charge/discharge profiles. (b) Cycle performance of a Na cell under C/40 and C/20 rates.

Figure 3-7. XRD patterns of $\text{Na}_x\text{Fe}_3(\text{PO}_4)_2(\text{P}_2\text{O}_7)$ ($x = 1, 4$).

Figure 3-8. Mössbauer spectra of $\text{Na}_x\text{Fe}_3(\text{PO}_4)_2(\text{P}_2\text{O}_7)$ ($x = 1, 4$).

Figure 3-9. Integrated spin as a function of integration radius around Fe in $\text{Na}_{4-x}\text{Fe}_3(\text{PO}_4)_2(\text{P}_2\text{O}_7)$ ($x = 0, 3$).

Figure 3-10. TGA/DSC analysis of the desodiated phase of $\text{NaFe}_3(\text{PO}_4)_2(\text{P}_2\text{O}_7)$.

Figure 3-11. *In-situ* high-temperature XRD patterns of $\text{NaFe}_3(\text{PO}_4)_2(\text{P}_2\text{O}_7)$ for a temperature range of 25–650°C under an Ar atmosphere.

Figure 3-12. (a) XRD patterns of $\text{Li}_3\text{NaFe}_3(\text{PO}_4)_2(\text{P}_2\text{O}_7)$. The reference sodium phase of $\text{Na}_4\text{Fe}_3(\text{PO}_4)_2(\text{P}_2\text{O}_7)$ is represented below. (b) Calculated voltage and galvanostatic charge/discharge profiles of the Li cell under a C/20 rate at 298 K and calculated voltage profiles; (c) cyclability of the Li-ion cell under C/5 at 333 K. (d) The rate capability of $\text{Li}_3\text{NaFe}_3(\text{PO}_4)_2(\text{P}_2\text{O}_7)$ in the Li-ion cell.

Figure 4-1. (a) Rietveld refinement of $\text{Na}_4\text{Fe}_3(\text{PO}_4)_2(\text{P}_2\text{O}_7)$ using XRD. A schematic representation of $\text{Na}_4\text{Fe}_3(\text{PO}_4)_2(\text{P}_2\text{O}_7)$ is illustrated in the inset. (b) Galvanostatic charge/discharge profiles of $\text{Na}_4\text{Fe}_3(\text{PO}_4)_2(\text{P}_2\text{O}_7)$ in a Na-ion cell at the C/20 rate. The inset presents the cycle performance at various C-rates (C/20, C/10, and C/5).

Figure 4-2. (a) Scanning electron microscopy (SEM) and (b) transmission electron microscopy (TEM) images of $\text{Na}_4\text{Fe}_3(\text{PO}_4)_2(\text{P}_2\text{O}_7)$ showing that the primary particle sizes are about 100 – 200 nm and that the crystallinity is good.

Figure 4-3. (a) *Ex situ* XRD patterns of $\text{Na}_4\text{Fe}_3(\text{PO}_4)_2(\text{P}_2\text{O}_7)$ in a Na-ion cell during the charge/discharge process. Amplified XRD patterns in the 2θ range of 8 to 19° are illustrated in (b).

Figure 4-4. X-ray diffraction (XRD) patterns of $\text{Na}_x\text{Fe}_3(\text{PO}_4)_2(\text{P}_2\text{O}_7)$ ($1 \leq x \leq 4$) powder samples synthesized by chemical desodiation.

Figure 4-5. (a) *a*, (b) *b*, (c) *c* lattice parameters and (d) lattice volume change of $\text{Na}_x\text{Fe}_3(\text{PO}_4)_2(\text{P}_2\text{O}_7)$ as a function of Na composition (*x*).

Figure 4-6. (a) *a*, (b) *b*, (c) *c* lattice parameters, and (d) lattice volume change of $\text{Na}_x\text{Fe}_3(\text{PO}_4)_2(\text{P}_2\text{O}_7)$ as a function of Na composition (*x*). The black, blue, and red rectangle markers represent the lattice parameters of *ex situ* electrode samples during the initial charge, discharge, and second charge, respectively.

Figure 4-7. DFT formation energies of $\text{Na}_x\text{Fe}_3(\text{PO}_4)_2(\text{P}_2\text{O}_7)$ at various configurations of *x*.

Figure 4-8. (a) Local structure schematics of $\text{Na}_x\text{Fe}_3(\text{PO}_4)_2(\text{P}_2\text{O}_7)$ around Fe sites and integrated spin as a function of integration radius around Fe in $\text{Na}_x\text{Fe}_3(\text{PO}_4)_2(\text{P}_2\text{O}_7)$ ((b) $x = 4$, (c) $x = 3$, (d) $x = 2$, and (e) $x = 1$).

Figure 4-9. Structure schematics of $\text{Na}_x\text{Fe}_3(\text{PO}_4)_2(\text{P}_2\text{O}_7)$ at (a) $x = 2$ and (b) $x = 1$ from first principles calculations.

Figure 4-10. (a) Rietveld refinement of $\text{NaFe}_3(\text{PO}_4)_2(\text{P}_2\text{O}_7)$ using ND. (b) Local structure schematics around Fe1 and P(3) – O – P(4) bond angle comparison table as a function of Na content (x) in $\text{Na}_x\text{Fe}_3(\text{PO}_4)_2(\text{P}_2\text{O}_7)$ from ND analysis.

Figure 4-11. XANES spectra during first (a) charge and (b) discharge. XANES spectra of the as-prepared state and of the end of charge and end of discharge states are shown in (c).

Figure 4-12. X-ray absorption near-edge structure (XANES) spectra of the $\text{Na}_x\text{Fe}_3(\text{PO}_4)_2(\text{P}_2\text{O}_7)$ electrode during the second charge.

Figure 4-13. XANES spectra of chemically prepared $\text{Na}_x\text{Fe}_3(\text{PO}_4)_2(\text{P}_2\text{O}_7)$ ($1 \leq x \leq 4$) samples.

Figure 4-14. PITT measurements of $\text{Na}_4\text{Fe}_3(\text{PO}_4)_2(\text{P}_2\text{O}_7)$ during (a) charging and (b) discharging.

Figure 4-15. Differential scanning calorimetry (DSC) spectra of $\text{Na}_x\text{Fe}_3(\text{PO}_4)_2(\text{P}_2\text{O}_7)$ ($1 \leq x \leq 4$).

Figure 4-16. *In situ* high-temperature XRD of desodiated powder samples of $\text{Na}_x\text{Fe}_3(\text{PO}_4)_2(\text{P}_2\text{O}_7)$ at (a) $x = 3.2$, (b) $x = 2.72$, (c) $x = 2.21$, and (d) $x = 1.71$.

Figure 4-17. Phase diagram of $\text{Na}_x\text{Fe}_3(\text{PO}_4)_2(\text{P}_2\text{O}_7)$ ($1 < x < 4$).

Figure 5-1. Crystal structure of phyllosilicate. (Inset: two kinds of phyllosilicate)

Figure 5-2. SEM image of ACP prepared by co-precipitation method

Figure 5-3. Powder X-ray diffraction patterns of the ACP and heated ACP by hydrothermal method.

Figure 5-4. Fourier transform infrared (FT-IR) of the ACP and heated ACP by hydrothermal method.

Figure 5-5. The variation of the Co/Si ratio with different precursor ratio.

Figure 5-6. Powder X-ray diffraction patterns of ACP with different precursor ratio.

Figure 5-7. Polarization curves of ACP in 1 M KOH electrolyte with different precursor ratio.

Figure 5-8. Schematic representation of CoOOH and ACP structure. CoOOH and the ACP consist of edge-sharing CoO_6 octahedra. The silicate layer of ACP features Si-deficient structure in contrast with the ideal phyllosilicate structure composed of hexagonal tetrahedral ring.

Figure 5-9. Structure of cobalt phyllosilicate $\text{Co}_3\text{Si}_2\text{O}_9\text{H}_4$. $\text{Co}_3\text{Si}_2\text{O}_9\text{H}_4$ consist of cobalt hydroxide layer and perfect hexagonal silicate chains at one sides of cobalt layers. The other side is terminated with hydrogen. Co, Si, O, and H are shown as blue, green, red and white spheres, respectively.

Figure 5-10. Structure of cobalt phyllosilicate $\text{Co}_3\text{Si}_4\text{O}_{12}\text{H}_2$. $\text{Co}_3\text{Si}_4\text{O}_{12}\text{H}_2$ consist of cobalt hydroxide layer and perfect hexagonal silicate chains at both sides of cobalt layers. Co, Si, O, and H are shown as blue, green, red and white spheres, respectively.

Figure 5-11. Calculated structure of ACP ($\text{Co}_3\text{Si}_3\text{O}_{12}\text{H}_6$). From reported structures of cobalt phyllosilicate ($\text{Co}_3\text{Si}_2\text{O}_9\text{H}_4$ and $\text{Co}_3\text{Si}_4\text{O}_{12}\text{H}_2$), we predicted structural motif of ACP with Co:Si:O = 1:1:4 using DFT calculations. Hydrogen atoms added to maintain Co oxidation state as 2+. (a) Homogeneous model with Si deficient chain at both side of cobalt hydroxide layer shows much stable energy (7.5 meV per atom) than that of (b) Inhomogeneous model with Si deficient chain at one side of cobalt hydroxide layer. Co, Si, O, and H are shown as blue, green, red and white spheres, respectively.

Figure 5-12. Oxygen evolution properties of prepared cobalt based catalysts. (a) *iR*-corrected polarization curves in 1 M KOH at scan rate of 10 mV s^{-1} and (c) the

corresponding tafel plots. (b) OER overpotentials required for 10 mA cm^{-2} . (d) The plots of differences in current density ($\Delta j = j_a - j_c$) at 1.05 V vs. RHE against scan rate due to evaluate electrochemical double layer capacitance. (e) Long-term stability of the ACP performed under constant current density at $j = 10 \text{ mA cm}^{-2}$ for 24 h.

Figure 5-13. Powder X-ray diffraction pattern of CoOOH nanoplates.

Figure 5-14. SEM image of CoOOH nanoplates.

Figure 5-15. Powder X-ray diffraction pattern of Co₃O₄ nanoparticles.

Figure 5-16. SEM image of Co₃O₄ nanoparticles.

Figure 5-17. (a) XANES cobalt K-edge spectra of the as-prepared ACP and the after 1st CV ACP. For comparison, CoO and LiCoO₂ also shown for reference samples of Co²⁺ and Co³⁺, respectively. (b) Oscillations of the EXAFS spectra and (c) Fourier transformed k^3 -weighted EXAFS spectra of the as-prepared, after electrolysis ACP and CoOOH. (d) Comparison between experimental Fourier transformed EXAFS spectrum (dotted line) of the ACP after electrolysis and theoretical fit (red line).

Figure 5-18. Comparison between experimental Fourier transformed EXAFS spectrum (dotted line) of the CoOOH nanoplates and theoretical fit (red line).

Figure 5-19. Comparison between experimental Fourier transformed EXAFS spectrum (dotted line) of as-prepared ACP and theoretical fit (red line).

Figure 5-20. Surface structures of OER active surface from (a, c) CoOOH surface and (b, d) ACP surface. (a) Side view for the CoOOH (**1014**) surface which is most active surface for OER. (b) Side view for the CoOOH surface with similar atomic configuration to the CoOOH (**1014**) surface. The ACP surface has longer interlayer distance than CoOOH. Top view for active surface of (c) CoOOH and (d) ACP shows active sites for OER. Co, Si, O, and H are shown as blue, green, red and white spheres, respectively. To clarify, we reveal only topmost atoms.

Figure 5-21. Crystal structure of (a) CoOOH and (b) ACP; Cleavage lines are given in black. Note that the (**1014**) surface is the most OER active surface from CoOOH.

Cleavage line for ACP has similar atomic configuration to the CoOOH ($10\bar{1}4$) surface and silicate tetrahedron is preserved.

Figure 5-22. Surface termination of ACP surface (model 1) corresponds to the potential. (a) Surface phase diagram as a function of applied potential for ACP surface model. Stable surface structures with adsorbates corresponds to applied potential: (b) with 1 monolayer (ML) of co-adsorbed H_2O (below 1.1 V), (c) with 1 ML of OH and 3/4 ML of H (from 1.1 V to 1.8 V), and (d) with 1 ML of OH and 1/4 ML (above 1.8 V). To clarify, only topmost atoms are shown.

Figure 5-23. Surface structures of another surface of ACP model (model 2). Different from ACP surface model in the Figure 5-20, silicates are adsorbed at the bridge site rather than terminal site. (a) Side view for the CoOOH surface with similar atomic configuration to the CoOOH ($10\bar{1}4$) surface. (b) Top view for active surface of ACP shows active sites for OER. Co, Si, O, and H are shown as blue, green, red and white spheres, respectively. To clarify, only topmost atoms are shown.

Figure 5-24. Surface termination of another ACP surface (model 2) corresponds to the potential. (a) Surface phase diagram as a function of applied potential for ACP surface model. Stable surface structures with adsorbates corresponds to applied potential: (b) with 1 monolayer (ML) of co-adsorbed H_2O (below 1.1 V), (c) with 1 ML of OH and 3/4 ML of H (from 1.1 V to 1.8 V), and (d) with 1 ML of OH and 1/4 ML (above 1.8 V). To clarify, only topmost atoms are shown.

Figure 5-25. DFT calculation results for OER at CoOOH and ACP surfaces. (a) Theoretical overpotentials for OER of plausible sites. Some bridge site on ACP surface show much lower overpotential than active sites of CoOOH. (b) Free energy landscape for OER at 1.23 V (ideal potential for OER). Black, cyan and blue line indicate free energy of ACP bridge 1 site, CoOOH bridge site, and CoOOH terminal site, respectively. Comparison of the structures for OOH^* forming step (rate-determining step for these cases) at the (c) ACP bridge 1 site, (d) CoOOH bridge site,

and (e) CoOOH terminal site. More adjustment in bond-length at the ACP surface lower the OER overpotential.

Figure 5-26. OER pathways and calculated minimum overpotential for terminal 1 site on ACP surface (model 1). Deprotonation from terminal 1 site needs more than 2.33 eV, therefore overpotential for OER is higher than 1.1 V.

Figure 5-27. OER pathways and calculated minimum overpotential for terminal 2 site on ACP surface (model 1). Vacancy at terminal 2 site is unstable, therefore OH* adsorption step is spontaneous with $\Delta G = -2.62$ eV. Because $\Delta G1 + \Delta G2$ is -1.54 eV, overpotential is higher than 2.00 V. ($\Delta G3 + \Delta G4 = 6.46$ eV)

Figure 5-28. OER pathways and calculated minimum overpotential for bridge 1 site on ACP surface (model 1). All the reaction steps at bridge 1 site are stable, therefore OER at bridge 1 site has much lower overpotential than other sites on ACP surface or CoOOH surface.

Figure 5-29. OER pathways and calculated minimum overpotentials for bridge 2 site on ACP surface (model 1). Different from that of bridge 1 site, deprotonation from bridge 2 site needs higher than 1.92 eV, therefore overpotential for OER is higher than 0.69 V.

Figure 5-30. OER pathways and calculated minimum overpotential for terminal 3 site on ACP surface (model 2). Deprotonation from terminal 3 site needs high potential of 1.94 V, thus overpotential for OER is higher than 0.71 V.

Figure 5-31. OER pathways and calculated minimum overpotential for terminal 4 site on ACP surface (model 2). OER from terminal 4 site shows moderate overpotential of 0.54 V which is similar to the CoOOH case.

Figure 5-32. OER pathways and calculated minimum overpotential for bridge 3 site on ACP surface (model 2). OER at bridge 3 site shows overpotential of 0.81 V. Rate determining step is OOH* formation step because silicate group does not stabilize OOH* step while does stabilize OH* and O* steps.

Figure 5-33. OER pathways and calculated minimum overpotential for bridge 4 site on ACP surface (model 2). Different from that of bridge 3 site, deprotonation from bridge 4 site needs higher than 2.12 eV, therefore overpotential for OER is higher than 0.89 V.

List of Tables

Table 2-1. Detailed structural information of hydrothermally prepared LiFePO_4 analyzed by Rietveld refinement.

Table 2-2. Detailed structural information of solid-solution $\text{Li}_{0.9}\text{FePO}_4$ analyzed by Rietveld refinement.

Table 2-3. Detailed structural information of electrochemically treated LiFePO_4 analyzed by Rietveld refinement.

Table 3-1. The detailed data for the structural refinement of $\text{Na}_4\text{Fe}_3(\text{PO}_4)_2(\text{P}_2\text{O}_7)$ using ND patterns.

Table 3-2. Sodium vacancy activation barriers in the $\text{Na}_4\text{Fe}_3(\text{PO}_4)_2(\text{P}_2\text{O}_7)$ structure.

Table 3-3. Lattice parameters of $\text{Na}_x\text{Fe}_3(\text{PO}_4)_2(\text{P}_2\text{O}_7)$ ($x = 4, 1$).

Table 3-4. Quadruple splitting, isomer shift values, and the ratio of each iron site in $\text{Na}_x\text{Fe}_3(\text{PO}_4)_2(\text{P}_2\text{O}_7)$ ($x = 4, 1$).

Table 3-5. Volumetric energy density of iron-based polyanion compounds.

Table 4-1. Schematic representations of $\text{Na}_4\text{Fe}_3(\text{PO}_4)_2(\text{P}_2\text{O}_7)$ and order of sodium extraction from the structure of $\text{Na}_x\text{Fe}_3(\text{PO}_4)_2(\text{P}_2\text{O}_7)$ ($1 \leq x \leq 4$).

Table 4-2. Detailed structural information of $\text{NaFe}_3(\text{PO}_4)_2(\text{P}_2\text{O}_7)$ analyzed by Rietveld refinement of the ND pattern.

Table 4-3. Bond valence parameters of each atom in $\text{Na}_x\text{Fe}_3(\text{PO}_4)_2(\text{P}_2\text{O}_7)$ ($x = 1, 4$).

Table 5-1. Element ratio of ACP prepared by Co/Si precursor ratio 3:4.

Table 5-2. Element ratio of ACP prepared by Co/Si precursor ratio 3:2.

Table 5-3. Element ratio of ACP prepared by Co/Si precursor ratio 3:3.

Table 5-4. Element ratio of ACP prepared by Co/Si precursor ratio 3:5.

Table 5-5. Structural parameters of the theoretically fitted FT-EXAFS in Figure 5-17d.

Chapter 1. Introduction

1.1 General Background

Continuous increase of energy demand and exhaustion of fossil fuel concerns accelerate developments of alternative energy such as photovoltaic power generation, wind power generation, hydroelectric power generation, geothermal power generation. In this respect, large-scale energy storage is an important issue in dealing with the generation and demand of uneven energy.¹ The largest technology group of the energy storage system (ESS) is chemical storage systems such as batteries and hydrogen fuel. It efficiently stores electricity in chemical substances and can release reversibly on demand. Generally, chemical energy storage has many desirable features including non-polluting operation, high reciprocating efficiency, and flexible power and energy characteristics to satisfy different functions, long cycle life, and low maintenance. Chemical energy storage systems store energies through a redox reaction of a material. Simple transition metal oxide materials have been extensively studied as redox active materials for chemical energy storage (See below for explanation of each system). However, since the types of transition metal oxides are limited, it is difficult to satisfy various needs such as cost, stability, appropriate oxidation-reduction potential. In this regard, polyanionic transition metal oxide compounds have been extensively studied as an important group of potential redox-active materials for chemical energy storage systems due to their chemical diversity.²⁻⁴

1.2 Lithium ion Battery system

Lithium ion battery (LIB) system is one of the most promising ESS. LIB stores electric energy while lithium ions deintercalates from the cathode materials.⁵ At the same time, transition metal ions in the cathode material are reduced. Important properties of LIB such as energy density, stability, and power are determined by the composition and the framework of the transition metal containing material.⁶⁻⁸ Simple metal oxides materials were intensively investigated. Simple metal oxide materials exhibit high energy density but low safety and cyclability disadvantages. Otherwise, lithium ion phosphate (LFP), which is the one of the promising polyanion-based transition metal oxide electrode material for LIB, shows promising electrochemical properties for applying a large scale energy storage system.⁹⁻¹² Theoretically, the LFP could release and insert Li ion on their crystal structure with a theoretical gravimetric energy density of 580 Wh kg⁻¹(theoretical capacity of ~ 169 mAh g⁻¹, Fe^{2+/3+} redox voltage of 3.42 V (vs. Li/Li⁺)) through the 1-D channels being along the [010] direction of crystal structure (Pnma).¹³ However, in practice, the Li-Fe cation site exchange defect (anti-site) in Li diffusion channel always forms with 1 ~ 5 % ratio depending on synthesise route, resulting in denying LFP to reach at a desired energy and power density.⁷ For example, the presence of 0.1 % anti-site ratio in micro size LFP makes statically its energy density to almost half of original value and reduces ionic conductivity with two or three orders.¹⁵ Since the nano-sizing or post crystal structural treatment on LFP has been widely applied to avoid immobile Fe anti-site effect, these approaches cannot completely get rid of the anti-site effects from LFP

because anti-site still remains under 1% in their structure.^{15,17} In addition, the nano-synthesis leads to other problems, such as lowering tap density of electrode, generating other surface defects, surface side reaction during cycling and additional cost problem at synthesizing.^{18,19} Therefore, it is difficult for these approaches to be an ultimate solution as satisfying high gravimetric/volumetric energy density and low cost active materials. Chapter 2 in this thesis deals with a new defect control method using an electrochemical procedure at room temperature. By tailoring the local environment around defects according to a strategy suggested by first principles calculations, it was found that the energy level of defects and the activation barrier for recombination could be lowered significantly. Experimental verification with a case study of LiFePO_4 revealed that significant defect annihilation occurred from a structural analysis, which substantially boosted the power capability of the material. In this work, an effective way to reduce Li-Fe defects is proposed using a simple electrochemical treatment at room temperature.

1.3 Sodium ion Battery system

Another promising alternative to conventional LIB is sodium ion battery (NIB) because of the unlimited Na resources and similar electrochemistry to LIB. Furthermore, the electrodes composed of Na guest ion and redox couples based on low cost transition metals such as Fe would be an optimal design for large scale ESSs.²⁻⁴ However, only a limited number of such materials have been reported to date.

Recent studies have identified several important types of potential electrode materials such as layered oxides, Prussian blue analogues and transition metal-free organic electrodes.²⁻⁴ There are numerous researches on layered oxide electrodes.²⁰⁻²³ Although these layered-type materials possess merits such as high capacity and energy density, the large volume change (>10%) during electrochemical cycling and the phase instability of the charged structure are largest obstacles.²⁴⁻²⁵ Also, general sodium layered oxides are very hygroscopic, therefore they exhibit irreversible phase transformation in the air at room temperature.²⁶

The polyanion-based compounds have been extensively studied as an important group of potential electrode materials due to their structural stability and chemical diversity.²⁷ The general structure based on the polyanions provides the structural stability due to the strong X-O (X = P, S, B, Si) covalent bonding in the structure, and the open rigid framework is beneficial for a small volume change upon electrochemical cycling with a fast ionic mobility compared common layered materials. Moreover, its diversity in chemistry in terms of polyanion species, transition metals and the crystal structure offers many opportunities to find new electrode materials with high-performance and low-cost. To date, the search for cost efficient polyanion electrodes has focused on the phosphate, pyrophosphate, fluorophosphates, fluorosulfate and sulfate containing iron-based materials. However, low voltage below 3.0 V is problematic.

In the search for new Na-containing polyanion compounds, there has been another state of the art approach which combines two different polyanions in the

structure, namely, a mixed-polyanion system. This system was firstly examined by pioneering work of A. K. Pahdi *et al.*, and they showed that the combination between two different $\text{Li}_3\text{Fe}_2(\text{PO}_4)_3$ and $\text{Fe}_2(\text{PO}_4)_3$ phases produces new electrode material of $\text{LiFe}_2(\text{SO}_4)_2(\text{PO}_4)$.²⁸ Recent synthesis of new mixed-polyanion compounds, $\text{Na}_7\text{V}_4(\text{P}_2\text{O}_7)_4\text{PO}_4$ and $\text{Na}_3\text{MnPO}_4\text{CO}_3$, showed that variety of combinations may lead to the discovery of a new open crystal framework with promising electrochemical properties.²⁹⁻³⁰

In this thesis, a new mixed-polyanion compounds based on $(\text{PO}_4)^{3-}$ and $(\text{P}_2\text{O}_7)^{4-}$ as well as low cost transition metal redox couples of $\text{Fe}^{2+}/\text{Fe}^{3+}$ were designed. I revealed redox mechanism and diffusion kinetics of a new iron-based mixed-polyanion compound, $\text{Na}_4\text{Fe}_3(\text{PO}_4)_2(\text{P}_2\text{O}_7)$, for the first time using first principles. Detailed researches on this material is discussed in Chapter 3 and Chapter 4.^{14,16}

1.4 Electrochemical Water Splitting for Hydrogen Fuel

Electrochemical water splitting has been viewed as a promising and eco-accommodating way to deal with create hydrogen, a spotless fuel, by keeping away from a reliance on fossil energizes.³¹⁻³⁷ The oxygen evolution reaction (OER) is the bottleneck of the general water splitting reaction in view of the slow multi-electron response and O–O bond formation.³⁸⁻⁴¹ The precious metal based catalysts, for example, RuO_2 and IrO_2 have been broadly considered as prime catalyst for OER due to the superior catalytic activity.⁴²⁻⁴⁶ However, the rarity and the high cost of

precious metals restrict the commercialization of these catalysts; accordingly, tremendous researches for the efficient and inexpensive OER catalyst using non-precious transition metals have proceeded.⁴⁷⁻⁵⁶ Nocera group reported that the Co- or Ni- based materials such as amorphous cobalt phosphates and nickel borates show the comparable performance or outperform that of the precious metal-based catalysts even in neutral and weak basic electrolyte.^{39, 56} Likewise, later researches have revealed that layered metal (oxy)hydroxides can be successful electrocatalysts, among which layered double hydroxides (LDHs) containing Ni, Fe, or Co can show amazingly high OER catalytic activity that can outperform that of precious metal-based catalysts.⁵⁷⁻⁶¹

Unveiling the origin of high catalytic activity in such transition metal based OER catalysts would provide a hint to effectively design new efficient catalysts. While the local environment of the redox active element is highly related with the activity of OER catalysts, studies have proposed that the coordination number of transition metals (MO_x), the local distortion of MO_x and how they are connected (*i.e.* edge-shared or corner-shared) can sensitively influence on the catalytic activity.^{53,62-67} Furthermore, neighboring redox inert elements can alter the redox activity of catalysts, for example, anions such as phosphate and borate enable efficient proton-coupled electron transfer (PCET)⁴⁶⁻⁴⁸, or capping anion species determine the domain size of electrodeposited amorphous catalysts^{62,63,71,72}, significantly affecting the catalysis. Also, in our recent study, it was shown that the phosphate or pyrophosphate group in catalysts such as $Mn_3(PO_4)_2 \cdot 3H_2O$, $LiMnP_2O_7$ and

$\text{Na}_2\text{CoP}_2\text{O}_7$ can offer the structural flexibility stabilizing the transition metal, thus enhances the OER activity,^{53,73,74} indicative of the importance of the relationship between the structure and catalytic properties.

In chapter 5, I report an amorphous cobalt phyllosilicate (ACP) with layered crystalline motif for a new efficient OER catalyst. The ACP catalyst can be prepared using a simple, fast, and low-cost precipitation method at room temperature and exhibits one of the highest OER activities among known cobalt-based catalysts. In our investigation to elucidate the origin of the catalysis, it is revealed that the OER activity stems from the layered crystalline motif in the ACP, which resembles the structure of CoOOH . Nevertheless, silicate groups present in the interlayer space of the layered crystalline motif significantly modulate the local environment of the active sites and substantially reduce the overall OER overpotential (η) compared with that of conventional layered metal (oxy)hydroxides, as demonstrated by density functional theory (DFT) calculations. This finding suggests that structural modulation by introducing redox-inert groups in the layer space of metal (oxy)hydroxides can be a viable strategy to tune the catalytic activity and that transition-metal-based phyllosilicates can be new candidates for low-cost and efficient OER catalysts.

1.5 References

- (1) H. Chen, T. N. Cong, W. Yang, C. Tan, Y. Li, Y. Ding *Prog. Nat. Sci.* **2009**, *19*, 291.
- (2) S.-W. Kim, D.-H. Seo, X. Ma, G. Ceder, K. Kang, *Adv. Energy Mater.* **2012**, *2*, 710-721.
- (3) H. Pan, Y.-S. Hu, L. Chen, *Energy Environ. Sci.* **2013**, *6*, 2338-2360.
- (4) D. Kundu, E. Talaie, V. Duffort, L. F. Nazar, *Angew. Chem. Int. Ed.* **2015**, *54*, 3431-3448.
- (5) M. Armand and J.M. Tarascon, *Nature* **2008**, *451*, 652-657.
- (6) K. Kang and G. Ceder, *Phy. Rev. B*, **2006**, *74*, 094105.
- (7) J. Chen and J. Graetz, *ACS Applied Materials & Interfaces*, **2011**, *3*, 1380-1384.
- (8) G.K.P. Dathar, D. Sheppard, K.J. Stevenson and G. Henkelman, *Chem. Mater.* **2011**, *23*, 4032-4037.
- (9) P. Gibot, M. Casas-Cabanas, L. Laffont, S. Levasseur, P. Carlach, S. Hamelet, J.M. Tarascon and C. Masquelier, *Nat. Mater.* **2008**, *7*, 741-747.
- (10) W. Dreyer, J. Jamnik, C. Guhlke, R. Huth, J. Moškon, and M. Gaberšček, *Nat. Mater.* **2010**, *9*, 448-453.
- (11) T. Sasaki, Y. Ukyo, and P. Novák, *Nat. Mater.* **2013**, *12*, 569-575.
- (12) C. Delacourt, J.M. Tarascon and C. Masquelier, *Nat. Mater.* **2005**, *4*, 54-260.

- (13) A.K. Padhi, K.S. Nanjundaswamy, and J.B. Goodenough, *J. Electrochem. Soc.* **1997**, 144, 1188-1194.
- (14) H. Kim, I. Park, D.-H. Seo, S. Lee, S.-W. Kim, W. J. Kwon, Y.-U. Park, C. S. Kim, S. Jeon, K. Kang, *J. Am. Chem. Soc.* **2012**, 134, 10369-10372.
- (15) R. Malik, D. Burch, M. Bazant, and G. Ceder, *Nano Letters*, **2010**, 10, 4123-4127.
- (16) H. Kim, I. Park, S. Lee, H. Kim, K.-Y. Park, Y.-U. Park, H. Kim, J. Kim, H.-D. Lim, W.-S. Yoon, K. Kang, *Chem. Mater.* **2013**, 25, 3614-3622.
- (17) J. Chen and M.S. Whittingham, *Electrochem. Commun.* **2006**, 8, 855-858.
- (18) C. M. Julien, A. Mauger, and K. Zaghib, *J. Mater. Chem.* **2011**, 21, 9955-9968.
- (19) J. Wang *et al.*, *Nat. Commun.* **2014**, 5.
- (20) N. Yabuuchi, M. Kajiyama, J. Iwatate, H. Nishikawa, S. Hitomi, R. Okuyama, R. Usui, Y. Yamada and S. Komaba, *Nat. Mater.*, **2012**, 11, 512-517.
- (21) B. Mortemard de Boisse, D. Carlier, M. Guignard, C. Delmas, *J. Electrochem. Soc.* **2013**, 150, A569-A574.
- (22) D. Kim, E. Lee, M. Slater, W. Lu, S. Rood, C. S. Johnson, *Electrochem. Commun.* **2012**, 18, 66-69.
- (23) S. -M. Oh, S. -T. Myung, C. S. Yoon, J. Lu, J. Hassoun, B. Scrosati, K. Amine, Y. -K. Sun, *Nano Lett.* **2014**, 14, 1620-1626.
- (24) R. Berthelot, D. Carlier and C. Delmas, *Nat. Mater.*, **2011**, 10, 74-80.

- (25) S. Komaba, N. Yabuuchi, T. Nakayama, A. Ogata, T. Ishikawa and I. Nakai, *Inorg. Chem.*, **2012**, *51*, 6211-6220.
- (26) V. Duffort, E. Talaie, R. Black, and L.F. Nazar, *Chem. Mater.* **2015**, *27*, 2515-2524.
- (27) C. Masquelier and L. Croguennec, *Chem. Rev.* **2013**, *113*, 6552-6591.
- (28) A. K. Padhi, V. Manivannan, J. B. Goodenough, *J. Electrochem. Soc.* **1998**, *145*, 1518-1520.
- (29) S. Y. Lim, H. Kim, J. Chung, J. H. Lee, B. G. Kim, J.-J. Choi, K. Y. Chung, W. Cho, S.-J. Kim, W. A. Goddard, Y. Jung and J. W. Choi, *Proc. Nat. Acad. Sci. U. S. A.*, **2013**, *A111*, 599-604.
- (30) H. Chen, Q. Hao, O. Zivkovic, G. Hautier, L.-S. Du, Y. Tang, Y.-Y. Hu, X. Ma, C. P. Grey, G. Ceder, *Chem. Mater.* **2013**, *25*, 2777-2786.
- (31) Lewis, N. S.; Nocera, D. G. *Proc. Natl. Acad. Sci. U.S.A.* **2006**, *103*, 15729.
- (32) Grätzel, M. *Nature* **2001**, *414*, 338.
- (33) Gust, D.; Moore, T. A.; Moore, A. L. *Acc. Chem. Res.* **2009**, *42*, 1890.
- (34) Swierk, J. R.; Mallouk, T. E. *Chem. Soc. Rev.* **2013**, *42*, 2357.
- (35) Tachibana, Y.; Vayssieres, L.; Durrant, J. R. *Nat. Photonics* **2012**, *6*, 511.
- (36) Kudo, A.; Miseki, Y. *Chem. Soc. Rev.* **2009**, *38*, 253.
- (37) Faunce, T.; Styring, S.; Wasielewski, M. R.; Brudvig, G. W.; Rutherford, A. W.; Messinger, J.; Lee, A. F.; Hill, C. L.; Fontecave, M.; MacFarlane, D. R. *Energy Environ. Sci.* **2013**, *6*, 1074.

- (38) Hurst, J. K. *Science* **2010**, *328*, 315.
- (39) Kanan, M. W.; Nocera, D. G. *Science* **2008**, *321*, 1072.
- (40) Suntivich, J.; May, K. J.; Gasteiger, H. A.; Goodenough, J. B.; Shao-Horn, Y. *Science* **2011**, *334*, 1383.
- (41) Betley, T. A.; Wu, Q.; Van Voorhis, T.; Nocera, D. G. *Inorg. Chem.* **2008**, *47*, 1849.
- (42) Galizzioli, D.; Tantardini, F.; Trasatti, S. *J. Appl. Electrochem.* **1974**, *4*, 57.
- (43) Horkans, J.; Shafer, M. *J. Electrochem. Soc.* **1977**, *124*, 1202.
- (44) Tilley, S. D.; Cornuz, M.; Sivula, K.; Grätzel, M. *Angew. Chem., Int. Ed.* **2010**, *122*, 6549.
- (45) Youngblood, W. J.; Lee, S.-H. A.; Kobayashi, Y.; Hernandez-Pagan, E. A.; Hoertz, P. G.; Moore, T. A.; Moore, A. L.; Gust, D.; Mallouk, T. E. *J. Am. Chem. Soc.* **2009**, *131*, 926.
- (46) Tong, L.; Duan, L.; Xu, Y.; Privalov, T.; Sun, L. *Angew. Chem., Int. Ed.* **2011**, *50*, 445.
- (47) Gorlin, Y.; Jaramillo, T. F. *J. Am. Chem. Soc.* **2010**, *132*, 13612.
- (48) Wang, H.; Lee, H.-W.; Deng, Y.; Lu, Z.; Hsu, P.-C.; Liu, Y.; Lin, D.; Cui, Y. *Nat. Commun.* **2015**, *6*.
- (49) Luo, J.; Im, J.-H.; Mayer, M. T.; Schreier, M.; Nazeeruddin, M. K.; Park, N.-G.; Tilley, S. D.; Fan, H. J.; Grätzel, M. *Science* **2014**, *345*, 1593.
- (50) Kim, J.; Kim, J. S.; Baik, H.; Kang, K.; Lee, K. *RSC Adv.* **2016**, *6*, 26535.

- (51) Lee, S. W.; Carlton, C.; Risch, M.; Surendranath, Y.; Chen, S.; Furutsuki, S.; Yamada, A.; Nocera, D. G.; Shao-Horn, Y. *J. Am. Chem. Soc.* **2012**, *134*, 16959.
- (52) Chemelewski, W. D.; Lee, H.-C.; Lin, J.-F.; Bard, A. J.; Mullins, C. B. *J. Am. Chem. Soc.* **2014**, *136*, 2843.
- (53) Park, J.; Kim, H.; Jin, K.; Lee, B. J.; Park, Y.-S.; Kim, H.; Park, I.; Yang, K. D.; Jeong, H.-Y.; Kim, J. *J. Am. Chem. Soc.* **2014**, *136*, 4201.
- (54) Friebel, D.; Louie, M. W.; Bajdich, M.; Sanwald, K. E.; Cai, Y.; Wise, A. M.; Cheng, M.-J.; Sokaras, D.; Weng, T.-C.; Alonso-Mori, R. *J. Am. Chem. Soc.* **2015**, *137*, 1305.
- (55) Song, F.; Hu, X. *J. Am. Chem. Soc.* **2014**, *136*, 16481.
- (56) Dincă, M.; Surendranath, Y.; Nocera, D. G. *Proc. Natl. Acad. Sci. U.S.A.* **2010**, *107*, 10337.
- (57) Gong, M.; Li, Y.; Wang, H.; Liang, Y.; Wu, J. Z.; Zhou, J.; Wang, J.; Regier, T.; Wei, F.; Dai, H. *J. Am. Chem. Soc.* **2013**, *135*, 8452.
- (58) Long, X.; Li, J.; Xiao, S.; Yan, K.; Wang, Z.; Chen, H.; Yang, S. *Angew. Chem., Int. Ed.* **2014**, *126*, 7714.
- (59) Song, F.; Hu, X. *Nat. Commun.* **2014**, *5*.
- (60) Ma, W.; Ma, R.; Wang, C.; Liang, J.; Liu, X.; Zhou, K.; Sasaki, T. *ACS Nano* **2015**, *9*, 1977.
- (61) Liang, H.; Meng, F.; Cabán-Acevedo, M.; Li, L.; Forticaux, A.; Xiu, L.; Wang, Z.; Jin, S. *Nano Lett.* **2015**, *15*, 1421.

- (62) Kanan, M. W.; Yano, J.; Surendranath, Y.; Dincă, M.; Yachandra, V. K.; Nocera, D. G. *J. Am. Chem. Soc.* **2010**, *132*, 13692.
- (63) Bediako, D. K.; Lassalle-Kaiser, B.; Surendranath, Y.; Yano, J.; Yachandra, V. K.; Nocera, D. G. *J. Am. Chem. Soc.* **2012**, *134*, 6801.
- (64) Zaharieva, I.; Chernev, P.; Risch, M.; Klingan, K.; Kohlhoff, M.; Fischer, A.; Dau, H. *Energy Environ. Sci.* **2012**, *5*, 7081.
- (65) Robinson, D. M.; Go, Y. B.; Mui, M.; Gardner, G.; Zhang, Z.; Mastrogiovanni, D.; Garfunkel, E.; Li, J.; Greenblatt, M.; Dismukes, G. C. *J. Am. Chem. Soc.* **2013**, *135*, 3494.
- (66) Grimaud, A.; Carlton, C. E.; Risch, M.; Hong, W. T.; May, K. J.; Shao-Horn, Y. *J. Phys. Chem. C* **2013**, *117*, 25926.
- (67) Stoerzinger, K. A.; Choi, W. S.; Jeon, H.; Lee, H. N.; Shao-Horn, Y. *J. Phys. Chem. Lett.* **2015**, *6*, 487.
- (68) Bediako, D. K.; Surendranath, Y.; Nocera, D. G. *J. Am. Chem. Soc.* **2013**, *135*, 3662.
- (69) Surendranath, Y.; Kanan, M. W.; Nocera, D. G. *J. Am. Chem. Soc.* **2010**, *132*, 16501.
- (70) Ullman, A. M.; Brodsky, C. N.; Li, N.; Zheng, S.-L.; Nocera, D. G. *J. Am. Chem. Soc.* **2016**, *138*, 4229.
- (71) Risch, M.; Klingan, K.; Ringleb, F.; Chernev, P.; Zaharieva, I.; Fischer, A.; Dau, H. *ChemSusChem* **2012**, *5*, 542.

(72) Farrow, C. L.; Bediako, D. K.; Surendranath, Y.; Nocera, D. G.; Billinge, S. J.
J. Am. Chem. Soc. **2013**, *135*, 6403.

(73) Jin, K.; Park, J.; Lee, J.; Yang, K. D.; Pradhan, G. K.; Sim, U.; Jeong, D.; Jang,
H. L.; Park, S.; Kim, D. *J. Am. Chem. Soc.* **2014**, *136*, 7435.

(74) Kim, H.; Park, J.; Park, I.; Jin, K.; Jerng, S. E.; Kim, S. H.; Nam, K. T.; Kang,
K. *Nat. Commun.* **2015**, *6*.

Chapter 2. Anti-site reordering in LiFePO_4 using charge carrier injection

(The content of this chapter has been published in *Chemistry of Materilas*. Reprinted with permission from [K.-Y Park and I. Park *et al. Chem. Mater.* **2014**, 26 (18) pp. 3545-5351.]. Copyright (2014) American Chemical Society.)

2.1 Introduction

Defects in crystals are an important factor governing the intrinsic properties of materials, such as mechanical strength, electronic conductivity, and mass diffusion rates.¹⁻³ While the concentration of defects in a crystal at a certain temperature and pressure is determined by thermodynamics,⁴⁻⁶ materials synthesized via non-equilibrium routes generally contain higher concentrations of defects. Careful choices of synthesis conditions or post-treatment methods are needed to control the level of defects and to tune the properties of materials.⁷⁻¹⁰ In conventional semiconductor systems, it is known that the type and concentration of defects determine the electronic properties of materials.¹¹⁻¹³ Similarly, in ion mass-transfer systems, they critically affect kinetic properties.¹⁴⁻¹⁶

Defects in a crystal can impede ion transport by blocking diffusion pathways in one- (1-D) or two-dimensional (2-D) ionic conductors¹⁷⁻¹⁹ LiFePO_4 , an important material in batteries, is a good example of this. While it has been considered a promising electrode material²⁰⁻²² due to its stability^{23,24} and relatively high energy

density,^{25,26} kinetic issues arising from the restrictive diffusion pathways for lithium ions and the low electronic conductivity have been problematic.²⁷ In particular, lithium ions can diffuse only through a 1-D tunnel in the crystal. Thus, this diffusion is susceptible to the presence of defects that may block the tunnel.³ Since nano-sizing has been conducted widely for this material, the reduction in diffusion length can partly resolve the low-power problem. However, more importantly, nano-sizing is capable of reducing the detrimental effects of the defects blocking the channel. Malik *et al.* recently revealed that with 0.1% of Li-Fe site exchange in LiFePO₄, ~45% of Li ions are trapped, statistically, between the defects in a 1- μm LiFePO₄ particle. However, this drops significantly, to ~5% in a 100-nm LiFePO₄ particle.³ For these trapped lithium ions to participate in the battery reaction, they must diffuse through other unfavorable diffusion pathways that require higher activation barriers (> 1 eV).

27-29

Important practical issue with nano-sized LiFePO₄ that needs to be urgently addressed, nevertheless, is the low electrode tap density, which results in a significant reduction in the volumetric energy density. It is simply because the interactions between nanoparticles make it difficult for them to be packed densely. This issue is more serious for LiFePO₄, the crystal density of which is only 3.6 g/cm³, which is substantially lower than those of commercial electrodes, such as LiCoO₂ (5.1 g/cm³) and LiMn₂O₄ (4.2 g/cm³).^{30,31} Using nano-LiFePO₄, in this regard, can hardly satisfy the requirements for batteries with high volumetric energy density. In this regards, it is increasingly important to develop a micro-LiFePO₄ electrode material that is

capable of delivering satisfactory performance with reasonably high gravimetric/volumetric energy density. However, previous studies on large-size LiFePO_4 particles have shown that the material delivers undesirably low specific capacity or power capabilities.^{3,32,33}

The minimization of defects in micro- LiFePO_4 can contribute to enhancing the transport properties because it reduces the possibility of blocking lithium diffusion tunnels. Since the blocking effect becomes more serious in larger particles, as noted, the control of anti-site defects becomes more critical in developing larger LiFePO_4 particles having fast transport properties. Previous approaches to reducing defects in crystals have mainly used high temperatures, with post heat treatment to recombine defects.¹⁸ Here, we report a novel way to reduce anti-site (Li-Fe) defects in LiFePO_4 electrochemically at room temperature. In this approach, we intentionally introduced a vacancy in the lithium channel by partial charging, and carried out a deep discharge below the conventional voltage cut-off. As a result, we observed significant Fe_{Li} -defect annihilation, resulting in defect-less LiFePO_4 from a structural analysis. Furthermore, the electrochemical performance could be enhanced markedly in the 'healed' sample. Density functional theory calculations suggest that Fe_{Li} -defect migration and annihilation could be facilitated by the introduction of vacancies near defects and the injection of excess electrons during over-discharge, which lowers the migration barrier for Fe defects.

2.2 Experimental

Hydrothermal synthesis of LiFePO_4 : LiFePO_4 with a high concentration of defects was synthesized by a hydrothermal method. LiOH (Sigma Aldrich, 99.9%), $\text{FeSO}_4 \cdot 7\text{H}_2\text{O}$ (Sigma Aldrich, 99.8%), and H_3PO_4 (Sigma Aldrich, 85 wt% in water base) were used as precursors at a molar ratio of 3:1:1 in deionized water. The mixture was heated to 180°C in an autoclave and maintained for 2 h in an air atmosphere. The synthesized powder was filtered and then moved to a drying oven at 120°C for 24 h to remove water.

Solid-state synthesis of LiFePO_4 : The solid-state synthesis of LiFePO_4 used precursors such as Li_2CO_3 (Sigma Aldrich, 99.9%), $\text{FeC}_2\text{O}_4 \cdot \text{H}_2\text{O}$ (Sigma Aldrich, 99%), NH_3HPO_4 (Aldrich, 98%), and pyromellitic acid hydrate (Fluka, 6 wt%, PA, 99%) as the organic additive. The powders were ball-milled in acetone for 14 h and dried at 70°C . The mixture was first calcined at 500°C in an Ar atmosphere for 10 h. For additional carbon coating, 6 wt% of pyromellitic acid hydrate and 1 wt% of ferrocene (Aldrich, 98%) were mixed with the calcined powder using a ball-mill in acetone for 2 h. The acetone was then evaporated at 70°C in a drying oven. The dried mixture was pelletized under 200 kg cm^{-2} pressure in a disk-shaped mold, and then sintered again at 600°C under Ar for 10 h.

Synthesis of $\text{Li}_{1-x}\text{FePO}_4$: The prepared LiFePO_4 powders and NO_2BF_4 powder were mixed in acetonitrile for 4 h at a molar ratio of 1:0.1 for chemical delithiation. After the drying process, partially de-lithiated powder was heated again to 380°C for 4 h and quenched with liquid N_2 . An electrode was fabricated by mixing the synthesized

powders, pre-mixed with super P (22 wt%) in a ball mill for 24 h, and polyvinylidene fluoride (PVDF, 10 wt%) in N-methyl-2-pyrrolidone (NMP). The mixture was cast on Al foil and dried at 120°C for 2 h. Electrochemical cells were assembled using a CR2016-type coin cell with lithium metal as the counter electrode, a separator (Celgard 2400), and 1 M LiPF₆ in ethyl carbonate/dimethyl carbonate (Panax, EC/DMC, 1:1 v/v) as the electrolyte in an Ar-filled glove box.

First principles calculation method: First principle calculations were performed using the Perdew–Burke–Ernzerhof exchange-correlation parameterization to density functional theory (DFT) with the spin-polarized generalized gradient approximation (GGA).³⁴ A plane-wave basis set and the projector-augmented wave (PAW) method, as implemented in the Vienna *ab initio* simulation package (VASP), were used. Hubbard parameters (GGA+U) were added to correct the incomplete cancellation of the self-interaction of GGA.^{35,36} A U value of 4.3 eV (the on-site Coulomb term) and a J value of 1.0 eV (the exchange term) were used for the Fe atoms.³⁷ To study the defect configuration in Li_xFePO₄ ($x = 1/16$), we considered all possible orderings within the $1 \times 2 \times 2$ supercell of LiFePO₄ (112 atoms) generated with the CASM program, which contains defects of one Li in the M2 site, one Fe in the M1 site, and one vacancy in the M1 site.³⁸ All plausible configurations of Li-Fe cation site-exchange and a Li-vacancy within the 16-formula unit were considered. Activation energies for the ionic diffusion were calculated using the nudged-elastic-band (NEB) method.³⁹ Appropriate replicate systems were used as starting points for

the NEB method, with linear interpolation between the initial and final states of the diffusion pathways.

Characterization: High-resolution powder diffraction patterns were recorded using synchrotron X-ray radiation (the 8C2-HRPD beam-line at the Pohang Accelerator Laboratory, Korea). The incident X-rays were collimated using a mirror and monochromatized to a wavelength of $\sim 1.5495 \text{ \AA}$ using a Si (111) mono-chromator. The diffraction data were collected in the 10 to 130° range with a step size of 0.01° . Rietveld refinement of the HRPD results was conducted using the “Fullprof” program.⁴⁰ The size and morphology of the powders were observed using field emission scanning electron microscopy (FE-SEM, Philips, XL 30 FEG).

2.3 Results and Discussion

In perfect olivine LiFePO_4 , all Li and Fe ions occupy M1 and M2 octahedral sites, respectively. However, Li/Fe cation site exchange may lead to Li ions in M2 sites and Fe ions in M1 sites.^{20,41} This type of cation disorder can be an edge-shared Li/Fe defect or a corner-shared Li/Fe defect, as shown in Figure 2-1.^{17,41} Calculation of the defect formation energies indicates that both defects are comparable in energy, but the edge-shared Li/Fe defect (~ 390 meV) is slightly more probable than the corner-shared one (~ 490 meV), consistent with previous observations.¹⁷ It has also been noted that the defect formation energy tends to decrease as the $\text{Fe}_{\text{Li}} - \text{Li}_{\text{Fe}}$ distance decreases among the types of anti-site. This indicates that an effectively attractive interaction does exist between Fe_{Li} and Li_{Fe} defects (see the formation energies for various defect types in Figure 2-1). Generally, it is known that these types of Li/Fe site exchange do not recombine during charging/discharging process or at room temperature due to the relatively high activation energy for recombination.⁴¹

The types of stable anti-site configurations differ with the introduction of a lithium vacancy, *i.e.*, $\text{Li}_{1-x}\text{FePO}_4$. DFT calculations on various anti-site configurations showed that the corner-shared Li/Fe defect becomes more probable in Li-deficient olivine, even though both corner-shared (Figure 2-2a) and edge-shared (Figure 2-2b) Li/Fe defects are comparably stable. However, it has been noted that all the stable anti-site configurations contain the vacancy as the first nearest neighbor to the Fe defect at the M1 octahedral site along the *b*-direction. It is believed that the relatively high valent Fe^{3+} exhibits stronger electrostatic repulsion, and thus

prefers a vacancy to Li^+ as its neighbor. As a consequence of the reduction in the electrostatic repulsion, the defect formation energy becomes lower in $\text{Li}_{1-x}\text{FePO}_4$ (~100 to 200 meV) than in LiFePO_4 (~400 to 500 meV; Figure 2-2). Furthermore, defect formation is energetically more stable than the defect-free $\text{Li}_{15/16}\text{FePO}_4$ phase (dotted line in Figure 2-2). This suggests that a meta-stable $\text{Li}_{15/16}\text{FePO}_4$ phase, if any, is likely to contain appreciable amounts of Li/Fe site exchange, although the most stable state is the two-phase coexistence of LiFePO_4 and FePO_4 .

Close examination of the stable anti-site configurations revealed that the major defect type (corner-shared defect, Figure 2-1a) has a plausible re-ordering route. In the possible route, shown in Figure 2-3, Li migrates to the vacant M1 site (inset 1, 2), then Fe moves sequentially to the M2 site (inset 3, 4), annihilating the defect. To assess this possible defect recombination, we calculated the activation energy following the hypothetical migration path using NEB calculations. Figure 2-3 illustrates the energy profile along the recombination path. The recombination involved a relatively high activation energy of ~1.4 eV. When the lithium ion diffuses from M2 to the vacant M1 site, the system becomes destabilized gradually by ~1 eV (inset 2 of Figure 2-3) and iron migration carries an additional ~400 meV barrier (inset 3 of Figure 2-3). The high activation barrier of ~1.4 eV is attributable to the strong electrostatic repulsion among cations during the migration, and implies that the recombination of the defect in such conditions is unlikely to occur at room temperature.^{28,29} However, we found that a slight reduction of the system can significantly lower the activation barrier. When we intentionally injected excess

electrons into the system, Fe^{3+} in the M2 site becomes reduced locally to Fe^{2+} , leading to a decrease in the activation barrier of iron migration from ~ 1.4 eV to ~ 0.8 eV. Considering that the activation barriers in many operable electrodes at room temperature range within several hundreds meV,^{12,28,41} this indicates that recombination of the defect at room temperature is quite plausible in this case. While the injection of excess charge into the system is purely artificial in the calculations, we suggest that it can occur in the dynamic circumstances of charging or discharging of the electrode in electrochemical systems. A local charge imbalance due to the differing mobilities of the cation (Li ion) and electron during discharge can also induce such a situation. However, the second major defect type, the edge-shared defect (Figure 2-2b), does not have an apparent re-ordering route, indicating that an edge-shared defect would not recombine and would remain, even with this healing process, which we will discuss further below.

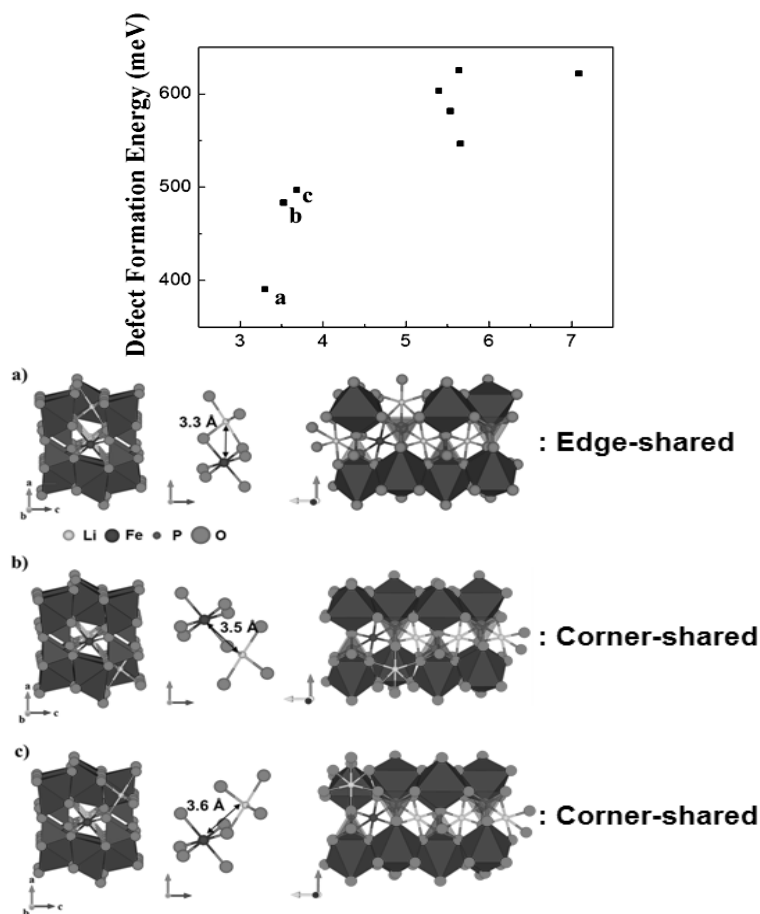


Figure 2-1. Calculated formation energy of anti-site defect in LiFePO_4 and its configuration corresponding to the distance between Li^+ on Fe^{2+} site and Fe^{2+} on Li^+ site. Near anti-site defect has lower formation energy. (a) Edge-shared anti-site defect with the lowest formation energy (about 390 meV) (b), (c) Corner-shared anti-site defect with the formation energy of about 490 meV.

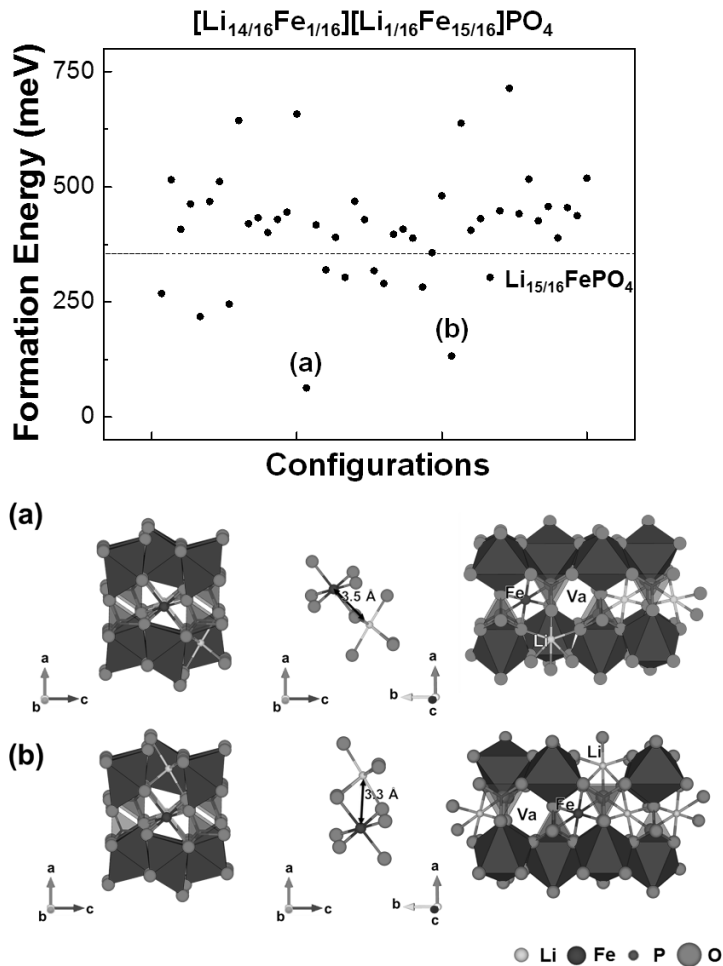


Figure 2-2. Formation energies for 45 different vacancy-Fe defect configurations of the single-phase $\text{Li}_{1-x}\text{FePO}_4$ from first principles calculations. The most stable energy is observed in (a) the corner-shared configuration and the second most stable configurations is shown as (b) the edge-shared configuration.

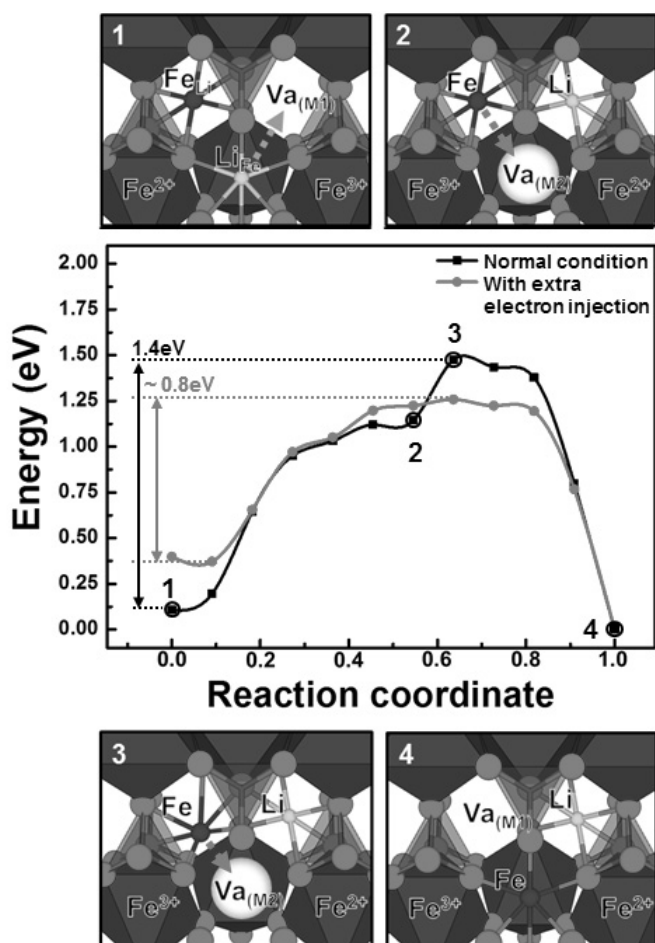


Figure 2-3. Energy curve and schematics of the Fe-Li cation site re-ordering process during discharge. The black line is the Fe/Li recombination route with no charge carrier injection. The red line is the hypothetical Fe/Li recombination route with a charge carrier (electron) injection. Schematics 1 – 4 schematics are Fe-Li cation site re-ordering processes at each point.

Inspired by these theoretical results, we prepared a vacancy-introduced LiFePO_4 , *i.e.*, $\text{Li}_{0.9}\text{FePO}_4$, in the form of solid solution from a defective LiFePO_4 . First, the LiFePO_4 was synthesized hydrothermally and delithiated chemically to obtain a mixture of LiFePO_4 and FePO_4 with a molar ratio of 9:1 (high-resolution powder X-ray diffraction (HRPD) patterns are provided in Figure 2-4). The two-phase mixture was heated and quenched to retain a $\text{Li}_{0.9}\text{FePO}_4$ solid-solution phase. Figure 2-5 shows that the (200) peak of FePO_4 can be detected at $\sim 18^\circ$ in the mixture, which disappears after heating and quenching. The shift of the (200) peak confirms the formation of solid-solution $\text{Li}_{0.9}\text{FePO}_4$. Rietveld refinements of the $\text{Li}_{0.9}\text{FePO}_4$ in Figure 2-5b show that the solid-solution phase was obtained successfully with $a = 10.328 \text{ \AA}$, $b = 6.007 \text{ \AA}$, and $c = 4.706 \text{ \AA}$. Comparison with pristine LiFePO_4 indicated that the lattice parameters decreased after the delithiation, in good agreement with previous reports.⁴² The LiFePO_4 and $\text{Li}_{0.9}\text{FePO}_4$ contain $\sim 4.2\%$ and $\sim 4.0\%$ Li-Fe site exchange, respectively (detailed refinement results are provided in Figure 2-6, Table 2-1, and Table 2-2). Those values match well with previous reports that hydrothermally prepared LiFePO_4 generally contains approximately ~ 3 to 4% defects, which are maintained even at the low post-heat-treatment temperature.^{42,43} The particle size of the sample was $\sim 2 \text{ \mu m}$, as shown in the inset of Figure 2-5b.

By constructing an electrochemical cell using the defective $\text{Li}_{0.9}\text{FePO}_4$, we then attempted to mimic the theoretical results of Li/Fe anti-site recombination. Figure 2-8a shows the galvanostatic intermittent titrations (GITT) discharge profile of $\text{Li}_{0.9}\text{FePO}_4$. While the $\text{Li}_{0.9}\text{FePO}_4$ was capable of lithiating 0.1 Li up to $\sim 1.6 \text{ V}$

discharge, notably high polarization was observed in the profile. However, the open-circuit voltage (OCV) after the relaxation matched that of conventional $\text{Li}_{0.9}\text{FePO}_4$, indicating that the lithium insertion into $\text{Li}_{0.9}\text{FePO}_4$ solid solution occurred with a large kinetic barrier. The high polarization of $\text{Li}_{0.9}\text{FePO}_4$ at this stage will be discussed later.

After imposing the dynamic situation where lithium ions and electrons were injected into the defective $\text{Li}_{0.9}\text{FePO}_4$, we detected an unusual change in structural parameters. Figure 2-8b and Figure 2-9 compare the structural parameters obtained from the careful refinements of HRPDs for pristine LiFePO_4 and $\text{Li}_{0.9}\text{FePO}_4$ before and after electrochemical treatment. The first remarkable observation is that the lithiation of the defective $\text{Li}_{0.9}\text{FePO}_4$, following the protocol above (recombined LiFePO_4 in the Table) resulted in a significant *reduction* in the c lattice, along with the a lattice and the volume. This is in contrast to the general trend with lithiation into olivine where the a and b lattice parameters and volumes *increase*, and the c lattice parameter decreases.⁴² Also, the concentration of anti-site defects decreased from 4.0% to 1.86%. This unusual behavior indicated that not only the lithium content but also other structural rearrangement(s) affected the lattice parameters in the new LiFePO_4 .⁴⁴ At this point, it should be mentioned that the complete annihilation of the defects was not possible even after multiple electrochemical annealing, which we believe is due to the presence of edge-shared Li/Fe defect. As noted above, the edge-shared defect is also comparably probable with the corner-

shared defect in the sample, but cannot be recombined due to the absence of the reordering routes.

From comparisons with previous reports on lattice parameters, we found that lattice parameters of olivines are sensitive to the concentration of defects and that the observed change was likely due to a decrease in Fe_{Li} defects, consistent with our theoretical predictions. In Figure 2-8c, we plot the previously reported lattice parameters of LiFePO_4 as a function of the refined value of Li/Fe site exchange.^{20,32,42,44} This revealed that as the Fe_{Li} defect concentration increased, the a lattice and volume of the olivine increased, following an almost linear relationship. To our surprise, the refined lattice parameters before and after the electrochemical healing of our defective LiFePO_4 (denoted with stars) also showed a similar trend, suggesting that the Li/Fe site exchange had decreased after the healing. Figure 2-9 shows that the b and c lattice parameters followed the same trend, further confirming the decrease in anti-site defects.

Fourier transform infrared spectroscopy (FT-IR) spectra analyses also supported the decrease in the Fe_{Li} defect concentration in the new LiFePO_4 . Previous theoretical and experimental works have indicated that the IR absorption of PO_4^{3-} is sensitive to the presence of defects in the olivine crystal.^{32,45} Defect-free LiFePO_4 shows the PO_4^{3-} absorption typically at ~ 956 to 963 cm^{-1} , whereas LiFePO_4 with a high defect concentration has a PO_4^{3-} signal at ~ 983 to 1003 cm^{-1} .^{32,45,46} In our FT-IR measurements, we found that the PO_4^{3-} absorption varied considerably, depending on the sample. Figure 2-8d shows that the absorption bands of the P-O symmetric

stretching vibration of the LiFePO_4 (anti-sites $\sim 4.2\%$) and $\text{Li}_{0.9}\text{FePO}_4$ (anti-sites $\sim 4.0\%$) were observed at $\sim 985\text{ cm}^{-1}$. In contrast, electrochemically treated LiFePO_4 (anti-sites $\sim 1.8\%$) and the reference LiFePO_4 (anti-sites $\sim 1.0\%$) showed absorption at $\sim 960\text{ cm}^{-1}$, suggesting that the new LiFePO_4 contained fewer Fe-Li cation site exchanges after our experiment, mimicking the charge carrier injection process. Our result is in contrast to previous reports that the recombination of Fe_{Li} defects in LiFePO_4 is only possible above $\sim 500^\circ\text{C}$ with heat treatment⁴⁰ and not during a charging/discharging process.⁴⁷

An unusually high polarization was observed during the initial lithiation of the defective $\text{Li}_{0.9}\text{FePO}_4$ during the electrochemical treatment. Nevertheless, the OCV after relaxation, which was close to $\sim 3.42\text{ V}$, agreed well with the average redox potential of $\text{Fe}^{2+}/\text{Fe}^{3+}$. This indicates that the lithiation process of the defective $\text{Li}_{0.9}\text{FePO}_4$ was a significantly sluggish process that required a high over-potential. We believe that this kinetic barrier was related to the recombination process of the Li/Fe site exchange. As shown before, the recombination required an activation barrier of $\sim 0.8\text{ eV}$, which is higher than that of typical lithium diffusion in conventional LiFePO_4 ($\sim 0.3\text{ eV}$).⁴⁸ Thus, it would require a high over-potential once it occurs at room temperature in an electrochemical cell. The large polarization was only observed during the initial discharge process, and disappeared subsequently in this region (Figure 2-10). This supports the idea that the polarization stems from a structural rearrangement involving the defect recombination.

Using this electrochemical recombination process, we prepared two kinds of defect-less LiFePO₄: one starting from hydrothermally synthesized micro-LiFePO₄, and the other from nano-LiFePO₄ obtained with a conventional solid-state synthesis. The synthesis and characterization of samples are illustrated in the Figure 2-11 and Figure 2-12. Although highly defective LiFePO₄ with micron-size particles usually shows very small capacity at room temperature, the reduction in Li/Fe site exchange could enhance electrochemical performance markedly. Figure 2-13a shows that the reversible capacity of micro-LiFePO₄ could be increased considerably after the recombination process. About ~0.2 Li ion capacity could be additionally achievable even with micron-sized LiFePO₄. It is believed that the reduction of anti-site defect from 4.0% to 1.86% could liberate those amounts of trapped lithium ions. The full utilization of Li in micro-LiFePO₄ was not possible due to the presence of edge-shared Li/Fe defects. The effect of defect reduction was also observable in the nano-LiFePO₄ electrodes. Figure 2-13b shows that the electrochemical recombination could enhance the power capability of the conventional nano-LiFePO₄ synthesized from a solid-solution reaction (~100 to 200 nm; SEM images in Figure 2-12c and d). The electrochemically treated nano-LiFePO₄ delivered ~9.3 to 12.3% higher capacity at higher current rates than its counterpart. At a 30-C rate, the electrochemically annealed sample could achieve ~115 mAh/g, ~20 mAh/g higher than that of conventional nano-LiFePO₄. This confirms that the simple electrochemical treatment described can result in the enhancement of the power capability of defective crystalline electrode materials regardless of the particle sizes.

We believe that the suggested defect recombination mechanism may be broadly applicable to electrode materials that typically suffer from restrained diffusion paths in crystals due to the presence of defects.^{3,42}

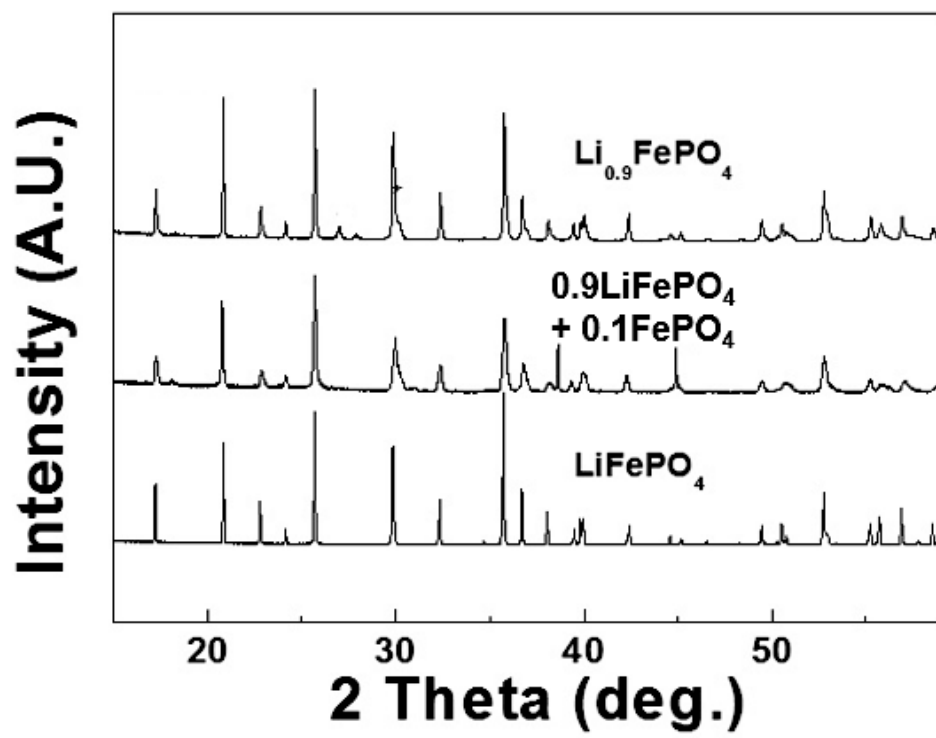


Figure 2-4. The 15 ~ 55° high resolution powder diffraction patterns of prepared by hydrothermal synthesis

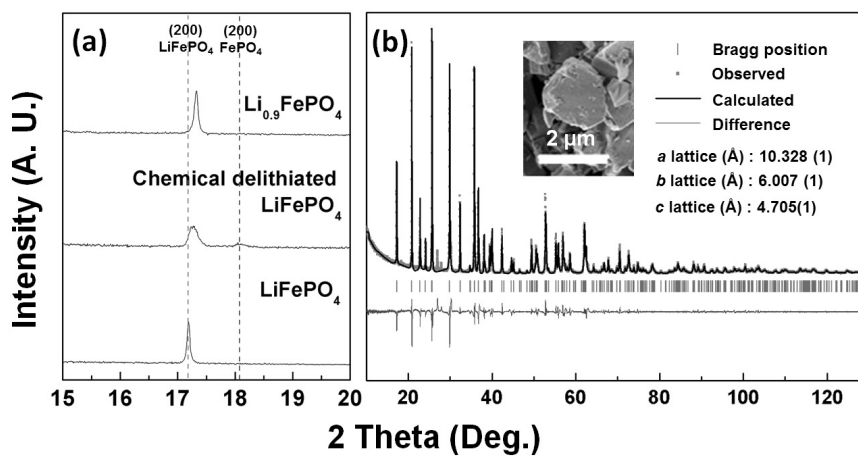


Figure 2-5. (a) Magnified (200) peak of high resolution powder diffraction patterns of the prepared samples. (b) Rietveld refinement results of solid-solution $\text{Li}_{0.9}\text{FePO}_4$. The inset figure is an SEM image of micro-size $\text{Li}_{0.9}\text{FePO}_4$.

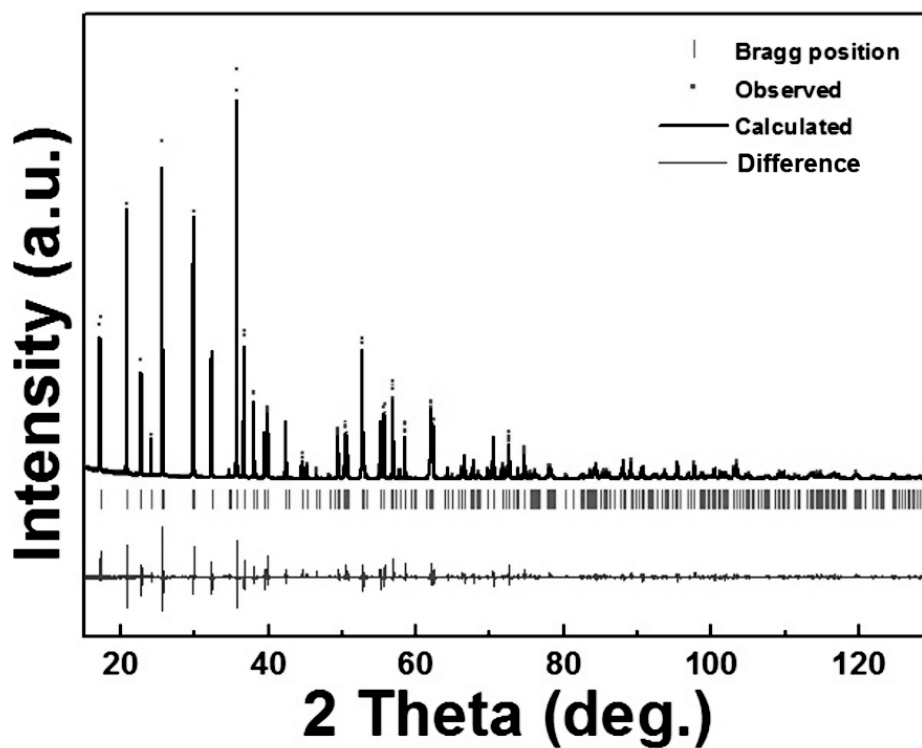


Figure 2-6. Rietveld refinement of hydrothermally prepared LiFePO_4 .

Table 2-1. Detailed structural information of hydrothermally prepared LiFePO₄ analyzed by Rietveld refinement.

Atom	X	Y	Z	Biso	Mult.	Occ.		
Li	0.00000(0)	0.00000(0)	0.00000(0)	1.49	4	0.479	Chi ²	5.49
Fe	0.28189(7)	0.25000(0)	0.97522(17)	0.395	4	0.479	R _p	11
Li _{Fe}	0.28189(7)	0.25000(0)	0.97522(17)	1.49	4	0.021	R _I	5.02
Fe _{Li}	0.00000(0)	0.00000(0)	0.00000(0)	0.395	4	0.021	R _f	3.44
P	0.09524(13)	0.25000(0)	0.41750(26)	0.282	4	0.500	Unit cell V.	292.640(1)
O1	0.09721(34)	0.25000(0)	0.74437(64)	0.495	4	0.500	Lattice a(Å)	10.35027(3)
O2	0.45596(36)	0.25000(0)	0.20695(65)	0.482	4	0.500	Lattice b(Å)	6.01304(2)
O3	0.16747(28)	0.04299(38)	0.28245(42)	0.518	8	1.000	Lattice b(Å)	4.70205(1)

Table 2-2. Detailed structural information of solid-solution Li_{0.9}FePO₄ analyzed by Rietveld refinement.

Atom	X	Y	Z	Biso	Mult.	Occ.		
Li	0.00000(0)	0.00000(0)	0.00000(0)	1.49	4	0.430	Chi ²	9.65
Fe	0.28139(13)	0.25000(0)	0.97462(35)	0.395	4	0.480	R _p	14.2
Li _{Fe}	0.28139(13)	0.25000(0)	0.97462(35)	1.49	4	0.020	R _I	7.71
Fe _{Li}	0.00000(0)	0.00000(0)	0.00000(0)	0.395	4	0.020	R _f	4.71
P	0.09592(23)	0.25000(0)	0.41781(48)	0.282	4	0.500	Unit cell V.	291.998(5)
O1	0.10082(60)	0.25000(0)	0.74909(113)	0.495	4	0.500	Lattice a(Å)	10.32877(8)
O2	0.45482(66)	0.25000(0)	0.20070(109)	0.482	4	0.500	Lattice b(Å)	6.00752(6)
O3	0.16566(49)	0.03936(72)	0.27621(71)	0.518	8	1.000	Lattice b(Å)	4.70582(4)

Table 2-3. Detailed structural information of electrochemically treated LiFePO₄ analyzed by Rietveld refinement.

Atom	X	Y	Z	Biso	Mult.	Occ.		
Li	0.00000(0)	0.00000(0)	0.00000(0)	1.375(90)	4	0.4907(8)	Chi ²	1.50
Fe	0.28166(15)	0.25000(0)	0.97498(43)	0.369(20)	4	0.4907(8)	R _p	6.67
Li _{Fe}	0.28166(15)	0.25000(0)	0.97498(43)	0.280(90)	4	0.0093(8)	R _I	3.94
Fe _{Li}	0.00000(0)	0.00000(0)	0.00000(0)	1.464(20)	4	0.0093(8)	R _f	2.74
P	0.09816(29)	0.25000(0)	0.41935(49)	0.356(41)	4	0.500	Unit cell V.	290.637(4)
O1	0.09531(71)	0.25000(0)	0.74595(118)	0.590(142)	4	0.500	Lattice a(Å)	10.32416(8)
O2	0.44798(82)	0.25000(0)	0.21221(109)	0.192(126)	4	0.500	Lattice b(Å)	5.99040(6)
O3	0.16480(53)	0.04815(79)	0.28282(81)	0.676(90)	8	1.000	Lattice b(Å)	4.66938(4)

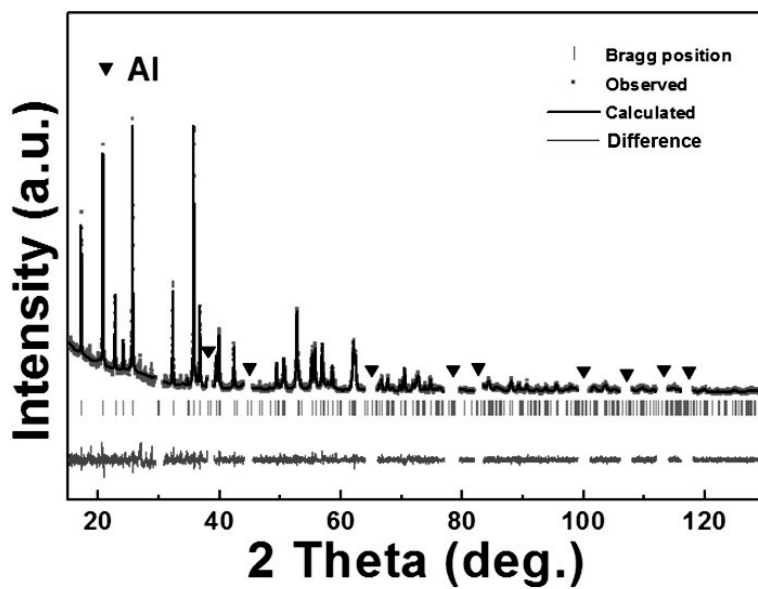


Figure 2-7. Rietveld refinement result of electrochemically treated LiFePO_4 .

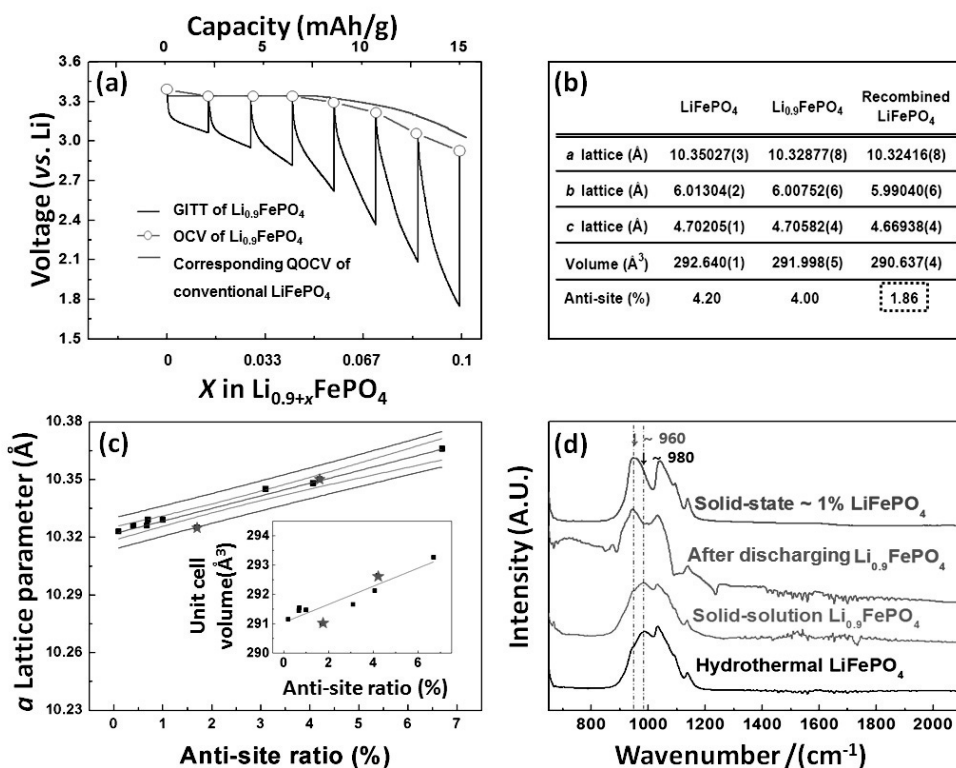


Figure 2-8. Defect characterization (a) Black: GITT result of $\text{Li}_{0.9}\text{FePO}_4$, red: quasi-OCV result of $\text{Li}_{0.9}\text{FePO}_4$, blue: quasi-OCV of conventional LiFePO_4 . (b) Lattice parameters, volume and anti-site ratio of prepared samples. The detailed Rietveld refinement results are provided in supporting Figure S3 – S5. (c) α -lattice parameter change as a function of anti-site ratio. The inset figure is shown the unit cell volume change as a function of anti-site ratio. Red line : trend line, blue line : confidence band, green line : prediction band. The interval coverage probability is set as 95 %. The star points symbolized stand for hydrothermal synthesized LiFePO_4 and electrochemically treated LiFePO_4 . The data are taken from references 20, 30, 40 and 42. (d) FT-IR results of prepared samples PO_4^{3-} spectra.

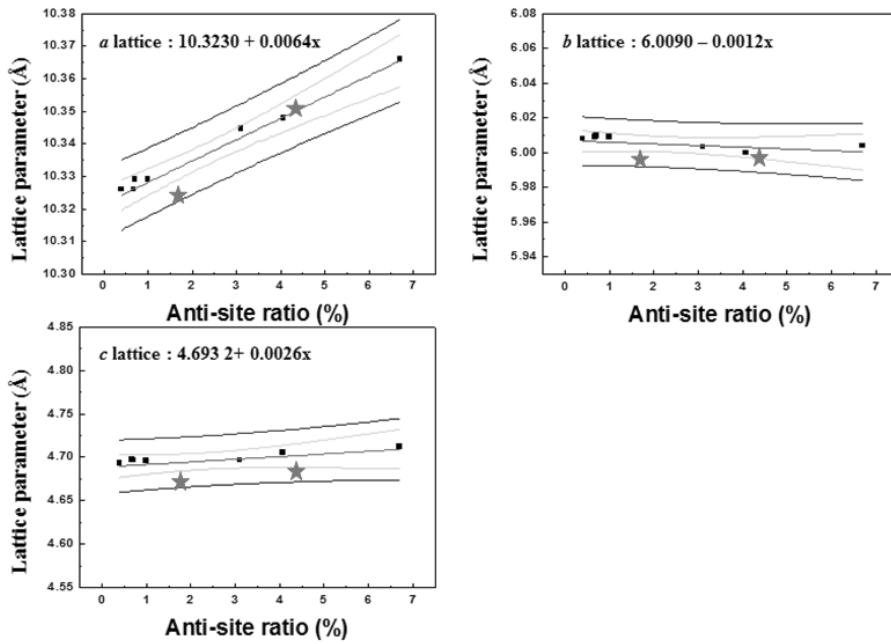


Figure 2-9. Lattice parameter with change modification with anti-site ratio at room temperature. Red line: trend line, blue line: confidence band, green line: prediction band. The interval coverage probability is set as 95 %. This figure used reference number 25, 35, 47 and 49.

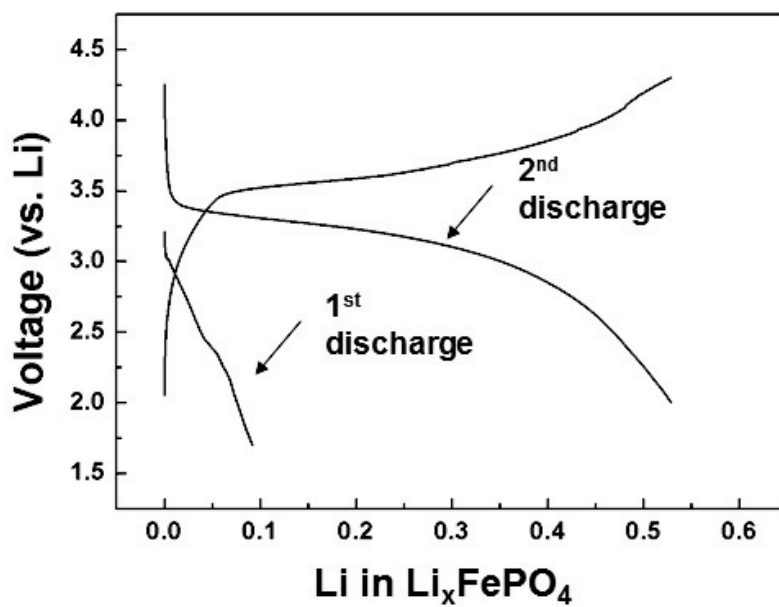


Figure 2-10. The electrochemical profile of solid-solution $\text{Li}_{0.9}\text{FePO}_4$ at C/100. The 1st discharge profile showed unexpected high polarization, however, the 2nd profile did not show overpotential during charging/discharging.

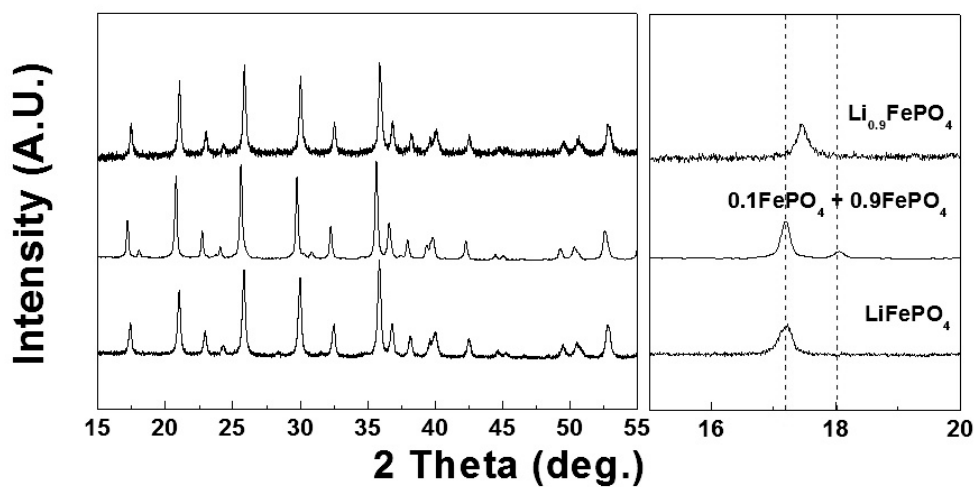


Figure 2-11. 15 ~ 55° XRD patterns of prepared by solid-state method samples (left) and magnified (200) peak of samples (right). red line: (200) peak of LiFePO_4 , blue line: (200) peak of FePO_4 . All samples are well synthesized without remarkable impurities.

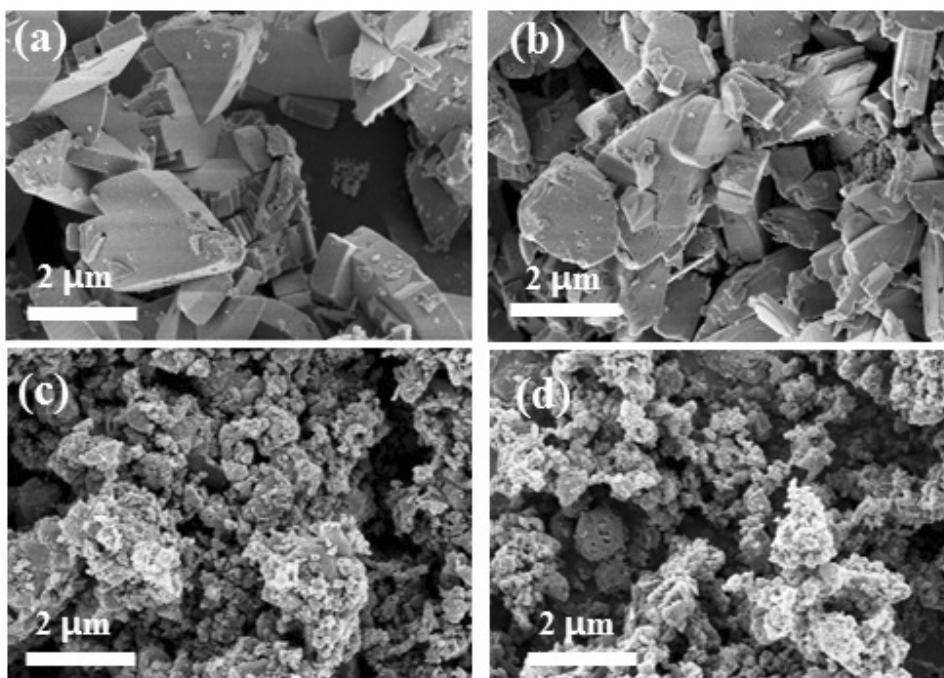


Figure 2-12. SEM image of prepared LiFePO_4 . (a) Hydrothermal synthesis LiFePO_4 (b) $380\text{ }^\circ\text{C}$ heated hydrothermal synthesis $\text{Li}_{0.9}\text{FePO}_4$ (c) $600\text{ }^\circ\text{C}$ solid-state synthesis LiFePO_4 (d) $380\text{ }^\circ\text{C}$ heated solid-state $600\text{ }^\circ\text{C}$ synthesis $\text{Li}_{0.9}\text{FePO}_4$.

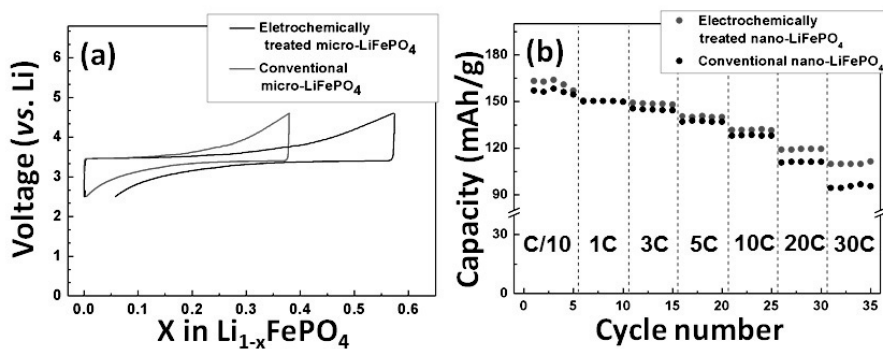


Figure 2-13. (a) First charge/discharge profile at C/200 of electrochemically treated micro-LiFePO₄ and hydrothermally grown micro-LiFePO₄. (b) C-rate capability of electrochemically treated nano-LiFePO₄ (red) and conventional nano-LiFePO₄ (black).

2.4 Conclusion

In this chapter, researcher introduced a new way to reduce defects in crystals with a case study of olivine LiFePO_4 . Fe_{Li} defects in the olivine structure were reduced using a room-temperature electrochemical annealing process. The defect annihilation mechanism was proposed from first principles calculations, which indicated that the introduction of vacancies and excess charge carriers lowered the activation barrier for defect recombination. Using this new method, we demonstrated that defective LiFePO_4 , including both micro- and nano-size particles, can be ‘healed,’ recovering power capabilities. The defect-annihilation mechanism suggested here may be broadly applicable in making defect-less materials, and is expected to help in understanding defect behavior in various materials.

2.5 References

- (1) Sammalkorpi, M.; Krasheninnikov, A.; Kuronen, A.; Nordlund, K.; Kaski, K. *Phys. Rev. B* **2004**, *70*, 245416.
- (2) Kuo, J. H.; Anderson, H. U.; Sparlin, D. M. *J. Solid State Chem.* **1990**, *87*, 55.
- (3) Malik, R.; Burch, D.; Bazant, M.; Ceder, G. *Nano Lett.* **2010**, *10*, 4123.
- (4) Penn, R. L.; Banfield, J. F. *Science* **1998**, *281*, 969.
- (5) Esch, F.; Fabris, S.; Zhou, L.; Montini, T.; Africh, C.; Fornasiero, P.; Comelli, G.; Rosei, R. *Science* **2005**, *309*, 752.
- (6) Wendt, S.; Sprunger, P. T.; Lira, E.; Madsen, G. K. H.; Li, Z.; Hansen, J. Ø.; Matthiesen, J.; Blekinge-Rasmussen, A.; Lægsgaard, E.; Hammer, B.; Besenbacher, F. *Science* **2008**, *320*, 1755.
- (7) Bikondoa, O.; Pang, C. L.; Ithnin, R.; Muryin, C. A.; Onishi, H.; Thornton, G. *Nat. Mater.* **2006**, *5*, 189.
- (8) Vlasov, Y. A.; Bo, X.-Z.; Sturm, J. C.; Norris, D. J. *Nature* **2001**, *414*, 289.
- (9) Philip, J.; Punnoose, A.; Kim, B. I.; Reddy, K. M.; Layne, S.; Holmes, J. O.; Satpati, B.; LeClair, P. R.; Santos, T. S.; Moodera, J. S. *Nat. Mater.* **2006**, *5*, 298.
- (10) Johansson, J.; Karlsson, L. S.; Patrik T. Svensson, C.; Martensson, T.; Wacaser, B. A.; Deppert, K.; Samuelson, L.; Seifert, W. *Nat. Mater.* **2006**, *5*, 574.
- (11) Pertsinidis, A.; Ling, X. S. *Nature* **2001**, *413*, 147.

- (12) Dathar, G. K. P.; Sheppard, D.; Stevenson, K. J.; Henkelman, G. *Chem. Mater.* **2011**, *23*, 4032.
- (13) Fahey, P. M.; Griffin, P. B.; Plummer, J. D. *Rev. Mod. Phys.* **1989**, *61*, 289.
- (14) Chung, S.-Y.; Bloking, J. T.; Chiang, Y.-M. *Nat. Mater.* **2002**, *1*, 123.
- (15) Bracht, H.; Nicols, S. P.; Walukiewicz, W.; Silveira, J. P.; Briones, F.; Haller, E. *E. Nature* **2000**, *408*, 69.
- (16) Allen, J. E.; Hemesath, E. R.; Perea, D. E.; Lensch-Falk, J. L.; Li, Z. Y.; Yin, F.; Gass, M. H.; Wang, P.; Bleloch, A. L.; Palmer, R. E.; Lauhon, L. J. *Nat Nano* **2008**, *3* (3), 168.
- (17) Islam, M. S.; Driscoll, D. J.; Fisher, C. A. J.; Slater, P. R. *Chem. Mater.* **2005**, *17*, 5085.
- (18) Chung, S.-Y.; Choi, S.-Y.; Yamamoto, T.; Ikuhara, Y. *Phys. Rev. Lett.* **2008**, *100*, 125502.
- (19) Kang, K.; Meng, Y. S.; Bréger, J.; Grey, C. P.; Ceder, G. *Science* **2006**, *311*, 977.
- (20) Padhi, A. K.; Nanjundaswamy, K. S.; Goodenough, J. B. *J. Electrochem. Soc.* **1997**, *144*, 1188.
- (21) Padhi, A. K.; Nanjundaswamy, K. S.; Masquelier, C.; Okada, S.; Goodenough, J. B. *J. Electrochem. Soc.* **1997**, *144*, 1609.
- (22) Yamada, A.; Chung, S. C.; Hinokuma, K. *J. Electrochem. Soc.* **2001**, *148*, A224.
- (23) Delacourt, C.; Poizot, P.; Tarascon, J.-M.; Masquelier, C. *Nat. Mater.* **2005**, *4*, 254.

- (24) Chen, G.; Song, X.; Richardson, T. J. *J. Electrochem. Soc.* **2007**, *154*, A627.
- (25) Wang, Y.; He, P.; Zhou, H. *Energy Environ. Sci.* **2011**, *4*, 805.
- (26) Xie, H. M.; Wang, R. S.; Ying, J. R.; Zhang, L. Y.; Jalbout, A. F.; Yu, H. Y.; Yang, G. L.; Pan, X. M.; Su, Z. M. *Adv. Mater.* **2006**, *18*, 2609.
- (27) Morgan, D.; Van der Ven, A.; Ceder, G. *Electrochem. Solid-State Lett.* **2004**, *7*, A30.
- (28) Kang, K.; Morgan, D.; Ceder, G. *Phys. Rev. B* **2009**, *79*, 014305.
- (29) Kang, K.; Ceder, G. *Phys. Rev. B* **2006**, *74*, 094105.
- (30) Yamada, A.; Hosoya, M.; Chung, S.-C.; Kudo, Y.; Hinokuma, K.; Liu, K.-Y.; Nishi, Y. *J. Power Sources* **2003**, *119–121*, 232.
- (31) Yang, M.-R.; Teng, T.-H.; Wu, S.-H. *J. Power Sources* **2006**, *159*, 307.
- (32) Qin, X.; Wang, J.; Xie, J.; Li, F.; Wen, L.; Wang, X. *Phys. Chem. Chem. Phys.* **2012**, *14*, 2669.
- (33) Delmas, C.; Maccario, M.; Croguennec, L.; Le Cras, F.; Weill, F. *Nat. Mater.* **2008**, *7*, 665.
- (34) Perdew, J. P.; Burke, K.; Ernzerhof, M. *Phys. Rev. Lett.* **1996**, *77*, 3865.
- (35) Kresse, G.; Furthmüller, J. *Comp. Mater. Sci.* **1996**, *6*, 15.
- (36) Anisimov, V. I.; Zaanen, J.; Andersen, O. K. *Phys. Rev. B* **1991**, *44*, 943.
- (37) Wang, L.; Maxisch, T.; Ceder, G. *Phys. Rev. B* **2006**, *73*, 195107.

- (38) Van der Ven, A.; Thomas, J. C.; Xu, Q.; Swoboda, B.; Morgan, D. *Phys. Rev. B* **2008**, *78*, 104306.
- (39) Henkelman, G.; Uberuaga, B. P.; Jonsson, H. *J. Chem. Phys.* **2000**, *113*, 9901.
- (40) Carvajal, J. *Abstracts of the Satellite Meeting on Powder Diffraction of the XV Congress of the IUCr* **1990**.
- (41) Tealdi, C.; Spreafico, C.; Mustarelli, P. *J. Mater. Chem.* **2012**, *22*, 24870.
- (42) Chen, J.; Graetz, J. *ACS Appl. Mater.* **2011**, *3*, 1380.
- (43) Yang, S.; Song, Y.; Zavalij, P. Y.; Stanley Whittingham, M. *Electrochem. Commun.* **2002**, *4*, 239.
- (44) Yamada, A.; Koizumi, H.; Nishimura, S.-i.; Sonoyama, N.; Kanno, R.; Yonemura, M.; Nakamura, T.; Kobayashi, Y. *Nat. Mater.* **2006**, *5*, 357.
- (45) Burba, C. M.; Frech, R. *J. Electrochem. Soc.* **2004**, *151*, A1032.
- (46) Cho, M.-Y.; Kim, K.-B.; Lee, J.-W.; Kim, H.; Kim, H.; Kang, K.; Chul Roh, K. *RSC Adv.* **2013**, *3*, 3421.
- (47) Badi, S.-P.; Wagemaker, M.; Ellis, B. L.; Singh, D. P.; Borghols, W. J. H.; Kan, W. H.; Ryan, D. H.; Mulder, F. M.; Nazar, L. F. *J. Mater. Chem.* **2011**, *21*, 10085.
- (48) Ouyang, C.; Shi, S.; Wang, Z.; Huang, X.; Chen, L. *Phys. Rev. B* **2004**, *69*, 104303.

Chapter 3. New iron-Based Mixed-Phosphate Cathodes for Lithium and Sodium Rechargeable Batteries

(The content of this chapter has been published in *Journal of the American Chemical Society*. Reprinted with permission from [H. Kim and I. Park et al., *J. Am. Chem. Soc.* **2012**, *134* (25), 10369-10372.]. Copyright (2012) American Chemical Society.)

3.1 Introduction

An integral part of the new energy economy is to provide cost-effective, sustainable energy storage. Chemical energy storage in the form of batteries, in particular, the most advanced lithium-ion batteries, will contribute strongly to the energy storage picture. However, the cost-effectiveness per energy and the safety hazards regarding lithium-ion batteries have so far prohibited their widespread use in large-scale applications.

In this respect, the search for new polyanion compounds using iron as a redox center is of timely significance. Using naturally abundant iron as a full redox couple, combined with stabilization of the oxygen atoms within the crystal via the strong covalent bonds of the polyanion,¹ may significantly reduce the energy costs and safety concerns. This has led to the use of olivine lithium iron phosphate, LiFePO_4 , as a popular cathode material for lithium-ion batteries.^{2,3} Recent studies on polyanion materials using the $\text{Fe}^{2+}/\text{Fe}^{3+}$ redox couple have identified new compounds, such as

fluorinated iron phosphate ($\text{Li}_2\text{FePO}_4\text{F}$),⁴ iron pyrophosphate ($\text{Li}_2\text{FeP}_2\text{O}_7$),^{1,5} fluorinated iron sulfate (LiFeSO_4F),^{6,7} iron silicate ($\text{Li}_2\text{FeSiO}_4$),⁸ and iron borate (LiFeBO_3),^{9,10} as alternatives. However, the synthesis of fluorinated compounds requires complex and costly procedures, and their theoretical capacities are hardly obtainable. Moreover, some of the fluorinated compounds such as $\text{Li}_2\text{FePO}_4\text{F}$ are moisture sensitive, while the most moisture stable phase is LiFePO_4F .^{11,12} Lithium iron silicates and iron borates are unable to provide sufficient voltage, and the specific capacity of $\text{Li}_2\text{FeP}_2\text{O}_7$ is less than 110 mAh g^{-1} .

In the search for new iron-based lithium-containing cathode materials, our prime interest is in mixed-polyanion systems, which were examined by pioneering work of Goodenough et al.^{13,14} Recently, mixed-polyanion compounds are refocused, and theoretical work predicted that the combination of $\text{YO}_3^{2 \text{ or } 3-}$ and $\text{XO}_4^{3 \text{ or } 4-}$ ($\text{Y} = \text{C}, \text{B}; \text{X} = \text{Si}, \text{As}, \text{P}$) could give a series of new $\text{A}_x\text{M}(\text{YO}_3)(\text{XO}_4)$ compounds ($\text{A} = \text{Li}, \text{Na}; \text{M} = \text{a redox transition metal}; \text{and } x = 0-3$) suitable for cathode materials.^{15,16} The experimental synthesis of the mixedphosphate, $\text{Li}_9\text{V}_3(\text{P}_2\text{O}_7)_3(\text{PO}_4)_2$, with the vanadium $\text{V}^{3+}/\text{V}^{5+}$ redox couple, showed promising electrochemical properties.^{17,18} We believe that the variety of combinations among different polyanion groups may lead to the discovery of a new open crystal framework containing both lithium and iron.

One of our main objectives of this study was to synthesize materials based on the mixed polyanion groups of $(\text{PO}_4)^{3-}$ and $(\text{P}_2\text{O}_7)^{4-}$ with the $\text{Fe}^{2+}/\text{Fe}^{3+}$ redox couple. Currently, the known mixed phosphate that is closest to our aim is

$\text{Na}_4\text{Me}_3(\text{PO}_4)_2(\text{P}_2\text{O}_7)$ (Me = Mn, Co, Ni, Mg).^{19,20} However, to the best of our knowledge, an iron analogue with this composition has been neither synthesized nor documented in the materials database. It was expected that such an unreported compound would not be stable under conventional synthesis conditions, and may, therefore, require a special synthesis route. However, contrary to expectations, $\text{Na}_4\text{Fe}_3(\text{PO}_4)_2(\text{P}_2\text{O}_7)$ was easily obtained using a simple solid-state method. Furthermore, from the first principles calculations, we found $\text{Na}_4\text{Fe}_3(\text{PO}_4)_2(\text{P}_2\text{O}_7)$ to be a promising candidate for cathode materials in terms of its voltage and the mobility of alkali cations for Na-ion batteries. Finally, we showed that sodium could be topotactically ion-exchanged with lithium to produce a new lithium compound that inherited the good electrochemical properties of the parent sodium phase for lithium-ion batteries.

3.2 Experimental

Synthesis of $\text{Na}_4\text{Fe}_3(\text{PO}_4)_2(\text{P}_2\text{O}_7)$: $\text{Na}_4\text{Fe}_3(\text{PO}_4)_2(\text{P}_2\text{O}_7)$ was synthesized using a simple solid-state method. Stoichiometric amounts of $\text{Na}_4\text{P}_2\text{O}_7$ (95%, Aldrich), $\text{Fe}_2\text{C}_2\text{O}_4 \cdot 2\text{H}_2\text{O}$ (99%, Aldrich), and $\text{NH}_4\text{H}_2\text{PO}_4$ (98% ACS reagent, Aldrich) were used as the starting materials. These precursors were mixed by ball-milling with acetone for 24 h and then evaporating the acetone at 70°C for 12 h. The homogeneous mixed powder was fired at 300°C under flowing Ar for 6 h. The calcined powder was pelletized manually under 200 kg cm⁻² pressure using a disk-shaped mold. This sample was then heated again at 500°C for 12 h. For the electrode composite, pyromellitic acid (PA) ($\text{C}_{10}\text{H}_6\text{O}_2$, 96%, Alfa Aesar) was added during the ball-milling step to enhance the electrochemical properties (weight ratio of the active material: PA = 95:5).

Synthesis of $\text{NaFe}_3(\text{PO}_4)_2(\text{P}_2\text{O}_7)$: An oxidized sample of $\text{NaFe}_3(\text{PO}_4)_2(\text{P}_2\text{O}_7)$ was prepared by stoichiometric amounts of NO_2BF_4 (95%, Aldrich) in an acetonitrile solvent (anhydrous, 99.8%, Aldrich) according to the following reaction:



NO_2BF_4 was used as the oxidizing agent with a 5.1 V redox potential versus Li^+/Li .²¹⁻²² The solution was stirred at 60°C for 12 h. $\text{NaFe}_3(\text{PO}_4)_2(\text{P}_2\text{O}_7)$ was obtained by washing several times with acetonitrile.

Synthesis of ion-exchanged $\text{Li}_3\text{NaFe}_3(\text{PO}_4)_2(\text{P}_2\text{O}_7)$: The ion-exchange of $\text{Na}_4\text{Fe}_3(\text{PO}_4)_2(\text{P}_2\text{O}_7)$ occurred in a 1M LiBr and 1-hexanol (anhydrous, 99%, Aldrich)

solution at 100–160°C for 24 h. The obtained $\text{Li}_x\text{Na}_{4-x}\text{Fe}_3(\text{PO}_4)_2(\text{P}_2\text{O}_7)$ was optimized to $\text{Li}_3\text{NaFe}_3(\text{PO}_4)_2(\text{P}_2\text{O}_7)$ (Li/Na ratio of 3:1).

Structural characterization: Powder X-ray diffraction (XRD) data of the synthesized $\text{Na}_x\text{Fe}_3(\text{PO}_4)_2(\text{P}_2\text{O}_7)$ ($x = 4, 1$) were collected using an X-ray diffractometer (Rigaku, D/MAX 2500) equipped with a Cu K α radiation ($\lambda = 1.5406$ Å). The data were recorded over a 2θ range of 5–100° at 4-s steps of 0.02°. The XRD data of $\text{Li}_x\text{NaFe}_3(\text{PO}_4)_2(\text{P}_2\text{O}_7)$ ($x = 3, 0$) were obtained over a 2θ range of 5–80°, with 0.01° steps per 2 s using an X-ray diffractometer an XRD (Bruker, New D8 Advance) at Research Institute of Advanced Materials, Seoul National University. Neutron diffraction (ND) analyses of $\text{Na}_4\text{Fe}_3(\text{PO}_4)_2(\text{P}_2\text{O}_7)$ were performed to determine detailed structural information. ND data were obtained using a high-resolution powder diffractometer (HRPD) at the HANARO facility, Korea Atomic Energy Research Institute. The data were recorded at $\lambda = 1.8348$ Å with a step size of 0.05° over a 2θ range of 0–180°. Rietveld refinement of the XRD and ND patterns was performed using Fullprof software.²³ *In-situ* high-temperature XRD data were collected over a 2θ range of 5–60° with a scan rate of 1° min⁻¹ at each temperature using an X-ray diffractometer (Rigaku, D/MAX 2500).

Mossbauer analysis: The ⁵⁷Fe Mössbauer spectra were recorded using a ⁵⁷Co source (60 mCi) in a Rh matrix with the spectrometer moving at constant acceleration.

Other analyses methods: The atomic ratios of the elements, including Li, Na, Fe, and P, were confirmed by inductively-coupled plasma–atomic emission

spectroscopy (ICP–AES, Thermo Jarrel Ash, Polyscan 60E, USA). The composition ratio of Na:Fe was confirmed to be 4.04:3 for $\text{Na}_4\text{Fe}_3(\text{PO}_4)_2(\text{P}_2\text{O}_7)$ and 1.1:3 for $\text{NaFe}_3(\text{PO}_4)_2(\text{P}_2\text{O}_7)$. Thermal gravimetric analysis (TGA) and differential scanning calorimetry (DSC) were used to investigate the synthesis, temperature, and structural stability of the desodiated phase. Data were recorded at a heating rate of $10^\circ\text{C min}^{-1}$ from room temperature to 650°C under an Ar atmosphere using a Setsys 16/18 thermogravimetric analyzer (SETARAM, France).

First principles calculation method: Density functional theory (DFT) calculations were performed using the Vienna *ab initio* simulation package (VASP) code²⁴ with the spin-polarized generalized gradient approximation (GGA) and the Perdew–Burke–Ernzerhof (PBE) functional²⁵ for the exchange-correlation. A plane-wave basis set and the projector-augmented-wave (PAW) method were used as implemented in the VASP. Because GGA involves incomplete cancellation of the self-interaction, we used GGA+U^{26–27}, which is a well-established approach for transition metal compounds to accurately calculate their structural and electronic properties. We used a U value of 4.3 eV for the Fe ion, which was previously determined from the self-consistent calculation of olivine phosphate. All calculations were performed in supercells ($a \times 2b \times c$) of eight formula units of $\text{Na}_4\text{Fe}_3(\text{PO}_4)_2(\text{P}_2\text{O}_7)$. A plane-wave basis with a kinetic energy cutoff of 500 eV and appropriate k -point meshes were used to ensure that the total energies converged within 5 meV per formula unit. The initial unit cells for the geometry optimizations were taken from our experimental structural data on $\text{Na}_4\text{Fe}_3(\text{PO}_4)_2(\text{P}_2\text{O}_7)$. The

activation barrier for Na diffusion in $\text{Na}_4\text{Fe}_3(\text{PO}_4)_2(\text{P}_2\text{O}_7)$ was calculated with the nudged-elastic-band (NEB) method in supercells ($a \times 2b \times c$).²⁸ For these calculations, a Na ion was allowed to diffuse in the supercells of $\text{Na}_{4-1/8}\text{Fe}_3(\text{PO}_4)_2(\text{P}_2\text{O}_7)$. During the NEB calculation, all of the lattice parameters were fixed; however, all of the internal degrees of freedom were relaxed.

Electrode fabrication: Samples of the electrochemical active materials were mixed with super P and polyvinylidene fluoride (PVDF) at a weight ratio of 70:20:10 in N-methyl-2-pyrrolidone (99.5%, Aldrich) (NMP) solvent. The electrode was assembled by a CR2016-type coin cell using lithium metal (Hohsen Corp, Japan) as an anode for the Li-ion cell and sodium metal (sodium cube 99%, Aldrich) as an anode for the Na-ion cell. Ethylene carbonate/dimethyl carbonate (EC/DMC 1:1 v/v, Technosemichem) with 1M LiPF_6 solution was used as an electrolyte for the Li-ion cell, and propylene carbonate (anhydrous 99.x%, Aldrich) with NaClO_4 (99.x%, Aldrich) was used for the Na-ion cell. A separator (Celgard 2400) was used in both the Na- and Li-ion cells. Galvanostatic charge/discharge tests were carried out at various C-rates (2C, 1C, C/5, C/10, C/20, C/40) for both the Na phase and the Li phase. The cut-off voltage was in the range of 1.7–4.3 V for the Na-ion cell and 2.0–4.6 V for the Li-ion cell. The cyclic voltammogram was obtained at a scan rate of 0.01 mV s^{-1} .

3.3 Results and Discussion

$\text{Na}_4\text{Fe}_3(\text{PO}_4)_2(\text{P}_2\text{O}_7)$ was successfully synthesized via a conventional solid-state reaction at 500 °C (see Figure 3-1). The first calcination was performed at 300°C based on the endothermic peak in the range of 150–300 °C in DSC. The final firing was conducted at 450–500 °C, the flat region in the DSC results. The exothermic peak after 500 °C in the DSC analysis is attributed to the evolution of NaFePO_4 . Figure 3-2a shows a schematic representation of the crystal. The crystal framework is composed of a 3D network of $[\text{Fe}_3\text{P}_2\text{O}_{13}]_\infty$ infinite layers parallel to the b–c plane. The $[\text{Fe}_3\text{P}_2\text{O}_{13}]_\infty$ layer is connected along the a-axis by P_2O_7 groups, and this diphosphate connection produces large tunnels that can provide one of the Na-diffusion channels along the b-axis. The structural characterization based on neutron diffraction (ND) data, shown in Figure 3-2b, confirmed that the $\text{Na}_4\text{Fe}_3(\text{PO}_4)_2(\text{P}_2\text{O}_7)$ is isostructural to $\text{Na}_4\text{Co}_3(\text{PO}_4)_2(\text{P}_2\text{O}_7)$, as reported by Sanz et al.¹⁶ The Rietveld refinement with a space group of $Pn2_1a$ identified that $a = 18.07517$ (7) Å, $b = 6.53238$ (2) Å, $c = 10.64760$ (4) Å, and $V = 1257.204$ (1) Å³. The fitting was satisfactory ($R_p = 1.92$ %, $R_1 = 1.98$ %, $R_F = 1.01$ %). A detailed structural illustration of $\text{Na}_4\text{Fe}_3(\text{PO}_4)_2(\text{P}_2\text{O}_7)$ and a summary of the crystal data can be found in Figure 3-3 and Table 3-1. A trace amount (< 4 %) of the NaFePO_4 impurity was detected in the ND patterns, and the impurity formation gradually increased above 550 °C, as shown by in situ high-temperature X-ray diffraction (XRD) analysis (Figure 3-4), thermal gravimetric analysis (TGA), and differential scanning calorimetry (DSC) results (Figure 3-1).

There are four symmetrically distinguishable Na sites in the crystal, and these are connected to each other throughout the 3D framework. Two Na sites (Na2 and Na3) formed by seven coordinated NaO_7 polyhedra and NaO_6 octahedra are present along the a -axis. Two other Na sites (Na1 and Na4), formed by NaO_6 octahedra, are located on the b - c plane, as shown in Figure 3-2c. All of the probable diffusion pathways among the four Na sites were examined by first principles calculations. Figure 3-2c illustrates the only energetically plausible Na diffusion paths, with activation barriers lower than 800 meV. The color gradient from yellow to green in Figure 3-2c indicates the site energies of Na during the migration along the path, from which we can identify the fast diffusion pathways of Na. While all Na sites are connected with reasonably low activation barriers, the Na diffusion in the large tunnel along the b -axis (Na1–Na1) shows the lowest activation barrier (see Table 3-2 for the activation barriers for each Na diffusion path). The Na moves sinusoidally along the b -axis due to the electrostatic repulsion from the neighboring iron, as shown in Figure 3-5b. It is interesting to note that the sinusoidal motion of Li along the 1D channel was also observed in LiFePO_4 .²⁹ Figure 3-5 shows the detailed diffusion mechanism and the landscape of the activation barrier.

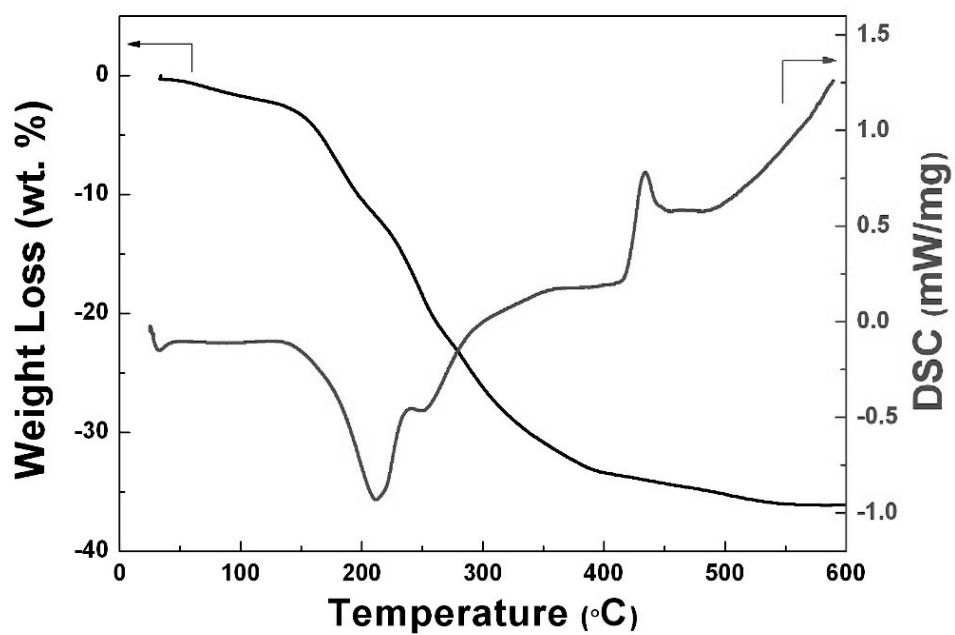


Figure 3-1. Thermogravimetric analysis and differential scanning calorimetry (TGA/DSC) of the precursor used for the solid-state synthesis of $\text{Na}_4\text{Fe}_3(\text{PO}_4)_2(\text{P}_2\text{O}_7)$.

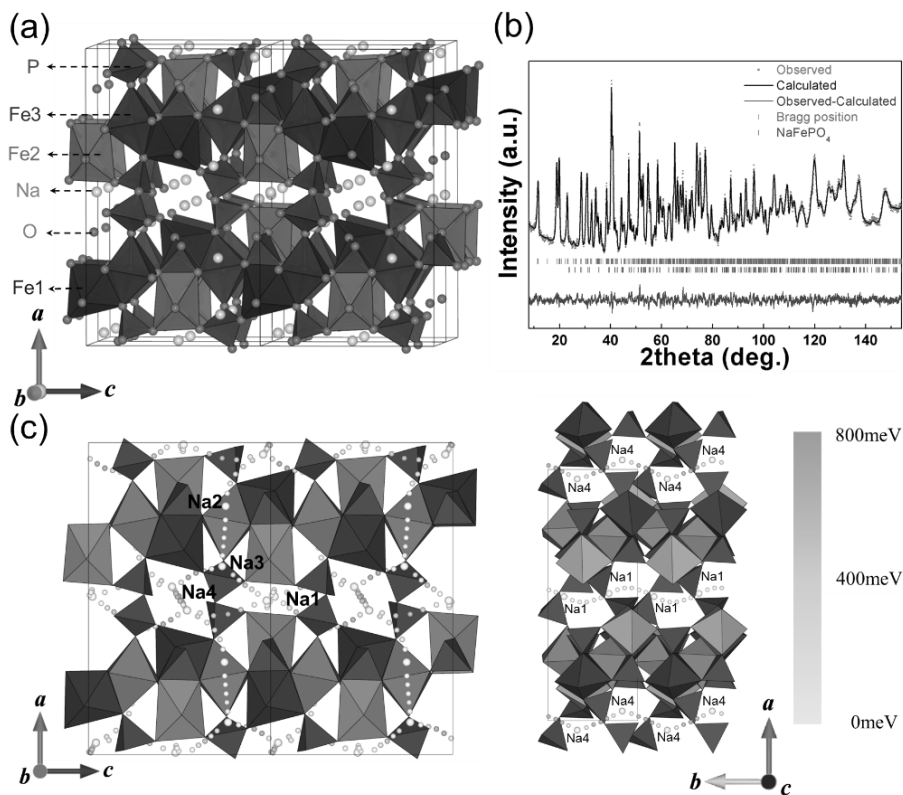


Figure 3-2. (a) Schematic representation of $\text{Na}_4\text{Fe}_3(\text{PO}_4)_2(\text{P}_2\text{O}_7)$. (b) Rietveld refinement of the neutron diffraction patterns of $\text{Na}_4\text{Fe}_3(\text{PO}_4)_2(\text{P}_2\text{O}_7)$. The observed and calculated intensities are represented by the red markers and the black solid line, respectively. The bottom blue line represents the difference between the observed and calculated patterns. Bragg positions for $\text{Na}_4\text{Fe}_3(\text{PO}_4)_2(\text{P}_2\text{O}_7)$ are represented as green markers, and the NaFePO_4 (~4%) impurity is shown as purple markers. (c) The 3D sodium diffusion paths in the $\text{Na}_4\text{Fe}_3(\text{PO}_4)_2(\text{P}_2\text{O}_7)$ structure.

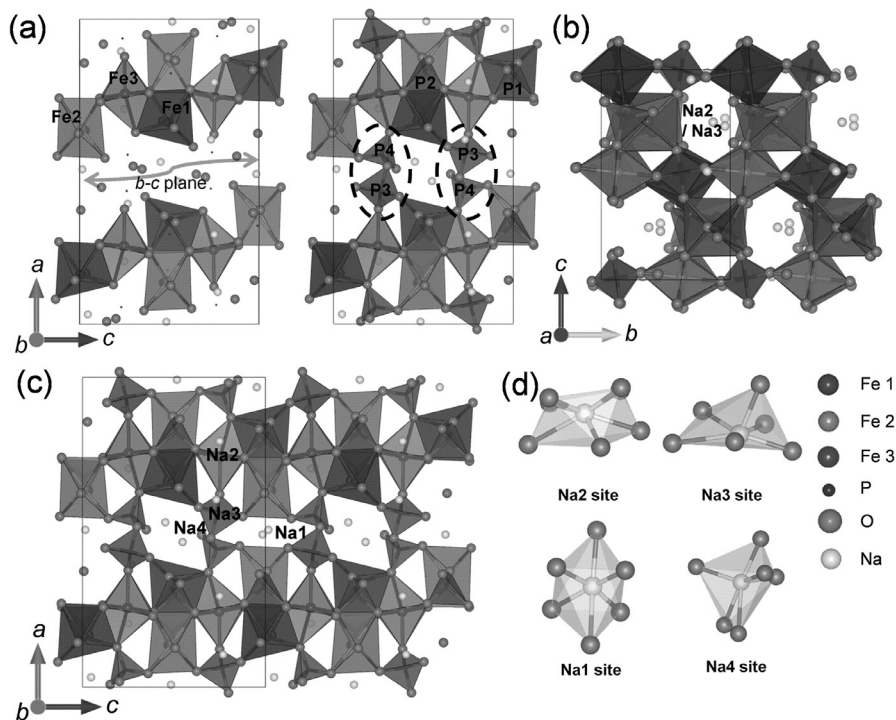


Figure 3-3. Detailed schematics of the Na channel along the b - c plane and the diphasphate connection between the $[\text{Fe}_3\text{P}_2\text{O}_{13}]_\infty$ layers are presented in (a). The sodium sites along the a - and b -axes in the structure of $\text{Na}_4\text{Fe}_3(\text{PO}_4)_2(\text{P}_2\text{O}_7)$ are shown in (b) and (c), respectively. The four different Na sites in the structure of $\text{Na}_4\text{Fe}_3(\text{PO}_4)_2(\text{P}_2\text{O}_7)$ are shown in (d).

Table 3-1. The detailed data for the structural refinement of $\text{Na}_4\text{Fe}_3(\text{PO}_4)_2(\text{P}_2\text{O}_7)$ using ND patterns.

Formula	$\text{Na}_4\text{Fe}_3(\text{PO}_4)_2(\text{P}_2\text{O}_7)$
Crystal system	Orthorhombic
Space group	$\text{Pn}2_1\text{a}$ (No. 33)
Lattice parameters	
a (Å)	18.07517 (7)
b (Å)	6.53238 (2)
c (Å)	10.64760 (4)
Unitcell volume (Å ³)	1257.204 (1)
Formula weight	623.38012
Source	Neutron
Temperature (K)	300K
Wave length (Å)	1.834333
2θ range	0 – 180°
Number of data points	3200
Number of reflections	1092
R_p (%)	1.92
R_I (%)	1.98
R_F (%)	1.01
χ^2	3.55

Atom	x	y	z	Biso
Fe1	0.3377(3)	0.138(3)	0.5042(9)	0.03(7)
Fe2	0.1402(3)	0.624(3)	0.4886(8)	0.03(7)
Fe3	0.2440(5)	0.358(4)	0.7469(11)	0.03(7)
P1	0.2950(6)	0.618(4)	0.502(2)	0.13(10)
P2	0.1772(5)	0.123(5)	0.4918(19)	0.13(10)
P3	0.5630(6)	0.488(4)	0.7382(14)	0.13(10)
P4	0.4446(7)	0.173(4)	0.7323(12)	0.13(10)
Na1	0.4923(13)	0.822(4)	0.984(2)	1.1(2)
Na2	0.2941(9)	0.868(4)	0.750(3)	1.1(2)
Na3	0.3949(11)	0.459(4)	0.2686(20)	1.1(2)
Na4	0.4681(12)	0.695(2)	0.5473(19)	1.1(2)
O1	0.2417(8)	0.590(3)	0.6136(16)	0.29(5)
O2	0.3563(8)	0.439(4)	0.4731(14)	0.29(5)
O3	0.3335(6)	0.814(4)	0.5351(12)	0.29(5)
O4	0.2414(7)	0.649(4)	0.3874(13)	0.29(5)
O5	0.2355(7)	0.138(4)	0.6097(12)	0.29(5)
O6	0.1258(7)	-0.071(4)	0.5074(13)	0.29(5)
O7	0.2299(7)	0.086(4)	0.3848(15)	0.29(5)
O8	0.1352(7)	0.302(4)	0.4674(12)	0.29(5)
O9	0.4819(7)	0.401(4)	0.7019(10)	0.29(5)
O10	0.5510(7)	0.595(4)	0.8760(12)	0.29(5)
O11	0.6225(6)	0.326(3)	0.7502(18)	0.29(5)
O12	0.5816(5)	0.634(4)	0.6339(12)	0.29(5)
O13	0.4558(6)	0.123(4)	0.8585(13)	0.29(5)
O14	0.3709(7)	0.191(4)	0.6882(12)	0.29(5)
O15	0.4915(7)	0.026(3)	0.6515(10)	0.29(5)

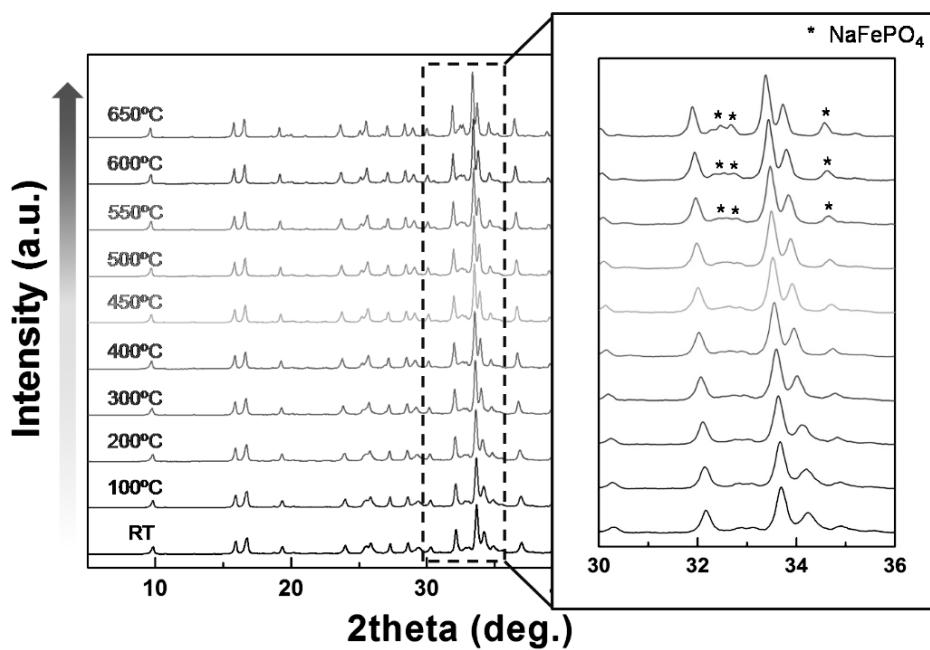


Figure 3-4. *In-situ* high-temperature X-ray diffraction (XRD) patterns of $\text{Na}_4\text{Fe}_3(\text{PO}_4)_2(\text{P}_2\text{O}_7)$ in the temperature range of 25–650°C under an Ar atmosphere. The NaFePO_4 peaks start to significantly evolve above 550°C.

Table 3-2. Sodium vacancy activation barriers in the $\text{Na}_4\text{Fe}_3(\text{PO}_4)_2(\text{P}_2\text{O}_7)$ structure.

From (site)	To (site)	Activation energy (meV)
Na1	Na1	256meV
Na1	Na4	599meV
Na2	Na4	481meV
Na3-1	Na1	540meV
Na2	Na3	344meV
Na3	Na4	685meV
Na4	Na4	544meV

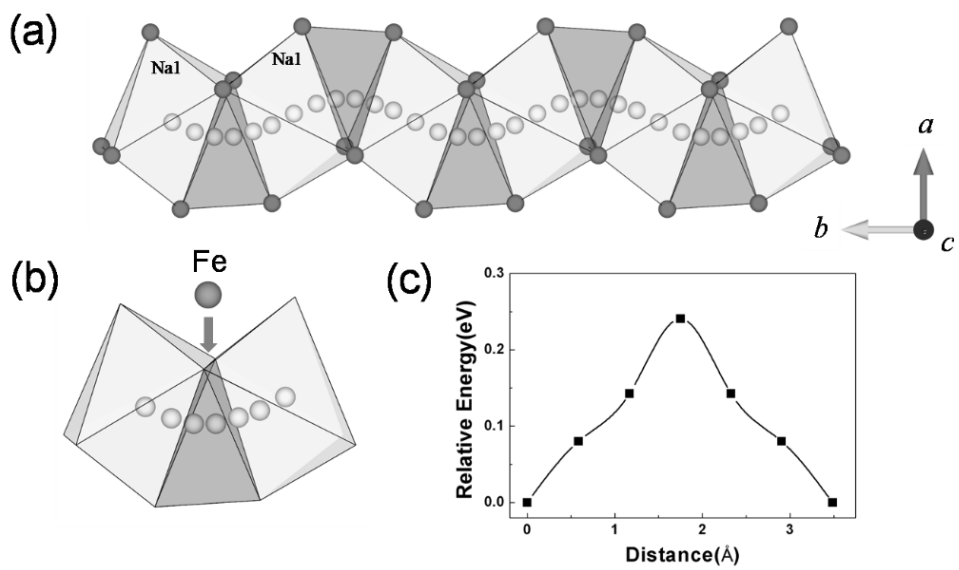


Figure 3-5. Calculated main diffusion motion along the b -axis as illustrated in (a) and (b). (c) The activation barrier of sodium from one Na1 site to another Na1 site.

Inspired by the feasible Na diffusion in the crystal, the electrochemical properties of $\text{Na}_4\text{Fe}_3(\text{PO}_4)_2(\text{P}_2\text{O}_7)$ were tested in a Na cell. The Na cell was fabricated with $\text{Na}_4\text{Fe}_3(\text{PO}_4)_2(\text{P}_2\text{O}_7)$ as the cathode, a sodium counter electrode as the anode, and NaClO_4 in propylene carbonate (PC) as the electrolyte. Figure 3-6a shows the voltage trace as a function of sodium composition for $\text{Na}_x\text{Fe}_3(\text{PO}_4)_2(\text{P}_2\text{O}_7)$ with a 4.3 V cutoff voltage in a Na cell. About 88 % of the theoretical capacity which can be considered as one electron reaction per Fe atom was obtained at the rate of C/40, with an average voltage of ~ 3.2 V. The electrochemical activity centered around 3.2 V is consistent with the theoretical prediction of the voltage from the first principles calculations, as indicated in Figure 3-6a. It is noted that unusually high polarization is observable at the end of the first charge profile. We speculate that this phenomenon can be related to the local structural change occurring around the Na tunnels at the end of the charge. The examination of the structural evolution from first principles calculation reveals that P_2O_7 dimer that constitutes the Na diffusion tunnels in the structure significantly distorts at $1 \leq x \leq 2$ in $\text{Na}_x\text{Fe}_3(\text{PO}_4)_2(\text{P}_2\text{O}_7)$, while the precise relation between P_2O_7 dimer distortion and the Na mobility is currently under investigation. Relatively good cycle performance was observed at both the C/40 rate and C/20 rate, as shown in Figure 3-6b.

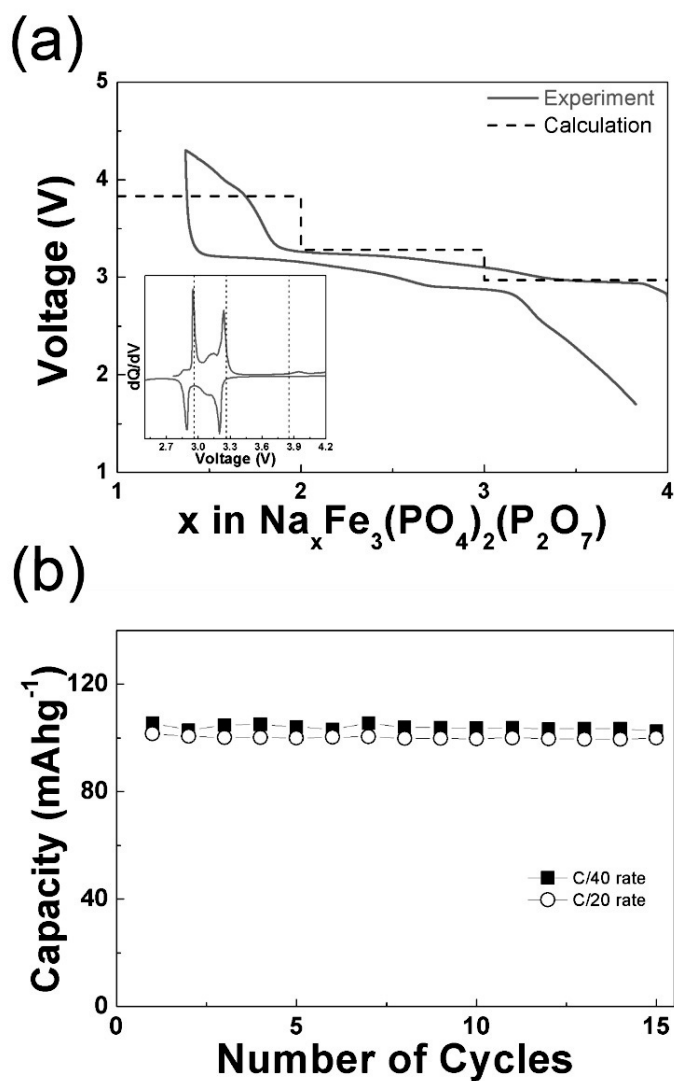


Figure 3-6. (a) Galvanostatic charge/discharge profiles of $\text{Na}_4\text{Fe}_3(\text{PO}_4)_2(\text{P}_2\text{O}_7)$ under a C/40 rate and the calculated average voltage at each region. The inset shows the dQ/dV curve of initial charge/discharge profiles. (b) Cycle performance of a Na cell under C/40 and C/20 rates.

The mechanism by which sodium is extracted from $\text{Na}_4\text{Fe}_3(\text{PO}_4)_2(\text{P}_2\text{O}_7)$ was studied by monitoring Mössbauer spectra and XRD patterns of $\text{Na}_4\text{Fe}_3(\text{PO}_4)_2(\text{P}_2\text{O}_7)$ and fully charged $\text{NaFe}_3(\text{PO}_4)_2(\text{P}_2\text{O}_7)$. Figure 3-7 indicates that the comparison of the XRD patterns of the two samples did not show a significant change; this implies a topotactical de/insertion of the sodium ions. However, a change in the lattice parameters was observed. The values of a , b , and the volume decreased when the three sodium ions were extracted, while the c lattice parameter increased significantly.

The volume change was less than 4 %, which is considerably low compared with other cathode materials.^{3,4,6} The lattice parameters of each phase are tabulated in Table 3-3 along with the ND analysis, which showed the same trend. The comparison of Mössbauer spectra of the two samples clearly indicated that the $\text{Fe}^{2+}/\text{Fe}^{3+}$ redox reaction mainly accompanies the de/sodiation shown in Figure 3-8. Mössbauer analysis in Figure 3-8 confirmed that most of the iron in $\text{Na}_4\text{Fe}_3(\text{PO}_4)_2(\text{P}_2\text{O}_7)$ initially existed as Fe^{2+} . The blue, green, and purple lines in Mössbauer spectra represent the three distinct iron sites. The values of the quadruple splitting (ΔE_Q) and isomer shift (I_S) are in good agreement with those observed in other Fe^{2+} -containing compounds.³⁰ However, when a full charge of $\text{Na}_4\text{Fe}_3(\text{PO}_4)_2(\text{P}_2\text{O}_7)$ is complete, resulting in the formation of $\text{NaFe}_3(\text{PO}_4)_2(\text{P}_2\text{O}_7)$, the ΔE_Q and I_S shift toward values typically observed for Fe^{3+} . A trace amount of Fe^{2+} detected was attributed to the NaFePO_4 impurity, consistent with the ND study. This result agrees with the first principles calculation of the Fe valence states for the two samples. The spin

integration around Fe indicates that the valence of Fe is +2 for the as-prepared sample and +3 for the charged sample, as shown in Figure 3-9. Detailed information on ΔE_Q , the I_S values, and the iron site ratios are provided in Table 3-4.

The thermal phase stability of the charged electrode is one of the indicators that determine the safety characteristics of the battery at elevated temperatures. The charged electrode, $\text{NaFe}_3(\text{PO}_4)_2(\text{P}_2\text{O}_7)$, was further investigated using TGA/ DSC measurements and in situ high-temperature XRD. TGA/ DSC analyses indicate that the desodiated phase was stable up to 500 °C, with only $\sim 4\%$ weight loss (see Figure 3-10). An exothermic peak was observed around 530 °C, where the decomposition into NaFeP_2O_7 and $\text{Fe}_2\text{P}_2\text{O}_7$ was detected from the in situ high-temperature XRD results (see Figure 3-11). The high stability of the $\text{NaFe}_3(\text{PO}_4)_2(\text{P}_2\text{O}_7)$ was comparable to that of charged olivine LiFePO_4 and pyrophosphate $\text{Li}_2\text{FeP}_2\text{O}_7$,^{3,5} presenting intrinsically safe characteristics of polyanion-compound electrodes.

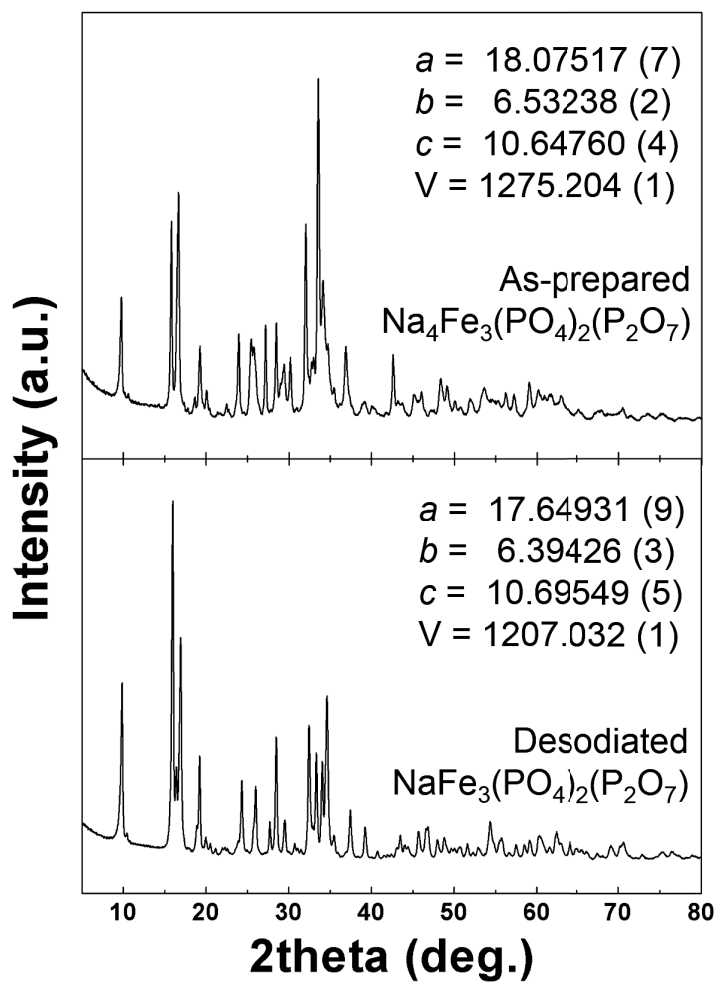


Figure 3-7. XRD patterns of $\text{Na}_x\text{Fe}_3(\text{PO}_4)_2(\text{P}_2\text{O}_7)$ ($x = 1, 4$).

Table 3-3. Lattice parameters of $\text{Na}_x\text{Fe}_3(\text{PO}_4)_2(\text{P}_2\text{O}_7)$ ($x = 4, 1$).

Sample	Source	a (Å)	b (Å)	c (Å)	vol (Å ³)
$\text{Na}_4\text{Fe}_3(\text{PO}_4)_2(\text{P}_2\text{O}_7)$	X-ray	18.0703 (1)	6.53193 (3)	10.64717 (5)	1256.723 (1)
	Neutron	18.07517 (7)	6.53238 (2)	10.64760 (4)	1257.204 (1)
$\text{NaFe}_3(\text{PO}_4)_2(\text{P}_2\text{O}_7)$	X-ray	17.6625(2)	6.39797(5)	10.69996(6)	1209.137 (1)
	Neutron	17.64931(9)	6.39426(3)	10.69549(5)	1207.032 (1)

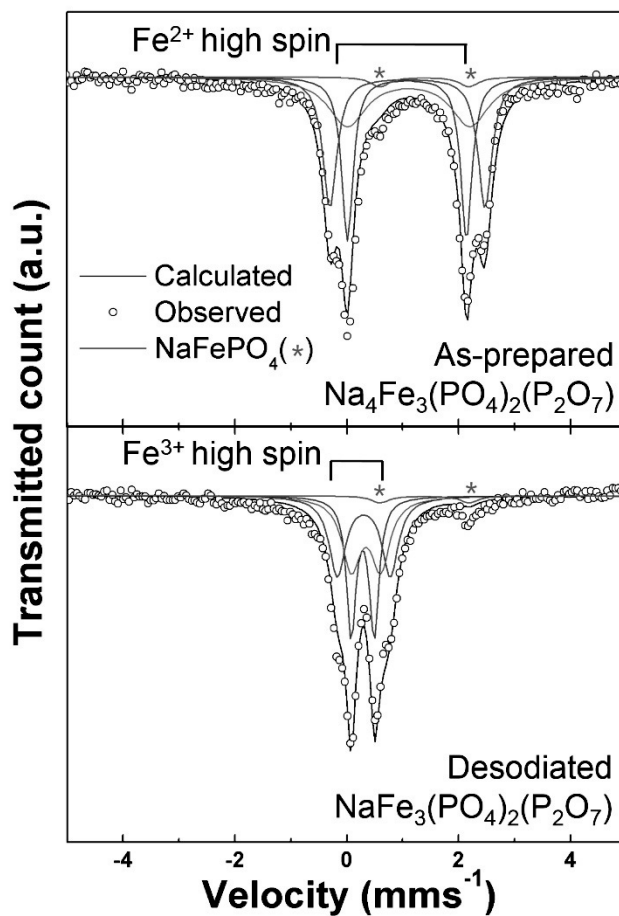


Figure 3-8. Mössbauer spectra of $\text{Na}_x\text{Fe}_3(\text{PO}_4)_2(\text{P}_2\text{O}_7)$ ($x = 1, 4$).

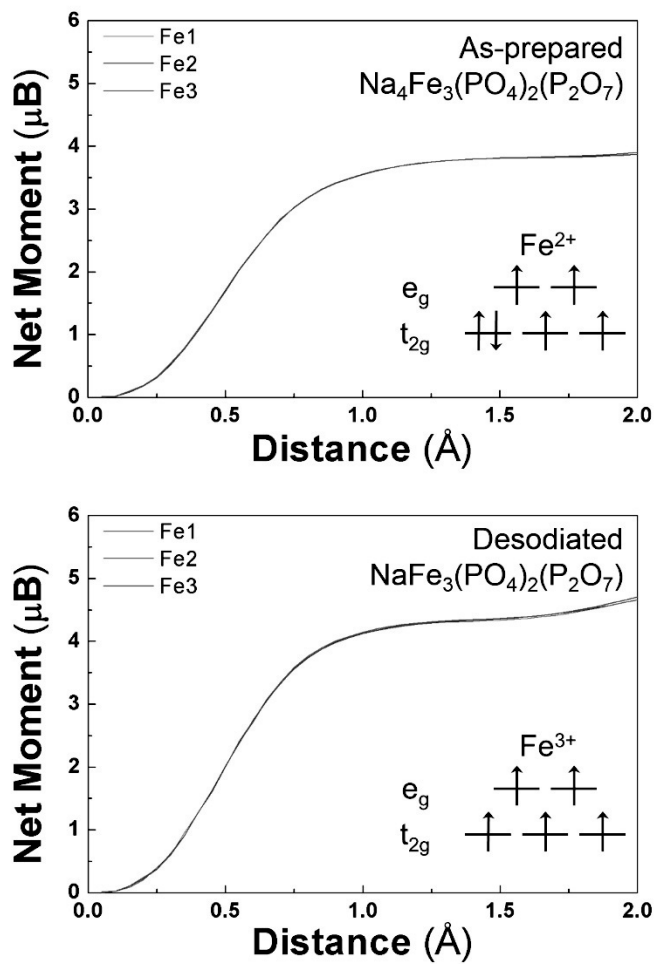


Figure 3-9. Integrated spin as a function of integration radius around Fe in $\text{Na}_{4-x}\text{Fe}_3(\text{PO}_4)_2(\text{P}_2\text{O}_7)$ ($x = 0, 3$).

Table 3-4. Quadruple splitting, isomer shift values, and the ratio of each iron site in $\text{Na}_x\text{Fe}_3(\text{PO}_4)_2(\text{P}_2\text{O}_7)$ ($x = 4, 1$).

$\text{Na}_4\text{Fe}_3(\text{PO}_4)_2(\text{P}_2\text{O}_7)$	ΔE_Q (mm/s)	δ (mm/s)	Ratio (%)
Iron 1	2.1312	1.078	32.26
Iron 2	2.775	1.0875	32.26
Iron 3	2.1941	1.1095	32.26
NaFePO_4	1.5933	1.3917	3.23

$\text{NaFe}_3(\text{PO}_4)_2(\text{P}_2\text{O}_7)$	ΔE_Q (mm/s)	δ (mm/s)	Ratio (%)
Iron 1	0.4104	0.2842	32.26
Iron 2	0.9477	0.3026	32.26
Iron 3	0.5244	0.3413	32.26
NaFePO_4	1.5933	1.3917	3.23

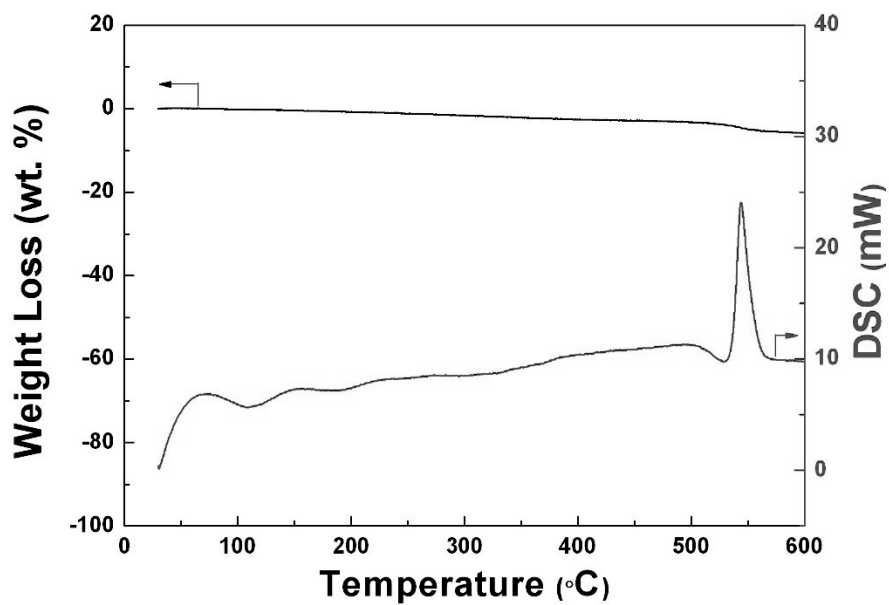


Figure 3-10. TGA/DSC analysis of the desodiated phase of $\text{NaFe}_3(\text{PO}_4)_2(\text{P}_2\text{O}_7)$.

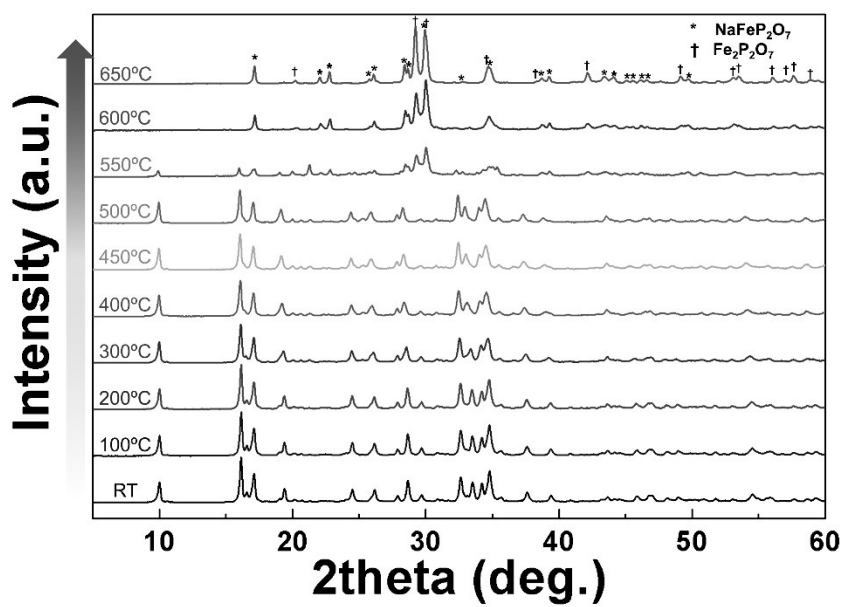


Figure 3-11. *In-situ* high-temperature XRD patterns of $\text{NaFe}_3(\text{PO}_4)_2(\text{P}_2\text{O}_7)$ for a temperature range of 25–650°C under an Ar atmosphere.

The lithium analogue of $\text{Na}_4\text{Fe}_3(\text{PO}_4)_2(\text{P}_2\text{O}_7)$ was produced via a topotactic ion-exchange of the Na cation to the Li cation within the lattice by refluxing in a solution of LiBr. Three Na ions were successfully replaced by Li ions in the lattice, while one Na remained in the structure, resulting in the production of $\text{Li}_3\text{NaFe}_3(\text{PO}_4)_2(\text{P}_2\text{O}_7)$. The Li/Na composition was confirmed to be 3.06:0.9 by inductively coupled plasma-atomic emission spectroscopy (ICP-AES). Figure 3-12a shows the XRD patterns of $\text{Li}_3\text{NaFe}_3(\text{PO}_4)_2(\text{P}_2\text{O}_7)$. The general patterns are similar to those of $\text{Na}_4\text{Fe}_3(\text{PO}_4)_2(\text{P}_2\text{O}_7)$, implying that the crystal framework was maintained. However, the lattice parameters were determined to be smaller, $a = 16.8755$ (7) Å, $b = 6.50413$ (17) Å, and $c = 10.6453$ (3) Å, for $\text{Li}_3\text{NaFe}_3(\text{PO}_4)_2(\text{P}_2\text{O}_7)$ from profile matching, due in part to the smaller ionic radius of Li compared with Na. In particular, a significant reduction of the a lattice was observed. We believe that the replacement of Na with Li in the $(\text{Na}1)\text{O}_6$ and $(\text{Na}4)\text{O}_6$ polyhedra located on the b - c plane caused a significant distortion of the P_2O_7 pillars, which induced the collapse of the interlayer spacing along the a -axis.

Electrochemical measurements on the Li-ion cell were performed with a Li metal anode in a 2016-type coin cell at 298 and 333 K. Figure 3-12b shows the voltage-lithium composition trace of $\text{Li}_3\text{NaFe}_3(\text{PO}_4)_2(\text{P}_2\text{O}_7)$. It should be noted that the electrochemical cycling of $\text{Li}_3\text{NaFe}_3(\text{PO}_4)_2(\text{P}_2\text{O}_7)$ electrode did not show any noticeable change in Na contents. This implies that residual Na may play a role of pillar in the structure. Nevertheless, we believe that various environments such as different C-rates, cutoff voltages, and particle sizes can affect the sodium contents in

the structure of $\text{Li}_3\text{NaFe}_3(\text{PO}_4)_2(\text{P}_2\text{O}_7)$. About 92 % of the theoretical capacity was obtained at a $C/20$ rate with an average voltage of 3.4 V. The electrochemical activity centered around 3.4 V agrees with the voltage trace predicted from the first principles calculations, as indicated in Figure 3-12b. The average voltage of the $\text{Li}_3\text{NaFe}_3(\text{PO}_4)_2(\text{P}_2\text{O}_7)$ is only slightly higher than that of $\text{Na}_4\text{Fe}_3(\text{PO}_4)_2(\text{P}_2\text{O}_7)$. It is attributed to the relative instability of Li ions in the crystal framework which is derived from a parent Na-phase. Relatively good cycle performance was observed, as shown Figure 3-12c. Almost 86 % of the initial discharge capacity was retained at 333 K after 100 cycles. The battery operation at higher current densities showed that ~ 75 % of the initial capacity could be delivered in 1 h (1C rate) and ~ 60 % even in 30 min (2C rate), suggesting that this electrode could sustain respectable rate capabilities (see Figure 3-12d). Note that this electrode was fabricated without any special efforts such as carbon-coating or nanosizing, and there exists about 4% inactive NaFePO_4 impurity. We believe that further synthesis optimization can improve the electrochemical properties significantly. The excellent rate capability and cycle performance was attributed to the open and stable polyanion framework of the electrode material. The open framework is beneficial for fast ion transport, but may, in turn, sacrifice the volumetric energy density for practical use. Nevertheless, comparison with other iron-based polyanion cathodes reported so far showed that the volumetric energy density of $\text{Li}_3\text{NaFe}_3(\text{PO}_4)_2(\text{P}_2\text{O}_7)$ is comparable to them as tabulated in Table S5.

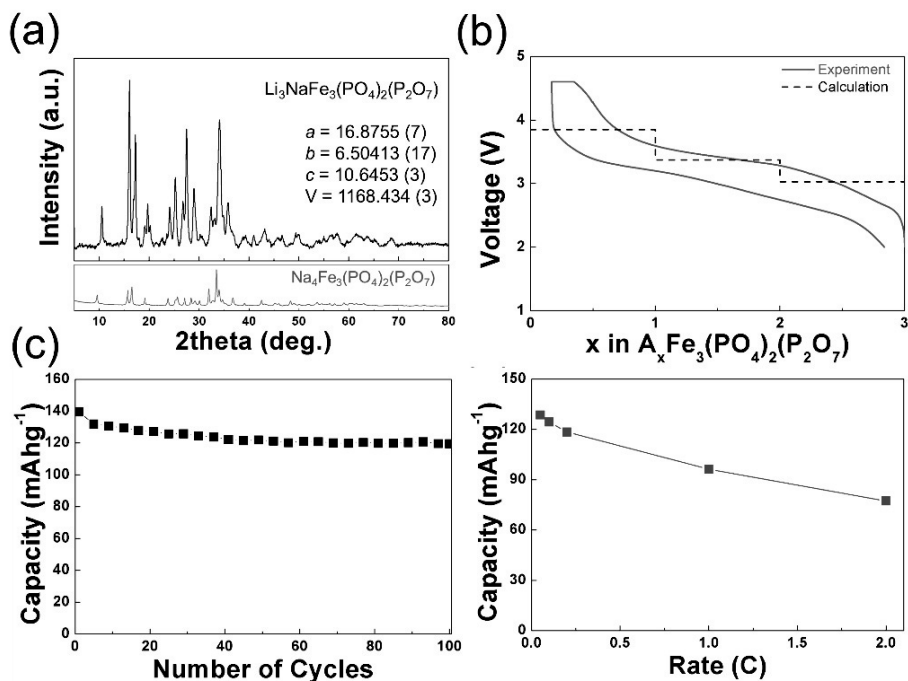


Figure 3-12. (a) XRD patterns of $\text{Li}_3\text{NaFe}_3(\text{PO}_4)_2(\text{P}_2\text{O}_7)$. The reference sodium phase of $\text{Na}_4\text{Fe}_3(\text{PO}_4)_2(\text{P}_2\text{O}_7)$ is represented below. (b) Calculated voltage and galvanostatic charge/discharge profiles of the Li cell under a C/20 rate at 298 K and calculated voltage profiles; (c) cyclability of the Li-ion cell under C/5 at 333 K. (d) The rate capability of $\text{Li}_3\text{NaFe}_3(\text{PO}_4)_2(\text{P}_2\text{O}_7)$ in the Li-ion cell.

Table 3-5. Volumetric energy density of iron-based polyanion compounds.

Designation	Voltage	Volumetric energy density	References
$\text{Li}_3\text{NaFe}_3(\text{PO}_4)_2(\text{P}_2\text{O}_7)$	3.4V	1550Wh/L	This work
Pyrophosphate, $\text{Li}_2\text{FeP}_2\text{O}_7$	3.5V	1200Wh/L	Ref. 1
$\text{Li}_2\text{FePO}_4\text{F}$	3.3V	1550Wh/L	Ref. 6
Tavorite, LiFeSO_4F	3.6V	1750Wh/L	Ref. 10
Tavorite, LiFePO_4F	2.75V	1290Wh/L	Ref. 31
Tavorite, LiFePO_4OH	2.4V	1220Wh/L	Ref. 32
Silicate, $\text{Li}_2\text{FeSiO}_4$	2.85V	1510Wh/L	Ref. 8
Olivine, LiFePO_4	3.3V	2010Wh/L	Ref. 2
$\text{Li}_3\text{Fe}_2(\text{PO}_4)_3$	2.8V	1110Wh/L	Ref. 13
LiFeP_2O_7	2.9V	1020Wh/L	

3.4 Conclusion

In conclusion, new mixed-polyanion-based compounds, $\text{Li}_x\text{Na}_{4-x}\text{Fe}_3(\text{PO}_4)_2(\text{P}_2\text{O}_7)$ ($x = 0, 3$), were successfully synthesized, and their energy densities were 380 and 460 Wh kg^{-1} in sodium- and lithium-ion batteries, respectively. The respectable cathode activity in both sodium- and lithium-ion batteries was delivered without special efforts, such as carbon coating or nano-sizing. The combined $(\text{PO}_4)^{3-}$ and $(\text{P}_2\text{O}_7)^{4-}$ polyanion groups, which provided a new crystal framework that accommodated the naturally abundant Fe redox center and lithium/sodium ions, exhibited stable and fast cathode activity in lithium and sodium batteries. The emerging rich chemistry in mixed-polyanion materials suggests that significant opportunity exists to explore new low-cost, high-performance electrodes in this class of materials.

3.5 References

- (1) S. Nishimura, M. Nakamura, R. Natsui, A. Yamada, *J. Am. Chem. Soc.* **2010**, *132* (39), 13596–13597.
- (2) A. K. Padhi, K. Nanjundaswamy, J. B. Goodenough, *J. Electrochem. Soc.* **1997**, *144* (4), 1188–1194.
- (3) C. Delacourt, P. Poizot, J. -M. Tarascon, C. Masquelier, *Nat. Mater.* **2005**, *4*, 254–260.
- (4) B. L. Ellis, W. R. Makahnouk, Y. Makimura, K. Toghill, L. F. Nazar, *Nat. Mater.* **2007**, *6* (10), 749–753.
- (5) H. Kim, S. Lee, Y. -U. Park, H. Kim, J. Kim, S. Jeon, K. Kang, *Chem. Mater.* **2011**, *23* (17), 3930–3937.
- (6) N. Recham, J. -N. Chotard, L. Dupont, C. Delacourt, W. Walker, M. Armand, J. -M. Tarascon, *Nat. Mater.* **2009**, *9* (1), 68–74.
- (7) P. Barpanda, M. Ati, B. C. Melot, G. Rousse, J. N. Chotard, M. L. Doublet, M. T. Sougrati, S. -A. Corr, J. C. Jumas, J. -M. Tarascon, *Nat. Mater.* **2011**, *10* (10), 772–779.
- (8) A. Nyten, A. Abouimrane, M. Armand, T. Gustafsson, J. O. Thomas, *Electrochem. Commun.* **2005**, *7* (2), 156–160.
- (9) A. Yamada, N. Iwane, Y. Harada, S. -i. Nishimura, Y. Koyama, I. Tanaka, *Adv. Mater.* **2010**, *22* (32), 3583–3587.

- (10) D.-H. Seo, Y. -U. Park, S. -W. Kim, I. Park, R. Shakoob, K. Kang, *Phy. Rev. B* **2011**, *83*, 205127–1–8.
- (11) T. N. Ramesh, K. T. Lee, B. L. Ellis, L. F. Nazar, *Electrochem. Solid-State Lett.* **2010**, *13* (4), A43–A47.
- (12) B. L. Ellis, T. N. Ramesh, W. N. Rowan-Weetaluktuk, D. H. Ryan, L. F. Nazar, *J. Mater. Chem.* **2012**, *22*, 4759–4766.
- (13) A. K. Paldi, K. S. Nanjundaswamy, C. Masquelier, S. Okada, J. B. Goodenough, *J. Electrochem. Soc.* **1997**, *144* (5), 1609–1613.
- (14) A. K. Padhi, V. Manivannan, J. B. Goodenough, *J. Electrochem. Soc.* **1998**, *145* (5), 1518–1520.
- (15) G. Hautier, A. Jain, H. Chen, C. Moore, S. P. Ong, G. Ceder, *J. Mater. Chem.* **2011**, *21* (43), 17147–17153.
- (16) A. Jain, G. Hautier, C. Moore, B. Kang, J. Lee, H. Chen, N. Twu, G. Ceder, *J. Electrochem. Soc.* **2012**, *159* (5), 622–633.
- (17) Q. Kuang, J. Xu, Y. Zhao, X. Chen, L. Chen, *Electrochim. Acta* **2011**, *56* (5), 2201–2205.
- (18) Q. Kuang, Z. Lin, Y. Zhao, X. Chen, L. Chen, *J. Mater. Chem.* **2011**, *21* (38), 14760–15765.
- (19) F. Sanz, C. Parada, J. Rojo, C. Ruiz-Valero, *Chem. Mater.* **2001**, *13* (4), 1334–1340.

- (20) R. Essehli, E. B. Bali, S. Benmokhtar, H. Fuess, I. Svoboda, S. Obbade, *J. Alloys Compd.* **2010**, 493 (1), 654–660.
- (21) A. R. Wizansky, P. E. Rauch, F. J. DiSalvo, *J. Solid State. Chem.* **1989**, 81, 203–207.
- (22) S. -W. Kim, J. Kim, H. Gwon, K. Kang, *J. Electrochem. Soc.* **2009**, 156 (8), A635–A638.
- (23) T. Roisnel, J. Rodriguez-Carvajal, *Transtec Publications*; 1999: **2001**, 118–123.
- (24) G. Kresse, J. Furthmuller, *Comput. Mater. Sci.* **1996**, 6, 15.
- (25) J. P. Perdew, K. Burke, M. Ernzerhof, *Phys. Rev. Lett.* **1996**, 77, 3865.
- (26) V. I. Anisimov, J. Zaanen, O. K. Andersen, *Phys. Rev. B* **1991**, 44, 943.
- (27) V. I. Anisimov, F. Aryasetiawan, A. I. Lichtenstein, *J. Phys. Condens. Matter* **1997**, 9, 767.
- (28) H. Jonsson, G. Mills, K. W. Jacobsen, B. J. Berne, title. in *Classical and Quantum Dynamics in Condensed Phase Simulations*, edited by D. Chandler, B. J. Berne, G. Ciccotti, & D. F. Coker (World Scientific, Singapore, 1998), p. 385
- (29) S. -i Nishimura, G. Kobayashi. K. Ohoyama, R. Kanno, M. Yashima, A. Yamada, *Nat. Mater.* **2008**, 7, 707–711.
- (30) A.-S. Andersson, B. Kalska, L. Haggström, J. -O. Thomas, *Solid State Ionics* **2000**, 130 (1), 41–52.

(31) N. Recham, J. -N. Chotard, J. -C. Jumas, L. Laffont, M. Armand, J. -M. Tarascon, *Chem. Mater.* **2010**, *22* (3), 1142-1148.

(32) M. S. Whittingham, Y. Song, S. Lutta, P. -Y. Zavalij, N. -A. Chernova, *J. Mater. Chem.* **2005**, *15*, 3362-3379.

Chapter 4. Understanding the electrochemical mechanism of the new iron-based mixed-phosphate $\text{Na}_4\text{Fe}_3(\text{PO}_4)_2(\text{P}_2\text{O}_7)$ in a Na rechargeable battery

(The content of this chapter has been published in *Chemistry of Materials*. Reprinted with permission from [H. Kim et al., *Chem. Mater.* **2013**, 25 (18), 3614-3622.]. Copyright (2013) American Chemical Society.)

4.1 Introduction

Storing the energy from sustainable but intermittent resources, such as solar and wind energy, in a large-scale energy storage system (ESS) has become a critical issue in recent years. Although the Li rechargeable battery has been a great success in small portable electronics, and is on the verge of being used in mid-size applications such as hybrid electric vehicles (HEVs) and electric vehicles (EVs),¹⁻³ great challenges remain in its application to large-scale ESSs. In order to develop a stationary ESS connected to green and sustainable energy generators beyond the scale of HEVs and EVs, cost effectiveness is of foremost importance. While the significant cost reduction in cell making or maintenance would greatly benefit the development, in the aspects of material cost, batteries that are based on earth-abundant, readily available, and low-cost elements are highly desirable for large-scale ESSs. In particular, electrochemistry that utilizes an iron-based redox reaction combined with Na guest ions would be an

optimal choice for such batteries because of the nearly unlimited availability of Na from seawater and the ready availability of iron. The intensive effort is focused on the development of new low-cost electrode materials. However, only a limited number of such materials has been reported to date (NaFePO₄, Na₂FePO₄F, NaFeSO₄F, and Na₂FeP₂O₇).⁴⁻⁹

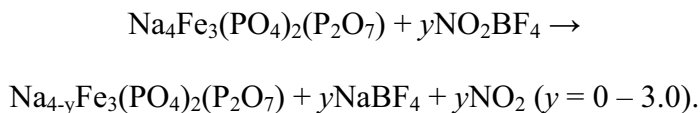
Recently, we reported a new iron-based mixed-polyanion compound, Na₄Fe₃(PO₄)₂(P₂O₇), that shows promising electrochemical properties in both Na- and Li-ion cells.¹⁰ A Na₄Fe₃(PO₄)₂(P₂O₇) electrode in a Na-ion cell exhibited an average voltage of 3.2 V (vs. Na), which is high compared to other polyanion-based cathodes, with a theoretical capacity of 129 mAhg⁻¹.⁴⁻⁹ Also, the open framework with three-dimensional (3D) Na channels enabled nearly full utilization of the theoretical capacity at reasonable current densities. However, a fundamental understanding of the electrochemical reaction mechanism and structural stability under various conditions, which is essential for further development of this promising cathode, had not yet been achieved.

Because the electrochemical reaction of a mixed-polyanion compound with a generally complex crystal structure may involve a complex structural evolution, we carefully combined neutron diffraction (ND), XRD, X-ray absorption spectroscopy (XAS), and first principles calculations for a structural characterization of Na_xFe₃(PO₄)₂(P₂O₇) (1 ≤ x ≤ 4). We discovered that the redox reaction of Na_xFe₃(PO₄)₂(P₂O₇) in a Na-ion cell occurs mainly *via* a one-phase reaction with a small volumetric change of less than 4 %, despite significant distortion of the pyrophosphate (P₂O₇) polyhedron occurring upon electrochemical cycling. Furthermore, the charged Na_xFe₃(PO₄)₂(P₂O₇) (x < 4)

electrode is thermally stable at temperatures of more than 500 °C, irrespective of the state of charge (SOC).

4.2 Experimental

Synthesis of $\text{Na}_x\text{Fe}_3(\text{PO}_4)_2(\text{P}_2\text{O}_7)$ ($1 \leq x \leq 4$): $\text{Na}_4\text{Fe}_3(\text{PO}_4)_2(\text{P}_2\text{O}_7)$ was synthesized *via* a conventional two-step solid-state method. The starting materials, $\text{Na}_4\text{P}_2\text{O}_7$ (95 %, Aldrich), $\text{Fe}_2\text{C}_2\text{O}_4 \cdot 2\text{H}_2\text{O}$ (99 %, Aldrich), and $\text{NH}_4\text{H}_2\text{PO}_4$ (98 % ACS reagent, Aldrich), were mixed by ball milling with acetone for 24 h and dried at 70 °C for 12 h. The mixture was sintered at 300 °C for 6 h under flowing Ar. The calcined powder was then reground and pelletized under a pressure of 200 kg cm⁻² using a disk-shaped mold. The pelletized sample was again sintered at 500 °C for 12 h under an Ar flow. Desodiated samples, $\text{Na}_x\text{Fe}_3(\text{PO}_4)_2(\text{P}_2\text{O}_7)$ ($x < 4.0$), were prepared using stoichiometric amounts of $y\text{NO}_2\text{BF}_4$ (95 %, Aldrich, $y = 0 - 3.0$) in acetonitrile solvent (anhydrous, 99.8 %, Aldrich) according to the following reaction:



NO_2BF_4 is a strong oxidizing agent equivalent to a 4.8 V potential versus Na^+/Na .¹¹ The solution was maintained at 60 °C for 12 h. Final products of the desodiated phases were obtained by washing with acetonitrile using a centrifuge.

Characterization: *Ex situ* XRD patterns of $\text{Na}_x\text{Fe}_3(\text{PO}_4)_2(\text{P}_2\text{O}_7)$ ($x = 1 - 4$) were recorded using an X-ray diffractometer (Bruker, D2 PHASER) with Cu K α radiation ($\lambda = 1.5406 \text{ \AA}$). Each dataset was obtained over a 2θ range of 5 – 60 °

with a 0.01 step per 1.2 s. ND data of $\text{NaFe}_3(\text{PO}_4)_2(\text{P}_2\text{O}_7)$ were collected using a high-resolution powder diffractometer (HRPD) at the HANARO facility of the Korea Atomic Energy Research Institute. Data were recorded over a 2θ range of $0 - 180^\circ$ with a step size of 0.05° . A constant wavelength of $\lambda = 1.834333 \text{ \AA}$ was supplied by a Ge (331) single-crystal monochromator. *In situ* high-temperature XRD patterns were obtained over a 2θ range of $5 - 60^\circ$ with a scan rate of 1° min^{-1} at each temperature (room temperature $\sim 650^\circ\text{C}$) using an X-ray diffractometer (Rigaku, D/MAX 2500). Particle size and crystallinity were examined by field-emission scanning electron microscopy (FESEM, SUPRA 55VP/Carl Zeiss) and transmission electron microscopy (TEM, Tecnal F20/FEI).

The valence states of iron in $\text{Na}_x\text{Fe}_3(\text{PO}_4)_2(\text{P}_2\text{O}_7)$ ($x = 1 - 4$) samples were investigated by X-ray absorption near-edge structure (XANES) analysis. The XAS experiments were performed at beamline 8C at the Pohang Accelerator Laboratory (PAL), Republic of Korea. Fe K-edge XANES spectra of $\text{Na}_x\text{Fe}_3(\text{PO}_4)_2(\text{P}_2\text{O}_7)$ ($x = 1 - 4$) samples were obtained in the transmission mode with an electron energy of 2.5 GeV and stored in the current range of 100 – 150 mA. Fe K-edge energy calibration was performed using Fe metal foil as a reference. A reference spectrum was simultaneously recorded for the *in situ* spectrum using Fe metal foil.

The structural stability of desodiated samples was investigated by DSC under an Ar atmosphere at a heating rate of $10^\circ\text{C min}^{-1}$ from room temperature

to 650 °C using a SETSYS 16/18 thermogravimetric analyzer (SETARAM, France). Atomic ratios of Na to Fe in the powdered sample of $\text{Na}_x\text{Fe}_3(\text{PO}_4)_2(\text{P}_2\text{O}_7)$ ($x = 1 - 4$) were determined by inductively coupled plasma-atomic emission spectroscopy (ICP-AES, Thermo Jarrel Ash, Polyscan 60E, USA).

First-principles calculation method: All *ab initio* calculations were performed with density functional theory (DFT) using the spin-polarized generalized-gradient approximation (GGA) from Perdew–Burke–Ernzerhof (PBE) and a Hubbard U parameter for Fe.^{12–15} Additional details about the general method and parameters can be found in previous work.¹⁰

The crystal structure and Na/vacancy ordering of $\text{Na}_x\text{Fe}_3(\text{PO}_4)_2(\text{P}_2\text{O}_7)$ ($x = 1, 2, 3$) were evaluated by the *convex hull methodology*, which has been frequently used to evaluate the thermodynamic stability of intercalation compounds in battery fields.^{16–19} We computed the *ab initio* energies of the 50 unique Na/vacancy orderings, which have been selected out of more than 8,000 random Na / vacancy orderings based on electrostatic energy calculations (by Ewald summation method²⁰) for each integer x in $\text{Na}_x\text{Fe}_3(\text{PO}_4)_2(\text{P}_2\text{O}_7)$. Even though it is not as comprehensive as methods such as cluster expansions,^{21,22} we believe 50 most plausible orderings out of $\sim 8,000$ candidates based on electrostatic energy are the reasonable starting points for further *ab initio* calculations considering the heavy computational costs.

Electrochemical tests: Electrodes were fabricated using the active material $\text{Na}_4\text{Fe}_3(\text{PO}_4)_2(\text{P}_2\text{O}_7)$, super P, and polyvinylidene fluoride (PVDF) at a weight ratio of 70:20:10 in N-methyl-2-pyrrolidone (NMP) (99.5 %, Aldrich) solvent. The mixed slurry was pasted onto Al foil, and the NMP was allowed to evaporate at 120 °C for 3 h. The Na-ion cell was assembled in a CR2016-type coin cell in an Ar-filled glove box using sodium metal (sodium cube 99 %, Aldrich) as an anode and propylene carbonate (anhydrous 99.9 %, Aldrich) with 1 mol of NaClO_4 (99 %, Aldrich) as an electrolyte. A Celgard 2400 separator was used. Galvanostatic charge/discharge measurements were conducted at various C-rates (C/20, C/10 and C/5). The C-rate is based on the theoretical capacity of 129mAh g^{-1} , which corresponds to 3 Na extraction / insertion of $\text{Na}_4\text{Fe}_3(\text{PO}_4)_2(\text{P}_2\text{O}_7)$. Current densities for C/20, C/10 and C/5 rate measurements were 0.0117 mA cm^{-2} , 0.0240 mA cm^{-2} and 0.042 mA cm^{-2} , respectively. The loading amount of active materials pasted onto an Al electrode was about 2 mg cm^{-2} . *Ex situ* electrode samples were prepared in different charge and discharge states. Each sample was collected at a certain cut-off voltage with a 12 h relaxation time to measure the quasi-equilibrium state of the electrodes. Potentiostatic intermittent titration technique (PITT) measurements were carried out using a voltage step of 5 mV. The cut-off current in each individual titration corresponded to that of the C/50 rate. The voltage range for the PITT measurements was 2.0 – 4.3 V.

4.3 Results and Discussion

$\text{Na}_4\text{Fe}_3(\text{PO}_4)_2(\text{P}_2\text{O}_7)$ was successfully synthesized using conventional solid-state methods at 500 °C. Rietveld refinement of the XRD pattern in Figure 4-1a confirmed that the structure of the as-prepared $\text{Na}_4\text{Fe}_3(\text{PO}_4)_2(\text{P}_2\text{O}_7)$ can be indexed with the orthorhombic $Pn2_1a$ space group.¹⁰ The lattice parameters were $a = 18.03744$ (11) Å, $b = 6.52727$ (4) Å, $c = 10.64413$ (7) Å, and $V = 1253.189$ (1) Å³, which is comparable to those of the previous study, with low R-factors of $R_p = 5.65$ %, $R_l = 3.44$ %, and $R_F = 2.14$ %.¹⁰ A trace amount of maricite (NaFePO_4) impurity (~4 wt%) was detected. The SEM and TEM analyses in Figure 4-2a and b show that the particle sizes of the crystalline $\text{Na}_4\text{Fe}_3(\text{PO}_4)_2(\text{P}_2\text{O}_7)$ were about 100 – 200 nm.

The electrochemical properties of the $\text{Na}_4\text{Fe}_3(\text{PO}_4)_2(\text{P}_2\text{O}_7)$ electrode in a Na-ion cell were examined at a C/20 rate in Figure 4-1b. The red and blue lines present the first and second charge/discharge profiles, respectively. About 82 % of the theoretical capacity was obtained at a C/20 rate with relatively good cycle stability. Good cycle performance was also observed at higher C-rates (C/20, C/10, and C/5) with only slight reduction of capacity, as shown in the inset of Figure 4-1 b.

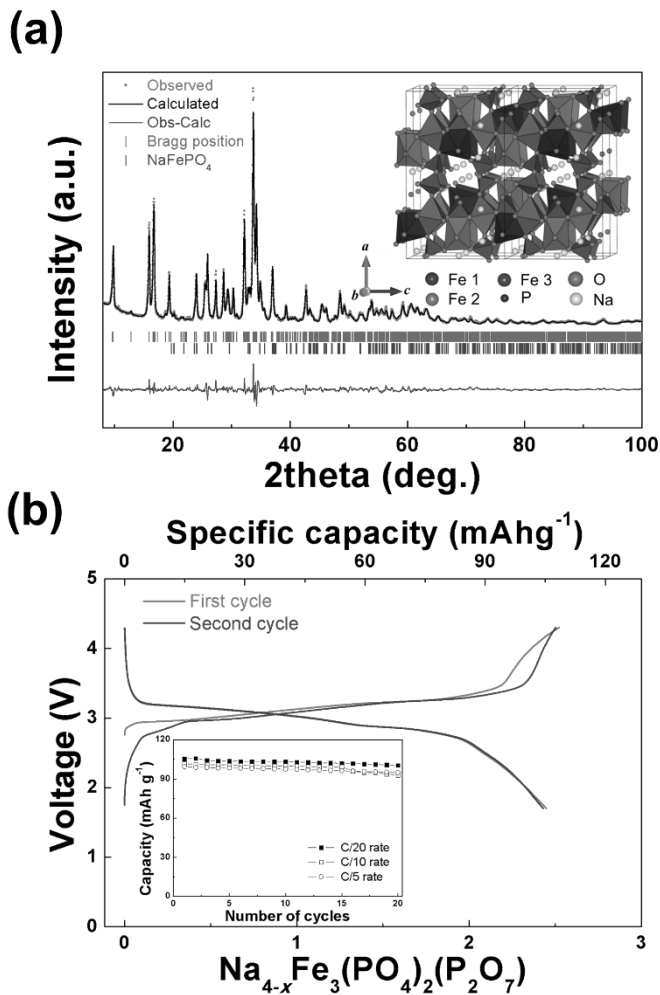


Figure 4-1. (a) Rietveld refinement of Na₄Fe₃(PO₄)₂(P₂O₇) using XRD. A schematic representation of Na₄Fe₃(PO₄)₂(P₂O₇) is illustrated in the inset. (b) Galvanostatic charge/discharge profiles of Na₄Fe₃(PO₄)₂(P₂O₇) in a Na-ion cell at the C/20 rate. The inset presents the cycle performance at various C-rates (C/20, C/10, and C/5).

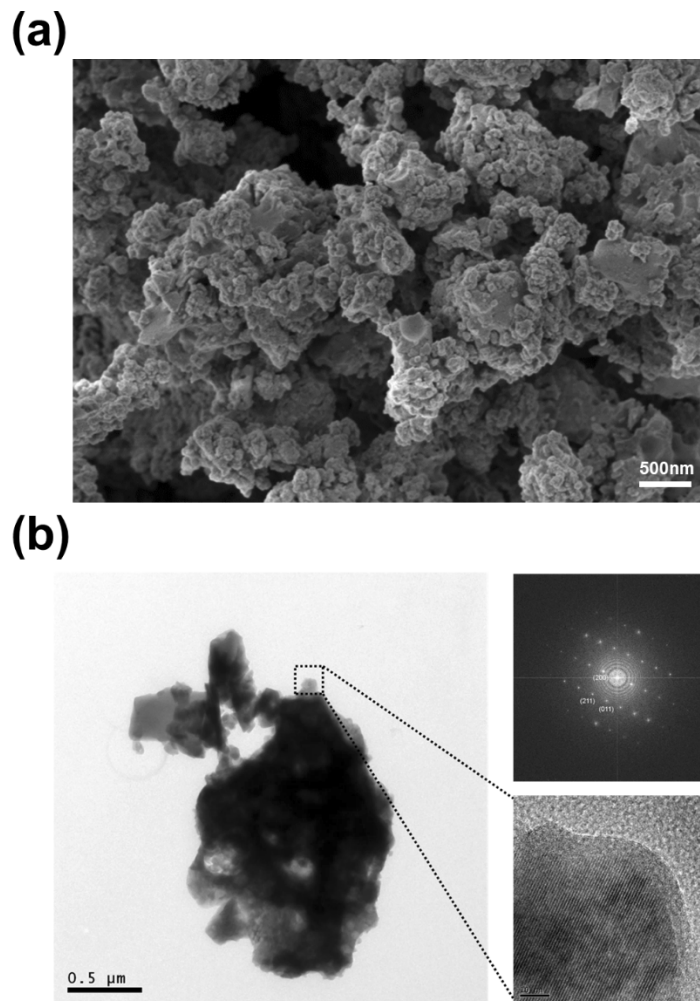


Figure 4-2. (a) Scanning electron microscopy (SEM) and (b) transmission electron microscopy (TEM) images of $\text{Na}_4\text{Fe}_3(\text{PO}_4)_2(\text{P}_2\text{O}_7)$ showing that the primary particle sizes are about 100 – 200 nm and that the crystallinity is good.

The structural evolution of the electrode material during cycling was analyzed by collecting electrodes at different states of charge in the first two cycles. Figure 4-3a shows *ex situ* XRD patterns of $\text{Na}_x\text{Fe}_3(\text{PO}_4)_2(\text{P}_2\text{O}_7)$ during the charge/discharge process. Although the general patterns remained unchanged, implying a topotactic Na extraction from the mother structure, noticeable peak shifts of (200) and changes in peak intensity ratios, such as (011) / (210), were observed during the charge. The subsequent discharge to 1.7 V and further charge resulted in a completely reversible structural evolution. Closer examination of the amplified XRD patterns in the 2θ range of 8 to 19 ° in Figure 4-3b clearly shows peak shifts during the electrochemical reaction. Major peaks such as (200), (011), (002), and (210) gradually move to higher 2θ during Na extraction and return to their original values during reinsertion, which was attributed to continuous lattice volume change during cycling. The continuous peak shift in the series of *ex situ* XRD measurements is an indication of a one-phase-based electrochemical reaction of the $\text{Na}_x\text{Fe}_3(\text{PO}_4)_2(\text{P}_2\text{O}_7)$ electrode in a Na rechargeable battery. This behavior is in clear contrast to those of simple polyanion compounds based on a similar Fe redox reaction, such as olivine NaFePO_4 and $\text{Na}_2\text{FeP}_2\text{O}_7$, which are known to exhibit biphasic electrochemical reaction in Na-ion cells.^{5,9}

For further structural characterization, we also prepared $\text{Na}_x\text{Fe}_3(\text{PO}_4)_2(\text{P}_2\text{O}_7)$ ($1 \leq x \leq 4$) samples from the chemical desodiation process. The XRD patterns of chemically prepared phases in Figure 4-4 show identical peak shifts and

intensity ratios as the *ex situ* XRD results. In Figure 4-5(a–d), the lattice parameters of chemically and electrochemically desodiated samples are plotted as a function of Na content; both show good agreement. Additionally, the figure shows the lattice parameters from first principles calculations. Experimental and theoretical quantification showed that a , b , and V (lattice volume) linearly decrease upon Na extraction from $\text{Na}_4\text{Fe}_3(\text{PO}_4)_2(\text{P}_2\text{O}_7)$. This confirms again that the $\text{Na}_x\text{Fe}_3(\text{PO}_4)_2(\text{P}_2\text{O}_7)$ electrode operates *via* a one-phase reaction during electrochemical cycling. However, we note that the c lattice parameter linearly increases up to $x \sim 2$ but suddenly collapses at $x \sim 1$, contrary to the behavior of the a and b lattice parameters. This unusual phenomenon was reversibly observed from *ex situ* electrodes, as shown in Figure 4-6(a–d), and will be discussed later. Nevertheless, it is noteworthy that the volumetric change with the full charge and discharge is less than 4 %, which is one of the smallest volume changes reported for Na battery cathodes.^{4–9} This small volume change is expected to contribute the stable cycle property as shown in Figure 4-1b. While the most of Na intercalation compounds show inherently large volumetric change during cycling due to large ionic size of Na compared to typical Li intercalation compounds, less than 4% volume change is remarkably small. We attributed this small volume change to the open and rigid framework of mixed polyanion crystal structure and believe this is one of the most important advantages of using mixed polyanion compounds as Na cathode materials.

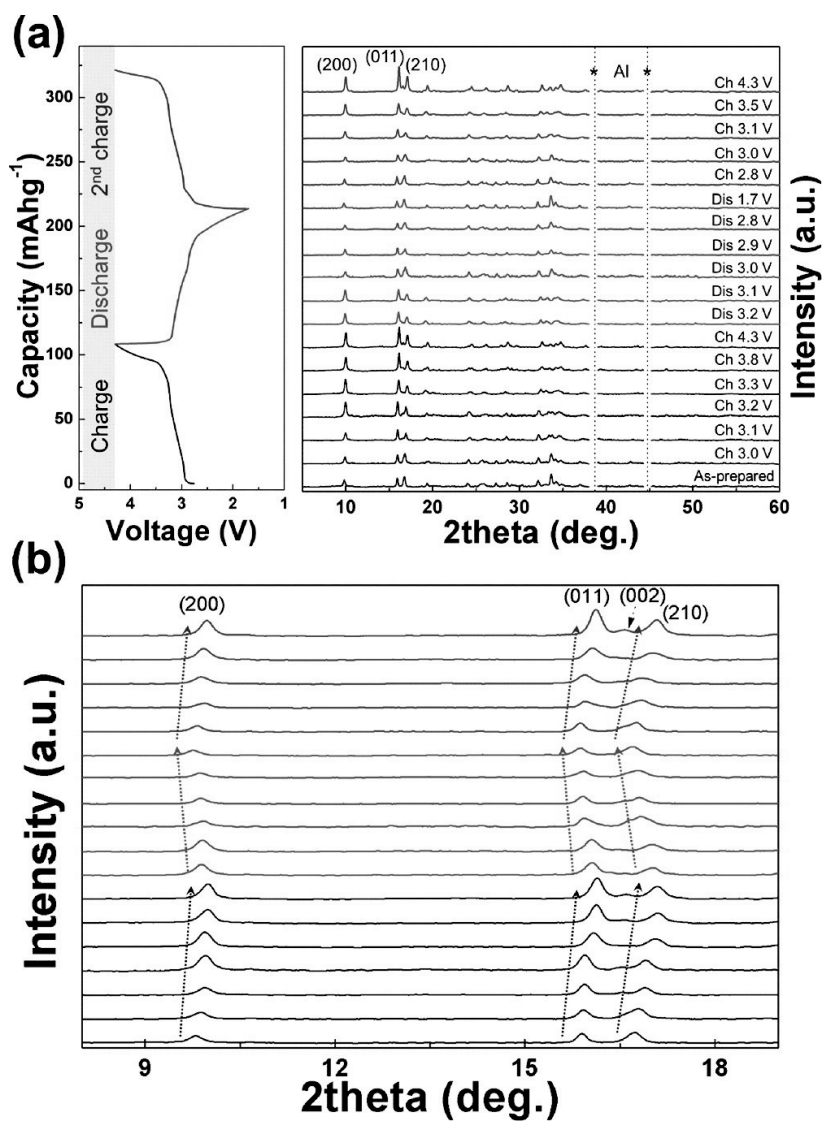


Figure 4-3. (a) *Ex situ* XRD patterns of $\text{Na}_4\text{Fe}_3(\text{PO}_4)_2(\text{P}_2\text{O}_7)$ in a Na-ion cell during the charge/discharge process. Amplified XRD patterns in the 2θ range of 8 to 19° are illustrated in (b).

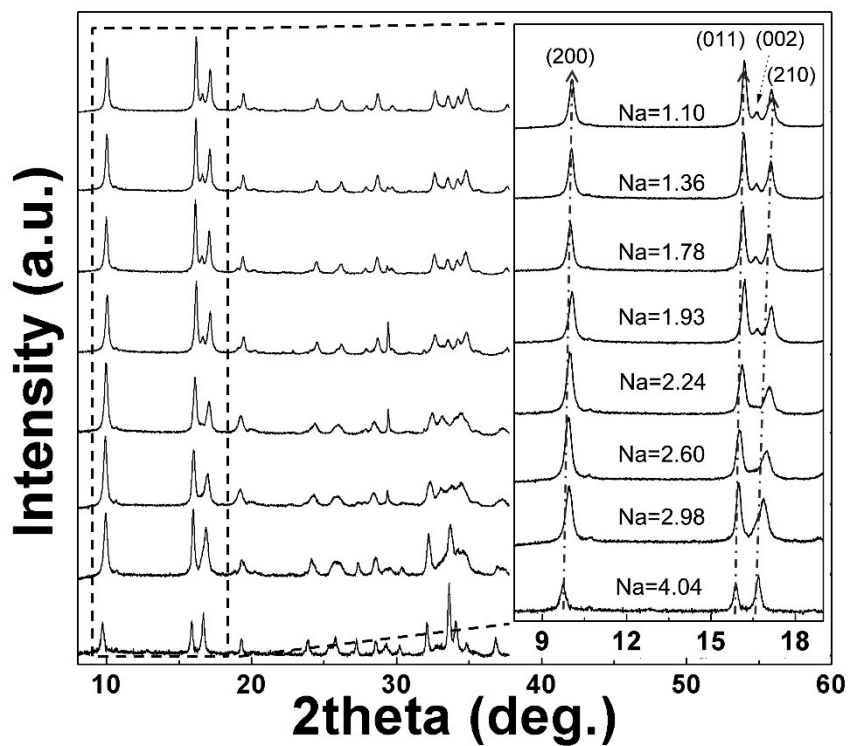


Figure 4-4. X-ray diffraction (XRD) patterns of $\text{Na}_x\text{Fe}_3(\text{PO}_4)_2(\text{P}_2\text{O}_7)$ ($1 \leq x \leq 4$) powder samples synthesized by chemical desodiation.

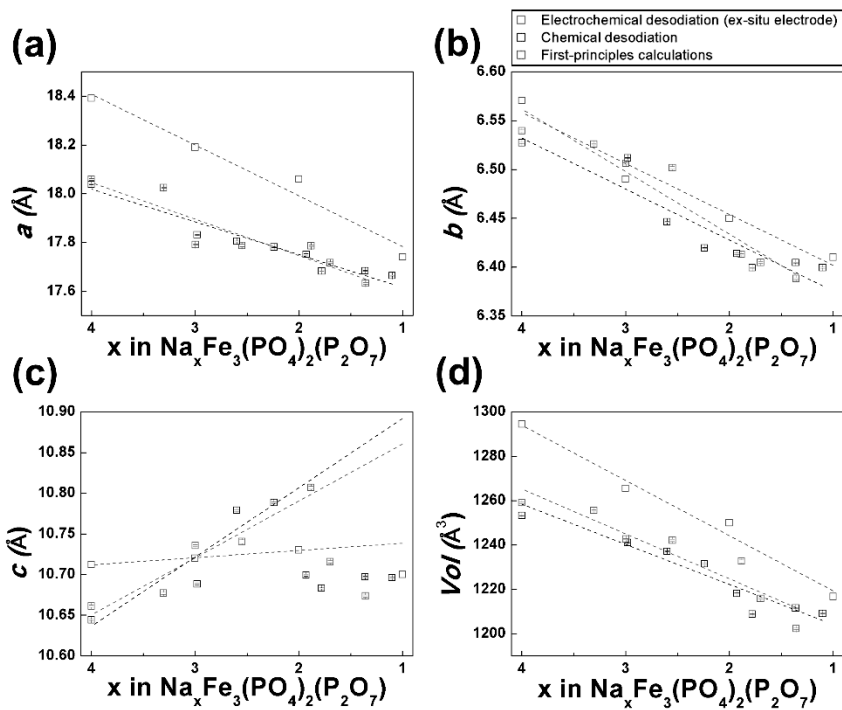


Figure 4-5. (a) a , (b) b , (c) c lattice parameters and (d) lattice volume change of $\text{Na}_x\text{Fe}_3(\text{PO}_4)_2(\text{P}_2\text{O}_7)$ as a function of Na composition (x).

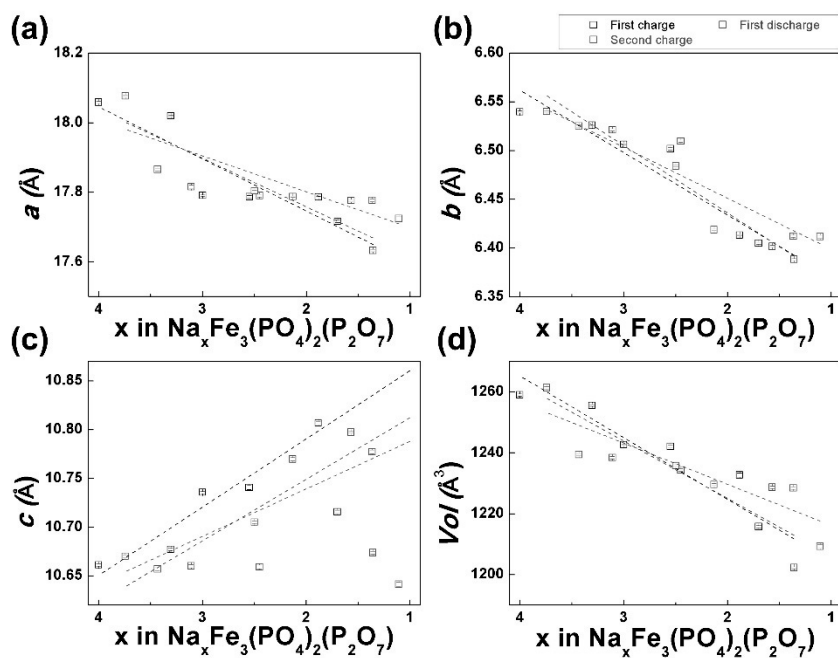


Figure 4-6. (a) a , (b) b , (c) c lattice parameters, and (d) lattice volume change of $\text{Na}_x\text{Fe}_3(\text{PO}_4)_2(\text{P}_2\text{O}_7)$ as a function of Na composition (x). The black, blue, and red rectangle markers represent the lattice parameters of *ex situ* electrode samples during the initial charge, discharge, and second charge, respectively.

To understand the structural evolution during charge and discharge, we carefully investigated the intermediate states of $\text{Na}_x\text{Fe}_3(\text{PO}_4)_2(\text{P}_2\text{O}_7)$ ($x = 1 - 4$) using first principles calculations at each Na content. Figure 4-7 shows the formation energies of $\text{Na}_x\text{Fe}_3(\text{PO}_4)_2(\text{P}_2\text{O}_7)$ structures with various Na-vacancy configurations as a function of Na composition. The convex hull $\text{Na}_x\text{Fe}_3(\text{PO}_4)_2(\text{P}_2\text{O}_7)$ ($1 \leq x \leq 4$) energy indicates that the presence of an intermediate phase is unlikely, implying a one-phase reaction of the $\text{Na}_x\text{Fe}_3(\text{PO}_4)_2(\text{P}_2\text{O}_7)$ electrode, which is consistent with the *ex situ* results. The various Na-vacancy configurations from calculated intermediate states of $\text{Na}_x\text{Fe}_3(\text{PO}_4)_2(\text{P}_2\text{O}_7)$ reveal that there are preferences in the order of Na extraction. Among four symmetrically different Na sites, shown in Table 4-1, the Na2 site in the five-coordinated polyhedra is extracted first from the structure. Once the Na in Na2 sites is fully extracted, half of the Na in Na1 and half of the Na in Na4 are extracted simultaneously. Finally, half of the Na in Na3 and the remaining Na in Na1 are extracted, leaving half of the Na3 and Na4 sites in $\text{NaFe}_3(\text{PO}_4)_2(\text{P}_2\text{O}_7)$ occupied. The order of Na extraction is illustrated in Table 4-1. Sequential Na extraction from different sites also affects the charge distribution in transition metals. Figure 4-8 illustrates the number of spins integrated around Fe in the structure, from which the oxidation state of the transition metal can be estimated considering the spin configuration of the Fe orbitals in octahedral coordination. As shown in Figure 4-8a, there are three different Fe sites in the structure. Initially, all of the Fe shows an identical

magnetic moment corresponding to Fe^{2+} in Figure 4-8b. However, as Na is extracted from the Na2 site, the spin moment of the Fe1 site increases, indicating oxidation to Fe^{3+} , shown in Figure 4-8c. It is noteworthy that the Fe1 site is the nearest-neighbor site of Na2. Upon further desodiation, Figure 4-8d, Fe2 oxidizes from +2 to +3. We attribute the oxidation of Fe2 prior to Fe3 to effective electrostatic interactions among Fe ions. As the Fe3 octahedron shares an edge with the Fe1 octahedron, whose oxidation state is already +3, further oxidation to Fe^{3+} in Fe3 will be less favorable due to electrostatic repulsion. Instead, Fe in Fe2, which does not share an edge with Fe1, will be oxidized. Finally, Fe in the Fe3 site oxidizes to +3, as shown in Figure 4-8e.

The unusual *c*-lattice evolution at $1 \leq x \leq 2$ in $\text{Na}_x\text{Fe}_3(\text{PO}_4)_2(\text{P}_2\text{O}_7)$ can also be clearly detected at an atomic scale from first principles calculations. Figure 4-9(a-b) compares the calculated schematic structure of $\text{Na}_2\text{Fe}_3(\text{PO}_4)_2(\text{P}_2\text{O}_7)$ and $\text{NaFe}_3(\text{PO}_4)_2(\text{P}_2\text{O}_7)$. The mother framework of $\text{Na}_x\text{Fe}_3(\text{PO}_4)_2(\text{P}_2\text{O}_7)$ ($x = 2, 1$) is not significantly altered with the Na ion extraction. However, distinct structural change is locally observed in $\text{NaFe}_3(\text{PO}_4)_2(\text{P}_2\text{O}_7)$. The amplified FeO_6 and PO_4 in Figure 4-9b show the significant distortion of PO_4 (P4) in the P_2O_7 dimer. It should be noted that this distortion was not observed in $\text{Na}_4\text{Fe}_3(\text{PO}_4)_2(\text{P}_2\text{O}_7)$, $\text{Na}_3\text{Fe}_3(\text{PO}_4)_2(\text{P}_2\text{O}_7)$, and $\text{Na}_2\text{Fe}_3(\text{PO}_4)_2(\text{P}_2\text{O}_7)$. The distortion of P_2O_7 also affects the Fe3 – Fe1 connection, which transforms from edge sharing to corner sharing when nearby Na4 sites are occupied. We believe that this structural change stems from $\text{Fe}^{3+} - \text{Fe}^{3+}$ repulsion in the $[\text{Fe}_3\text{P}_2\text{O}_{13}]_\infty$

chain. As described earlier, Fe in the Fe3 site is oxidized to +3 when x finally reaches 1. Therefore, at the $\text{NaFe}_3(\text{PO}_4)_2(\text{P}_2\text{O}_7)$ composition, Fe3 – Fe1 repulsion leads to corner sharing instead of edge sharing. The distance between Fe1 and Fe3 in $\text{Na}_2\text{Fe}_3(\text{PO}_4)_2(\text{P}_2\text{O}_7)$ is 3.3 Å; Fe1 is in Fe^{3+} and Fe3 is in Fe^{2+} . However, the extraction of Na from $\text{Na}_2\text{Fe}_3(\text{PO}_4)_2(\text{P}_2\text{O}_7)$ involving the oxidation of Fe in Fe3 sites does not lead to further reduction of the Fe1 – Fe3 distance. Instead, the P_2O_7 dimer distorts such that the stronger electrostatic repulsion between the Fe^{3+} in Fe1, and Fe3 is effectively buffered. This distortion shifts the Fe1 site in the a direction, thus significantly reducing the c lattice parameter.

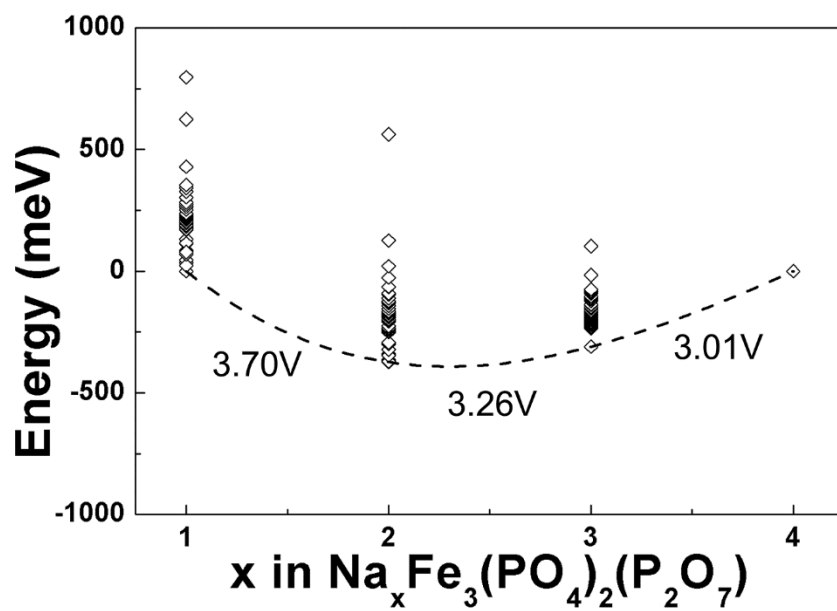
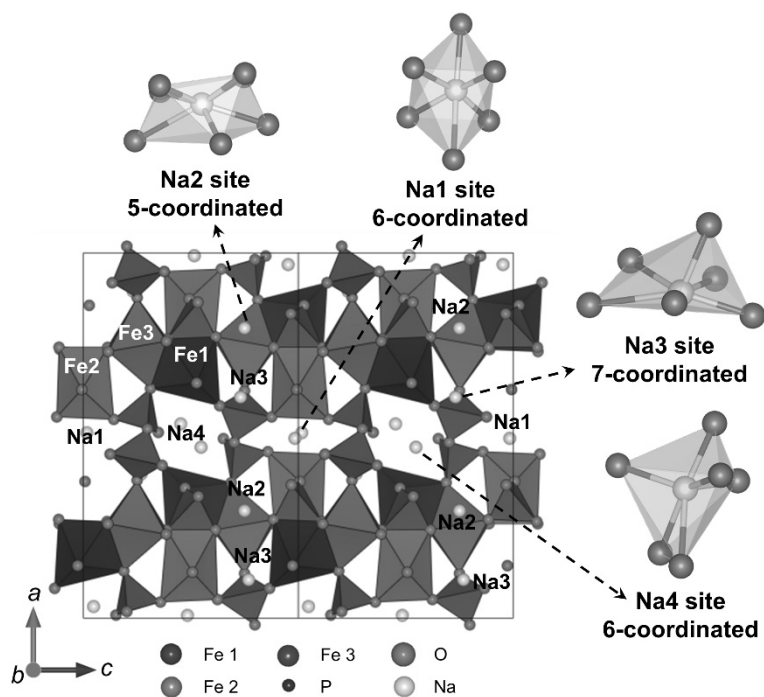


Figure 4-7. DFT formation energies of $\text{Na}_x\text{Fe}_3(\text{PO}_4)_2(\text{P}_2\text{O}_7)$ at various configurations of x .



Composition	Space group	Na1 site	Na2 site	Na3 site	Na4 site
$\text{Na}_4\text{Fe}_3(\text{PO}_4)_2(\text{P}_2\text{O}_7)$	$Pn2_1a$	1.0	1.0	1.0	1.0
$\text{Na}_3\text{Fe}_3(\text{PO}_4)_2(\text{P}_2\text{O}_7)$	$Pn2_1a$	1.0	0	1.0	1.0
$\text{Na}_2\text{Fe}_3(\text{PO}_4)_2(\text{P}_2\text{O}_7)$	$Pn2_1a$	0.5	0	1.0	0.5
$\text{NaFe}_3(\text{PO}_4)_2(\text{P}_2\text{O}_7)$	$Pn2_1a$	0	0	0.5	0.5

Table 4-1. Schematic representations of $\text{Na}_4\text{Fe}_3(\text{PO}_4)_2(\text{P}_2\text{O}_7)$ and order of sodium extraction from the structure of $\text{Na}_x\text{Fe}_3(\text{PO}_4)_2(\text{P}_2\text{O}_7)$ ($1 \leq x \leq 4$).

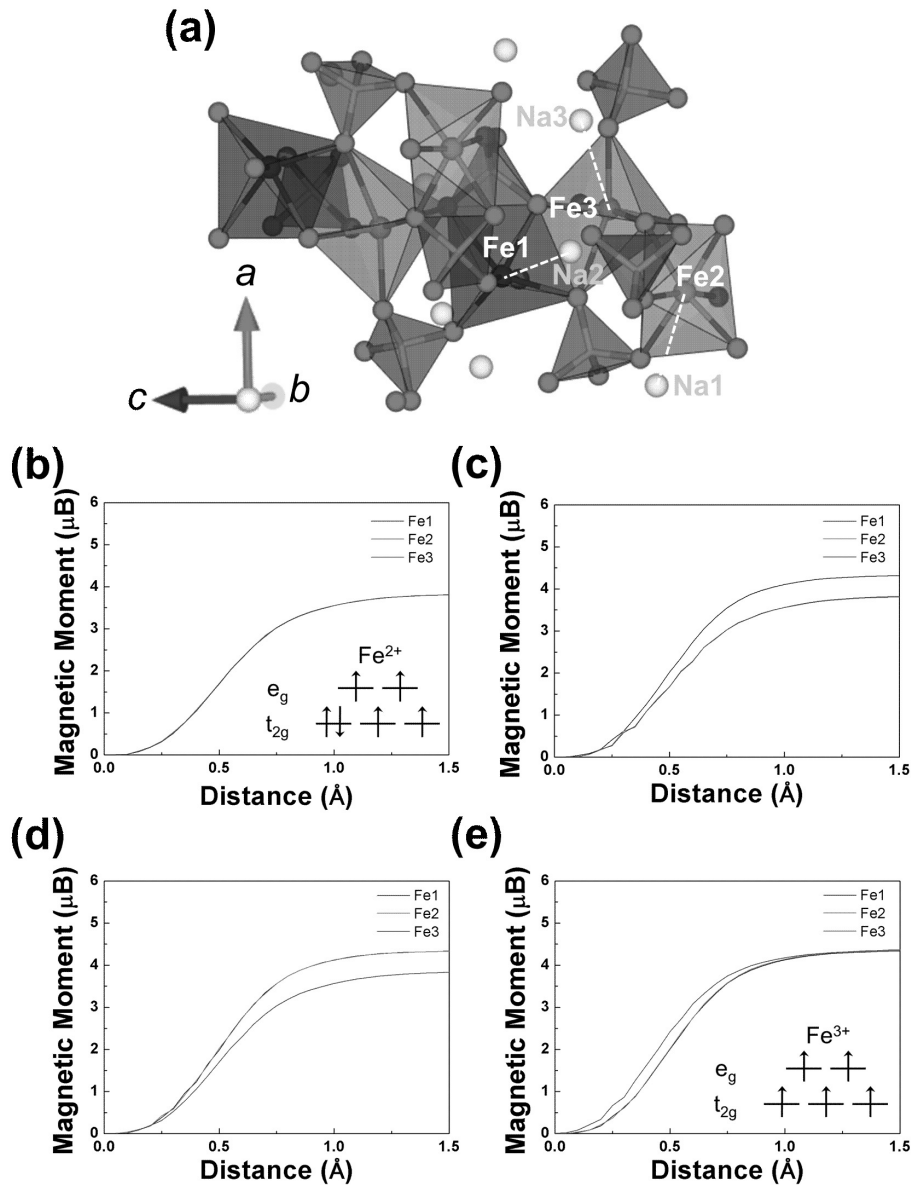


Figure 4-8. (a) Local structure schematics of $\text{Na}_x\text{Fe}_3(\text{PO}_4)_2(\text{P}_2\text{O}_7)$ around Fe sites and integrated spin as a function of integration radius around Fe in $\text{Na}_x\text{Fe}_3(\text{PO}_4)_2(\text{P}_2\text{O}_7)$ ((b) $x = 4$, (c) $x = 3$, (d) $x = 2$, and (e) $x = 1$).

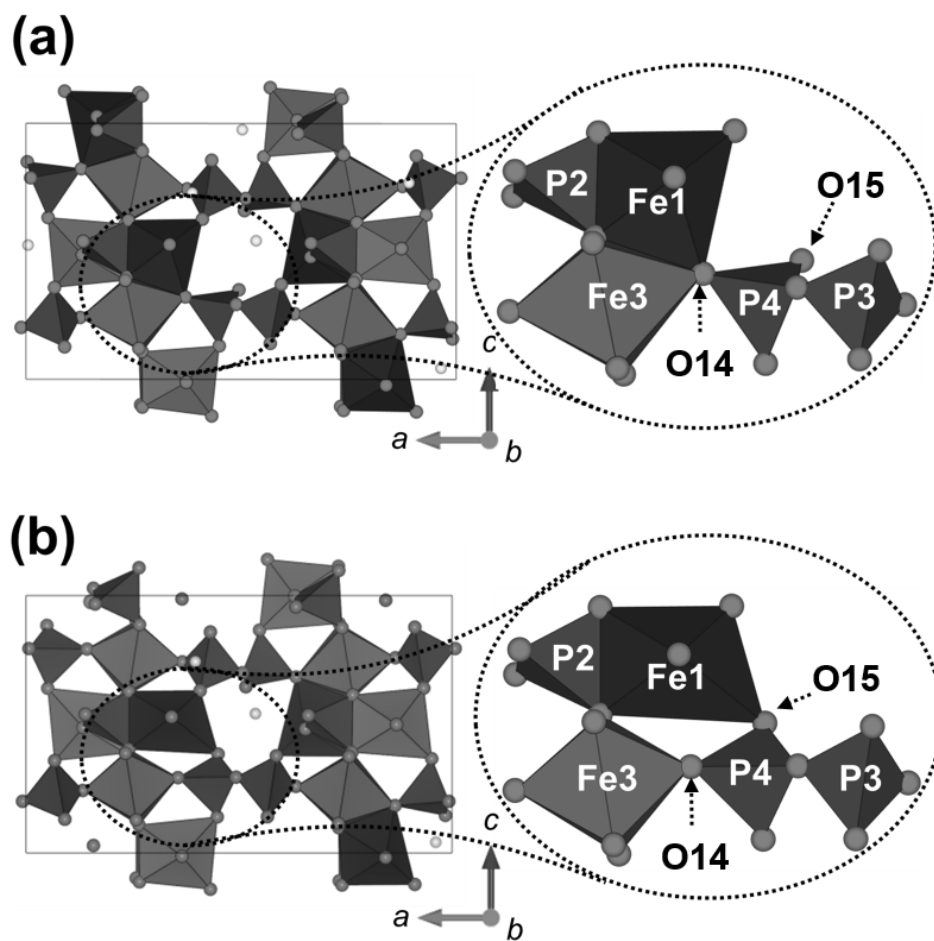
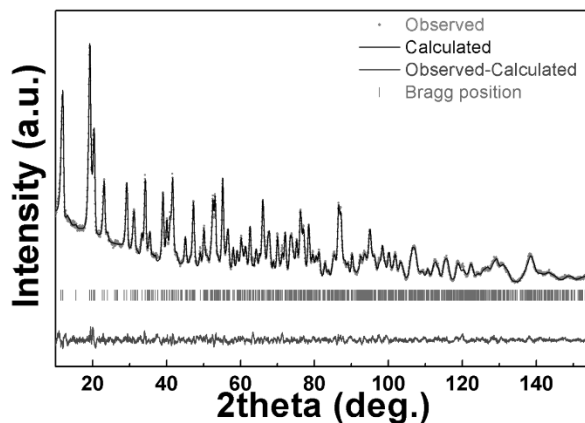


Figure 4-9. Structure schematics of $\text{Na}_x\text{Fe}_3(\text{PO}_4)_2(\text{P}_2\text{O}_7)$ at (a) $x = 2$ and (b) $x = 1$ from first principles calculations.

This theoretical explanation was further confirmed by ND refinements of $\text{NaFe}_3(\text{PO}_4)_2(\text{P}_2\text{O}_7)$. Figure 4-10 presents the ND Rietveld refinement of $\text{NaFe}_3(\text{PO}_4)_2(\text{P}_2\text{O}_7)$ and the corresponding local structure around the Fe1 and Fe3 sites. Detailed structural information from the ND patterns is presented in Table 4-2 and 3-3. It is interesting to note that the significant P_2O_7 distortion in $\text{NaFe}_3(\text{PO}_4)_2(\text{P}_2\text{O}_7)$ leads to a shift from edge sharing to corner sharing of FeO_6 polyhedra between the Fe1 and Fe3 sites, in striking agreement with our first principles calculation. We further note that the local distortion in $\text{NaFe}_3(\text{PO}_4)_2(\text{P}_2\text{O}_7)$ can affect Na diffusion. Since the local distortion involves a shift of Fe in Fe1 and the P_2O_7 dimer that narrows Na diffusion tunnels, as indicated with the arrow in Figure 4-10b, the mobility of Na is potentially reduced at this composition of $x \sim 1$. As this distortion is mainly observed at $1 \leq x \leq 2$ in $\text{Na}_x\text{Fe}_3(\text{PO}_4)_2(\text{P}_2\text{O}_7)$ (Table in Figure 4-10b), it is believed to reduce the Na de/intercalation kinetics particularly in this region, and therefore to increase the polarization. Based on these results, we speculate that the incomplete utilization of Na ($\sim 82\%$ of theoretical capacity in Figure 4-1b) can be attributed to a large polarization developing at the last stage of charging, despite its apparent high rate capability as reflected in the negligible capacity reduction from $C/20$ to $C/5$.

(a)



(b)

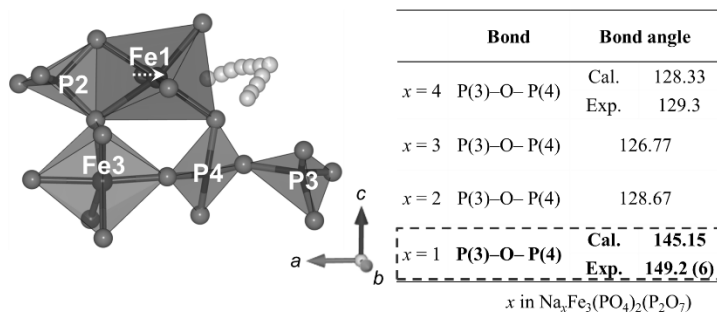


Figure 4-10. (a) Rietveld refinement of $\text{NaFe}_3(\text{PO}_4)_2(\text{P}_2\text{O}_7)$ using ND. (b) Local structure schematics around Fe1 and P(3) – O – P(4) bond angle comparison table as a function of Na content (x) in $\text{Na}_x\text{Fe}_3(\text{PO}_4)_2(\text{P}_2\text{O}_7)$ from ND analysis.

Table 4-2. Detailed structural information of NaFe₃(PO₄)₂(P₂O₇) analyzed by Rietveld refinement of the ND pattern.

Formula	NaFe ₃ (PO ₄) ₂ (P ₂ O ₇)
Crystal system	Orthorhombic
Space group	Pn2 ₁ a (No. 33)
Lattice parameters	
<i>a</i> (Å)	17.6613 (9)
<i>b</i> (Å)	6.3966 (4)
<i>c</i> (Å)	10.7012 (7)
Unitcell volume (Å ³)	1208.948 (1)
Formula weight	531.42104
Source	Neutron
Temperature (K)	300K
Wave length (Å)	1.834333
2θ range	0 – 180°
Number of data points	3200
Number of reflections	905
R _p (%)	1.91
R ₁ (%)	1.82
R _F (%)	0.999
R _{wp} (%)	2.42
χ ²	3.86

Atom	<i>x</i>	<i>y</i>	<i>z</i>	B _{iso}	Occupancy
Fe1	0.3587 (5)	0.113 (4)	0.496 (1)	0.93 (9)	1.00
Fe2	0.1516 (4)	0.603 (4)	0.500 (1)	0.93 (9)	1.00
Fe3	0.2446 (7)	0.350 (4)	0.7652 (9)	0.93 (9)	1.00
P1	0.3064 (11)	0.595 (5)	0.496 (2)	0.6 (1)	1.00
P2	0.1997 (9)	0.102 (5)	0.493 (2)	0.6 (1)	1.00
P3	0.5733 (11)	0.472 (5)	0.742 (2)	0.6 (1)	1.00
P4	0.4279 (10)	0.248 (4)	0.752 (2)	0.6 (1)	1.00
Na3	0.409 (4)	0.468 (10)	0.312 (6)	1.0 (3)	0.13 (1)
Na4	0.485 (1)	0.794 (3)	0.534 (1)	1.0 (3)	0.87 (1)
O1	0.2387 (8)	0.5743 (5)	0.611 (2)	0.22 (5)	1.00
O2	0.3496 (10)	0.410 (4)	0.490 (2)	0.22 (5)	1.00
O3	0.3469 (9)	0.808 (5)	0.533 (1)	0.22 (5)	1.00
O4	0.2517 (8)	0.605 (4)	0.384 (2)	0.22 (5)	1.00
O5	0.2551 (9)	0.156 (5)	0.608 (2)	0.22 (5)	1.00
O6	0.1428 (10)	-0.053 (4)	0.520 (1)	0.22 (5)	1.00
O7	0.2518 (8)	0.078 (5)	0.395 (2)	0.22 (5)	1.00
O8	0.1427 (8)	0.327 (4)	0.462 (1)	0.22 (5)	1.00
O9	0.5107 (8)	0.325 (4)	0.7194 (10)	0.22 (5)	1.00
O10	0.5845 (7)	0.624 (5)	0.859 (1)	0.22 (5)	1.00
O11	0.6395 (8)	0.314 (4)	0.768 (1)	0.22 (5)	1.00
O12	0.5748 (8)	0.653 (4)	0.661 (1)	0.22 (5)	1.00
O13	0.4251 (9)	0.162 (4)	0.871 (1)	0.22 (5)	1.00
O14	0.3627 (7)	0.374 (4)	0.766 (2)	0.22 (5)	1.00
O15	0.4440 (7)	0.160 (4)	0.605 (1)	0.22 (5)	1.00

Table 4-3. Bond valence parameters of each atom in $\text{Na}_x\text{Fe}_3(\text{PO}_4)_2(\text{P}_2\text{O}_7)$ ($x = 1, 4$).

Atomic site	Coordination		Average Distance		Expected values	Bond valence	
	DFT	Exp.	DFT	Exp.		DFT	Exp.
Fe1	6.00	6.00	2.06 (2)	2.05 (1)	3.0	2.7 (1)	2.9 (1)
Fe2	6.00	6.00	2.0602 (3)	2.01 (1)	3.0	2.83 (5)	3.3 (1)
Fe3	6.00	6.00	2.06 (3)	2.05 (1)	3.0	2.8 (1)	2.78 (8)
P1	4.00	4.00	1.5547 (4)	1.56 (2)	5.0	4.746 (2)	4.8 (2)
P2	4.00	4.00	1.5564 (3)	1.56 (2)	5.0	4.73 (1)	5.1 (2)
P3	4.00	4.00	1.549 (4)	1.52 (2)	5.0	4.82 (6)	5.2 (2)
P4	4.00	4.00	1.551 (5)	1.52 (1)	5.0	4.82 (4)	5.5 (2)
Na3	4.00	6.00	2.4737	2.38 (1)	1.0	1.034	1.07 (4)
Na4	5.00	6.00	2.4842	2.427 (8)	1.0	0.991	1.09 (3)
O1	3.00	3.00	1.97 (2)	1.95 (2)	-2.0	-1.82 (3)	-1.67 (7)
O2	2.13	3.00	2.05 (1)	1.84 (2)	-2.0	-1.86 (3)	-2.4 (2)
O3	2.87	2.50	1.9 (1)	2.01 (2)	-2.0	-1.89 (3)	-1.8 (1)
O4	3.00	3.00	1.93 (1)	1.91 (1)	-2.0	-1.90 (3)	-2.1 (1)
O5	3.00	3.00	1.89 (1)	1.97 (1)	-2.0	-1.97 (6)	-1.72 (8)
O6	2.00	2.50	1.9 (2)	1.83 (2)	-2.0	-1.84 (4)	-1.9 (1)
O7	3.00	2.50	1.9 (1)	1.87 (1)	-2.0	-1.72 (7)	-2.6 (1)
O8	2.00	2.00	1.746 (8)	1.80 (3)	-2.0	-1.86 (1)	-1.5 (1)
O9	3.00	2.50	1.8 (2)	2.12 (1)	-2.0	-2.10 (4)	-2.6 (1)
O10	2.00	2.50	1.9 (2)	1.76 (2)	-2.0	-1.95 (1)	-1.7 (1)
O11	2.13	2.50	1.9 (1)	2.00 (1)	-2.0	-1.86 (4)	-1.8 (1)
O12	3.00	3.00	1.9 (2)	1.96 (1)	-2.0	-2.1 (1)	-2.3 (2)
O13	2.00	2.00	1.735 (7)	1.68 (2)	-2.0	-1.90 (1)	-2.4 (1)
O14	2.00	3.00	1.97 (4)	1.75 (2)	-2.0	-1.89 (8)	-2.1 (1)
O15	3.74	3.00	2.04 (4)	2.08 (1)	-2.0	-1.84 (3)	-1.92 (7)

Atomic site	Coordination		Average Distance		Expected values	Bond valence	
	DFT	Exp.	DFT	Exp.		DFT	Exp.
Fe1	6.00	6.00	2.169	2.138 (9)	2.0	1.913	2.09 (6)
Fe2	6.00	6.00	2.168	2.156 (9)	2.0	1.879	1.97 (6)
Fe3	5.00	5.00	2.114	2.10 (1)	2.0	1.812	1.86 (6)
P1	4.00	4.00	1.557	1.56 (1)	5.0	4.713	4.7 (2)
P2	4.00	4.00	1.560	1.54 (1)	5.0	4.669	5.1 (2)
P3	4.00	4.00	1.562	1.57 (1)	5.0	4.680	4.6 (2)
P4	4.00	4.00	1.564	1.51 (1)	5.0	4.673	5.6 (2)
Na1	6.00	6.00	2.412	2.37 (1)	1.0	1.186	1.37 (5)
Na2	7.00	7.00	2.532	2.51 (1)	1.0	1.000	1.07 (4)
Na3	5.00	5.00	2.451	2.44 (1)	1.0	0.933	1.00 (4)
Na4	6.00	6.00	2.537	2.51 (1)	1.0	0.882	0.94 (3)
O1	4.00	4.00	2.123	2.10 (1)	-2.0	1.897	2.00 (9)
O2	4.00	4.00	2.217	2.17 (1)	-2.0	1.874	1.75 (9)
O3	4.00	4.00	2.124	2.16 (2)	-2.0	1.947	2.0 (1)
O4	4.00	4.00	2.069	2.04 (1)	-2.0	1.987	2.09 (8)
O5	4.00	4.00	2.116	2.10 (1)	-2.0	1.915	1.81 (7)
O6	4.00	4.00	2.224	2.23 (2)	-2.0	1.816	1.8 (1)
O7	4.00	4.00	2.121	2.09 (1)	-2.0	1.874	2.09 (9)
O8	4.00	4.00	2.159	2.13 (2)	-2.0	1.891	2.4 (2)
O9	3.00	3.00	1.983	1.94 (2)	-2.0	1.902	2.00 (9)
O10	4.00	4.00	2.159	2.10 (1)	-2.0	1.886	1.81 (7)
O11	3.00	3.00	2.029	2.05 (1)	-2.0	1.788	1.79 (9)
O12	4.00	4.00	2.121	2.06 (1)	-2.0	2.002	2.2 (1)
O13	4.00	4.00	2.114	2.10 (1)	-2.0	1.959	2.5 (1)
O14	3.00	3.00	2.071	2.04 (1)	-2.0	1.745	2.22 (9)
O15	4.00	4.00	2.199	2.19 (1)	-2.0	1.858	1.83 (8)

The desodiation mechanism was further analyzed by XANES to monitor the redox reaction. Figure 4-11a clearly shows that the XANES spectrum shifts to the right during the first charging, indicating oxidation of iron from Fe^{2+} to Fe^{3+} . An $\text{Na}_4\text{Fe}_3(\text{PO}_4)_2(\text{P}_2\text{O}_7)$ powder sample was used as an Fe^{2+} reference, since its oxidation state was previously identified using Fe Mössbauer analysis.¹⁰ The XANES spectrum shifts back to lower valence states with progress of the discharge reaction. Finally, iron recovers its original oxidation state, Fe^{2+} , at the discharge state of 1.7 V, as shown in Figure 4-11b. The tendency of XANES spectra during the second cycle was almost identical to that of the initial charge state (see Figure 4-12). The XANES spectra of the as-prepared state and of the end of the charge/discharge states are compared in Figure 4-11c. The iron oxidation state of the as-prepared and cycled electrode was consistent with the Fe^{2+} reference material, and the oxidation state of fully charged samples corresponded to Fe^{3+} . Supplementary XANES spectra from chemically prepared samples indicated the same trend, and are provided in Figure 4-13.

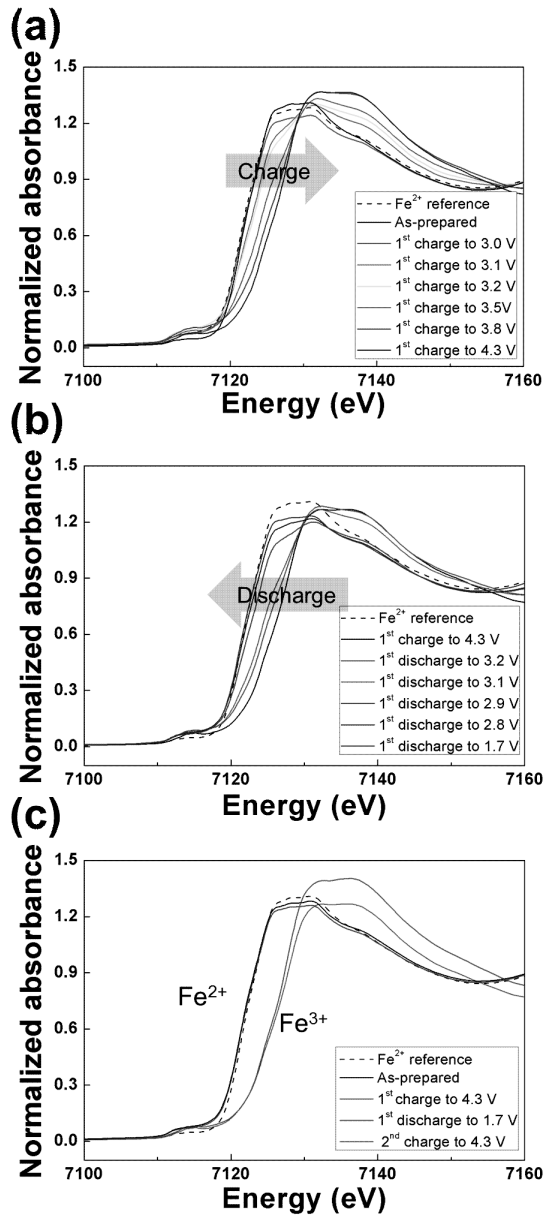


Figure 4-11. XANES spectra during first (a) charge and (b) discharge. XANES spectra of the as-prepared state and of the end of charge and end of discharge states are shown in (c).

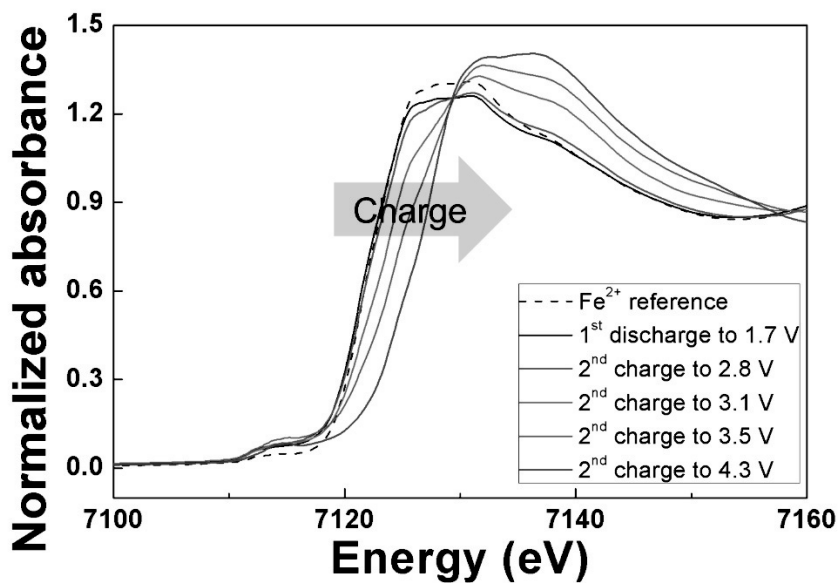


Figure 4-12. X-ray absorption near-edge structure (XANES) spectra of the $\text{Na}_x\text{Fe}_3(\text{PO}_4)_2(\text{P}_2\text{O}_7)$ electrode during the second charge.

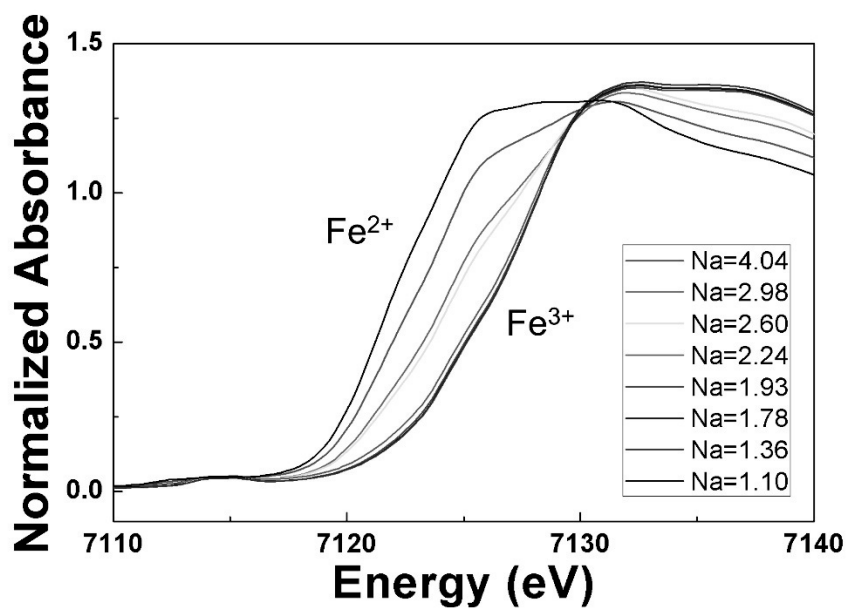


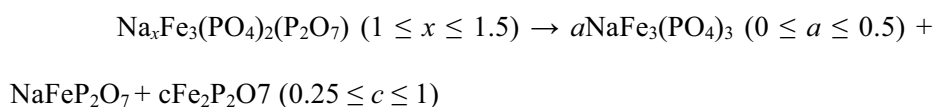
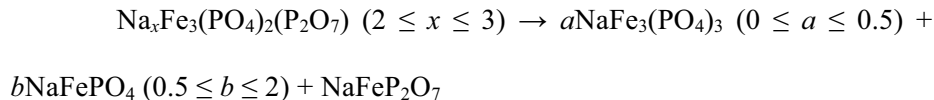
Figure 4-13. XANES spectra of chemically prepared $\text{Na}_x\text{Fe}_3(\text{PO}_4)_2(\text{P}_2\text{O}_7)$ ($1 \leq x \leq 4$) samples.

The nature of the de/intercalation process of $\text{Na}_4\text{Fe}_3(\text{PO}_4)_2(\text{P}_2\text{O}_7)$ was additionally confirmed from electrochemical PITT measurements, as shown in Figure 4-14(a,b). The PITT experiment was carried out using a voltage step of 5 mV and a cut-off current corresponding to the C/50 rate. “Cottrel-type” curves that represent the one-phase reaction were observed throughout the range of the charge and discharge steps.²³ This result is consistent with the *ex situ* XRD and first principles calculations.

Finally, the safety of the $\text{Na}_4\text{Fe}_3(\text{PO}_4)_2(\text{P}_2\text{O}_7)$ electrode at high temperature was examined by evaluating the thermal stability of partially desodiated phases. A series of samples with different SOC was prepared through chemical desodiation, and the stability of the samples was investigated using DSC and *in situ* high-temperature XRD analyses. Figure 4-15 shows the DSC curves of partially charged samples, which illustrate that all of the partially charged samples were stable up to 500°C. Exothermic peaks began to appear only above 500 °C for each sample, and the intensity of the exothermic peaks increased with the SOC. *In situ* high temperature XRD, Figure 4-16(a–d), also confirmed the superior thermal stability of $\text{Na}_x\text{Fe}_3(\text{PO}_4)_2(\text{P}_2\text{O}_7)$ irrespective of the SOC. The desodiated phases followed various decomposition routes depending on the remaining Na composition. For example, the slightly desodiated sample $\text{Na}_{3.2}\text{Fe}_3(\text{PO}_4)_2(\text{P}_2\text{O}_7)$ decomposed mainly into Na-rich compounds, such as $\text{Na}_3\text{Fe}_2(\text{PO}_4)_3$ and NaFePO_4 , starting at 550 to 650 °C. As the Na composition in the phase decreased, Na-poor phases such as $\text{NaFe}_3(\text{PO}_4)_3$, NaFeP_2O_7 , and

$\text{Fe}_2\text{P}_2\text{O}_7$ were preferentially evolved as decomposition products. The fully charged sample, $\text{NaFe}_3(\text{PO}_4)_2(\text{P}_2\text{O}_7)$, yielded $\text{Fe}_2\text{P}_2\text{O}_7$ and NaFeP_2O_7 at the same temperature.¹⁰

Figure 4-17 summarizes the decomposed phases of $\text{Na}_x\text{Fe}_3(\text{PO}_4)_2(\text{P}_2\text{O}_7)$ ($1 < x < 4$) upon heating. Solid solution of $\text{Na}_x\text{Fe}_3(\text{PO}_4)_2(\text{P}_2\text{O}_7)$ ($1 < x < 4$) was maintained up to 530 °C at all SOC. However, at temperatures higher than 530 °C, the phases began to decompose, yielding a few different products depending on the remaining Na content in the phases. Although it is difficult to precisely describe the decomposition reaction as a chemical formula due to the complex feature involving many phases, the decomposition process of $\text{Na}_x\text{Fe}_3(\text{PO}_4)_2(\text{P}_2\text{O}_7)$ ($x \leq 3$) can be estimated as follows.



The high stability at all SOCs is notable and is comparable to that of the safest polyanion cathodes for Na rechargeable batteries,^{9,24,25} illustrating the inherently safe characteristics of low voltage sodium-based polyanion compounds which have low oxygen chemical potential in desodiated phases.^{19,26} We believe that the outstanding safety characteristics of $\text{Na}_x\text{Fe}_3(\text{PO}_4)_2(\text{P}_2\text{O}_7)$ ($x < 4$) at all SOCs is one of its strongest advantages as a cathode for Na rechargeable battery. However, it should be also noted that for

the safe Na batteries; the safety characteristics of other components, not only the electrodes, should be considered, since the recent report has shown that the use of perchlorate salts in the electrolyte, for example, can cause a danger for explosion.²⁷

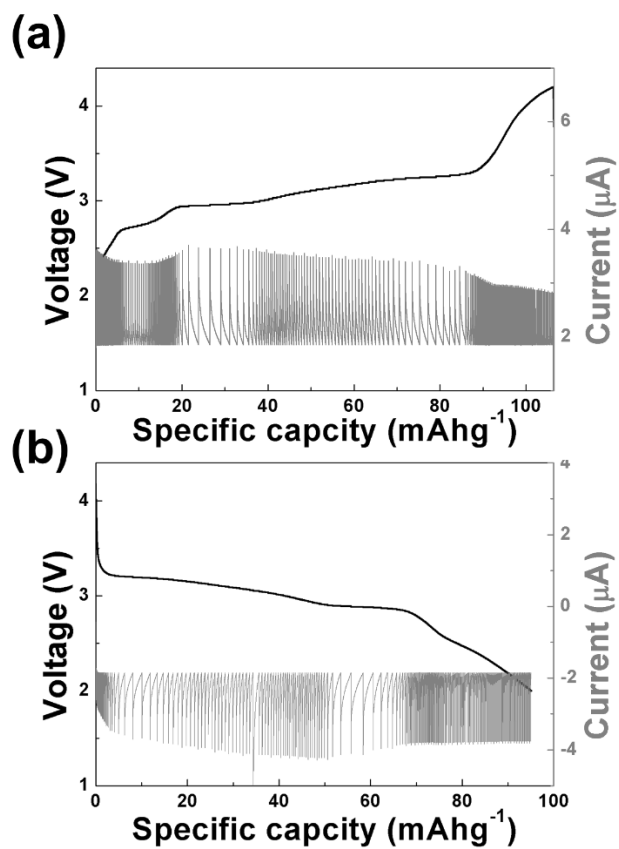


Figure 4-14. PITT measurements of $\text{Na}_4\text{Fe}_3(\text{PO}_4)_2(\text{P}_2\text{O}_7)$ during (a) charging and (b) discharging.

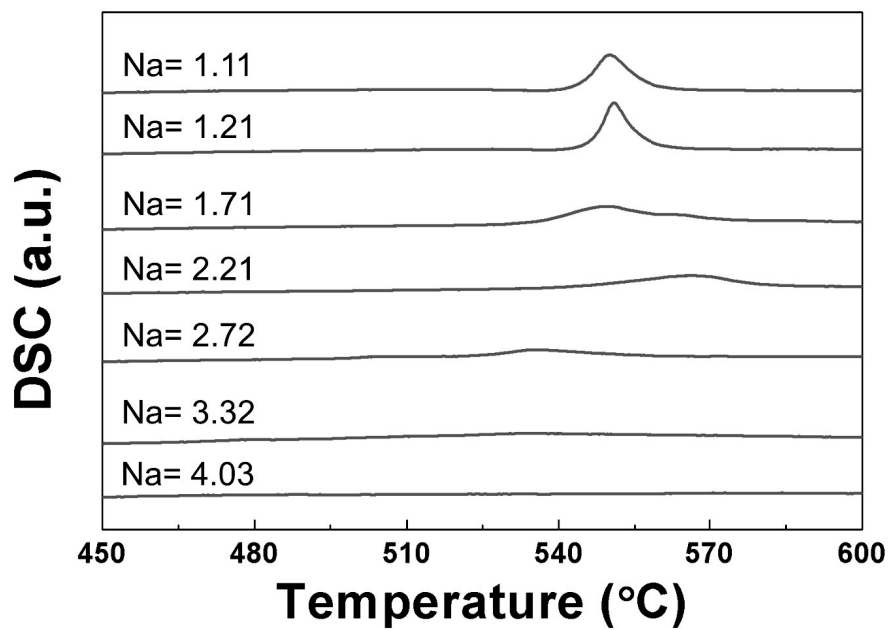
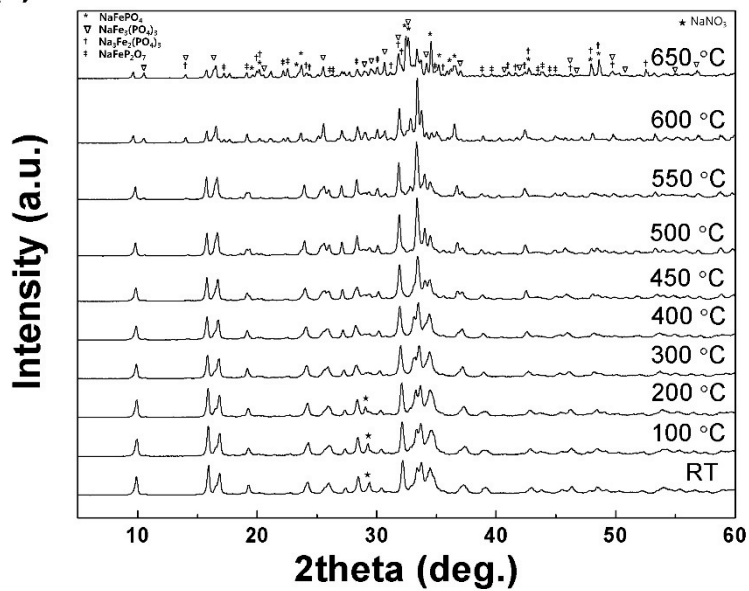
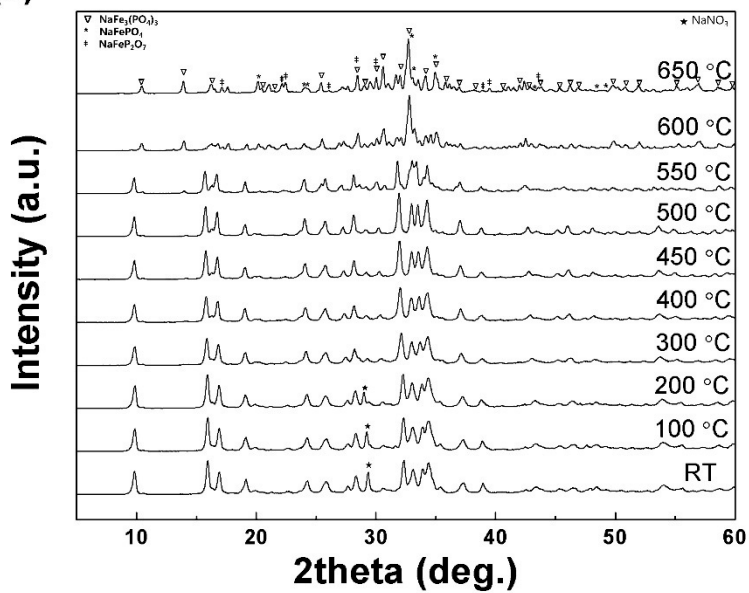


Figure 4-15. Differential scanning calorimetry (DSC) spectra of $\text{Na}_x\text{Fe}_3(\text{PO}_4)_2(\text{P}_2\text{O}_7)$ ($1 \leq x \leq 4$).

(a)



(b)



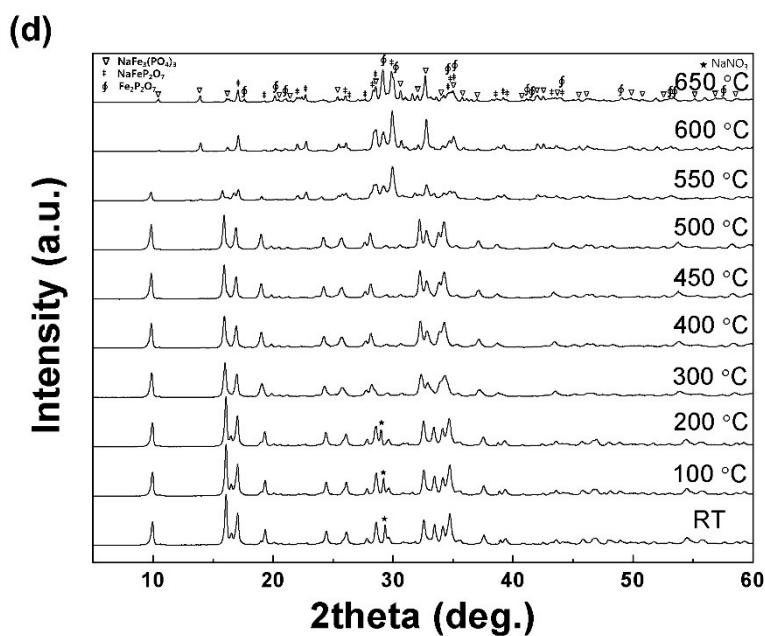
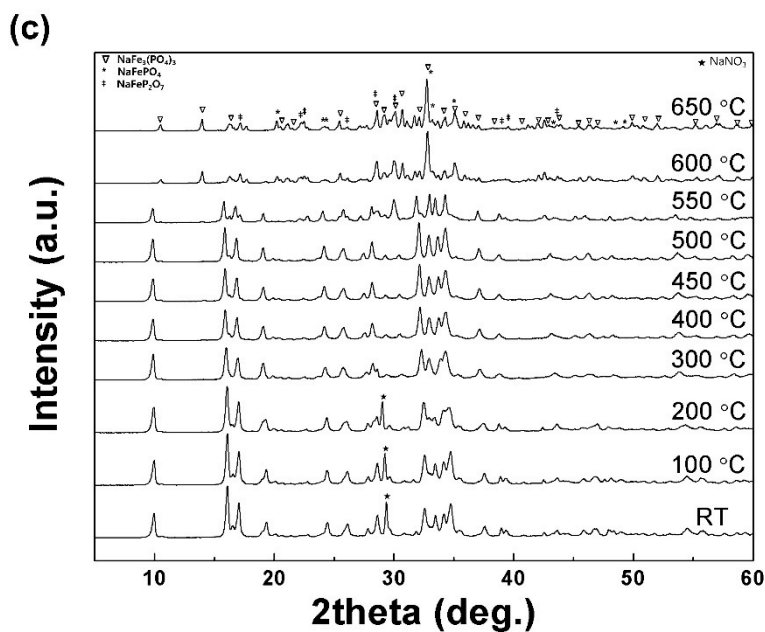


Figure 4-16. *In situ* high-temperature XRD of desodiated powder samples of $\text{Na}_x\text{Fe}_3(\text{PO}_4)_2(\text{P}_2\text{O}_7)$ at (a) $x = 3.2$, (b) $x = 2.72$, (c) $x = 2.21$, and (d) $x = 1.71$.

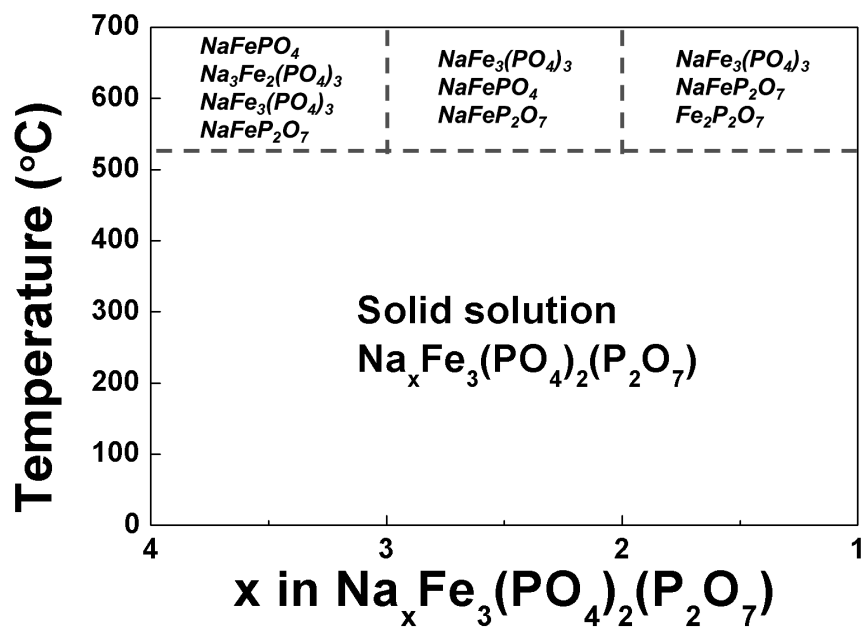


Figure 4-17. Phase diagram of $\text{Na}_x\text{Fe}_3(\text{PO}_4)_2(\text{P}_2\text{O}_7)$ ($1 < x < 4$).

4.4 Conclusion

Detailed structural evolution of $\text{Na}_4\text{Fe}_3(\text{PO}_4)_2(\text{P}_2\text{O}_7)$ during charging and discharging was examined by XRD, ND, XAS, first-principles calculations, and electrochemical measurements. We clarified that the electrochemical reaction of $\text{Na}_4\text{Fe}_3(\text{PO}_4)_2(\text{P}_2\text{O}_7)$ in a Na-ion cell is governed mainly by a one-phase reaction with a reversible structural evolution that includes P_2O_7 distortion. The unusually small volume change observed during cycling is expected to contribute to stable cycle retention. Furthermore, the partially desodiated phases were thermally stable up to 530 °C at all SOCs. With an open framework and one-phase reaction, high voltage (~ 3.2 V vs. Na), low volume change (~ 4 %), and high safety, $\text{Na}_4\text{Fe}_3(\text{PO}_4)_2(\text{P}_2\text{O}_7)$ should be a promising candidate for Na rechargeable battery electrodes.

4.5 References

- (1) J. -M. Tarascon, M. Armand, *Nature* **2001**, *414*, 359–367.
- (2) M. Armand, J. -M. Tarascon, *Nature* **2008**, *451*, 652–657.
- (3) K. Kang, Y. S. Meng, J. Breger, C. P. Grey, G. Ceder, *Science* **2006**, *311*, 977–980.
- (4) P. Moreau, P.; D. Guyomard, J. Gaubicher, F. Boucher. *Chem. Mater.* **2010**, *22*, 4126–4128.
- (5) K. T. Lee, T. N. Ramesh, F. Nan, G. Botton, L. F. Nazar, *Chem. Mater.* **2011**, *23*, 3593-3600.
- (6) B. L. Ellis, W. R. M. Makahnouk, Y. Makimura, K. Toghill, L. F. Nazar, *Nat. Mater.* **2007**, *6*, 749-753.
- (7) P. Barpanda, J. Chotard, N. Recham, C. Delacourt, M. Ati, L. Dupont, M. Armand, J. -M. Tarascon, *Inorg. Chem.* **2010**, *49*, 7401–7413.
- (8) P. Barpanda, T. Ye, S. Nishimura, S. -C. Chung, Y. Yamada, M. Okubo, H. Zhou, A. Yamada, *Electrochem. Commun.* **2012**, *24*, 116–119.
- (9) H. Kim, R. A. Shakoor, C. Park, S. -Y. Lim, J. -S. Kim, Y. -N. Jo, W. Cho, K. Miyasaka, R. Kahraman, Y. Jung, J. -W. Choi, *Adv. Funct. Mater.* **2012**, *23*, 1147–1155.
- (10) H. Kim, I. Park, D. -H. Seo, S. Lee, S. -W. Kim, W. J. Kwon, Y. -U. Park, C. S. Kim, S. Jeon, K. Kang, *J. Am. Chem. Soc.* **2012**, *134*, 10369–10372.

- (11) A. R. Wizansky, P. E. Rauch, F. J. DiSalvo, *J. Solid State. Chem.* **1989**, *81*, 203–207.
- (12) G. Kresse, J. Furthmuller, *Comput. Mater. Sci.* **1996**, *6*, 15.
- (13) J. P. Perdew, K. Burke, M. Ernzerhof, *Phys. Rev. Lett.* **1996**, *77*, 3865.
- (14) V. I. Anisimov, J. Zaanen, O. K. Andersen, *Phys. Rev. B* **1991**, *44*, 943.
- (15) V. I. Anisimov, F. Aryasetiawan, A. I. Lichtenstein, *J. Phys. Condens. Matter* **1997**, *9*, 767.
- (16) G. Hautier, C. C. Fischer, A. Jain, T. Mueller, G. Ceder, *Chem. Mater.* **2010**, *22*, 3762–3767.
- (17) A. Jain, G. Hautier, C. Moore, B. Kang, J. Lee, H. Chen, N. Twu, G. Ceder, *J. Electrochem. Soc.* **2012**, *159*, A622–A633.
- (18) H. Chen, G. Hautier, G. Ceder, *J. Am. Chem. Soc.* **2012**, *134*, 19619–19627.
- (19) G. Hautier, A. Jain, T. Mueller, C. Moore, S. P. Ong, G. Ceder, *Chem. Mater.* **2013**, *25*, 2064–2074.
- (20) P. P. Ewald, *Annalen der Physik.*, **1921**, *369*, 253-287.
- (21) A. Van der Ven, M. K. Aydinol, G. Ceder, *Phy. Rev. B* **1998**, *58*, 2975–2987.
- (22) R. Malik, F. Zhou, G. Ceder, *Nat. Mater.* **2011**, *10*, 587–590.
- (23) N. Meethong, H. –Y. Huang, S. A. Speakman, W. C. Carter, Y. –M. Chiang, *Adv. Funct. Mater.* **2007**, *17*, 1115–1123.

- (24) S. -W. Kim, J. Kim, H. Gwon, K. Kang, *J. Electrochem. Soc.* **2009**, *156*, A635–A638.
- (25) P. Barpanda, J. -M. Chotard, N. Recham, C. Delacourt, M. Ati, L. Dupont, M. Armand, J. -M. Tarascon, *Inorg. Chem.* **2010**, *49*, 7401–7413.
- (26) S. P. Ong, A. Jain, G. Hautier, B. Kang, G. Ceder, *Electrochem. Commun.* **2010**, *12*, 427–430.
- (27) A. Ponrouch, E. Marchante, M. Courty, J. -M. Tarascon, M. R. Palacin, *Energy Environ. Sci.* **2012**, *5*, 8572–8583.

Chapter 5. Amorphous cobalt phyllosilicate with layered crystalline motifs as water oxidation catalyst

(The content of this chapter is now submitted to a scientific journal.)

5.1 Introduction

Electrochemical water splitting has been regarded as a promising and eco-friendly approach to produce hydrogen, a clean fuel, by avoiding a dependency on fossil fuels.¹⁻⁷ The oxygen evolution reaction (OER) is the bottleneck of the overall water-splitting reaction because of the sluggish multi-electron reaction and O–O bond formation.⁸⁻¹¹ Precious-metal-based catalysts such as RuO₂ and IrO₂ have been widely studied as prime catalysts for the OER because of their superior catalytic activity.¹²⁻¹⁶ However, the rarity and high cost of precious metals prohibit the large-scale commercialization of these catalysts; therefore, tremendous research efforts have been directed toward the search for efficient and inexpensive OER catalysts based on non-precious transition metals.¹⁷⁻³⁴ Nocera and co-workers reported that Co- and Ni-based materials such as amorphous cobalt phosphates and nickel borates are capable of delivering comparable performance to that of conventional catalysts even in neutral and weak alkaline electrolytes.^{9,26} In addition, more recent studies have revealed that layered metal (oxy)hydroxides can be effective electrocatalysts, among

which layered double hydroxides containing Ni, Fe, or Co can exhibit remarkably high OER catalytic activity that can surpass that of precious-metal-based catalysts.³⁵⁻³⁹

Unveiling the origin of the high catalytic activity in these transition-metal-based OER catalysts would provide insight for the rational design of new efficient catalysts. In this respect, an atomistic level of understanding of the activity of OER catalysts is necessary with consideration of the local environment of the redox-active transition metal element. Recent studies have proposed that the coordination number of transition metals (MO_x), their local distortion, and how they are connected (*i.e.*, edge-shared or corner-shared) can sensitively affect the catalytic activity.^{23,40-45} Furthermore, neighboring redox-inert elements can alter the redox activity of catalysts; for example, anions such as phosphate and borate facilitate proton-coupled electron transfer,⁴⁶⁻⁴⁸ and capping anion species affect the domain size of electrodeposited amorphous catalysts,^{40,41,49,50} significantly altering the catalysis. In addition, in our recent study, it was demonstrated that the phosphate or pyrophosphate group in catalysts such as $\text{Mn}_3(\text{PO}_4)_2 \cdot 3\text{H}_2\text{O}$, LiMnP_2O_7 , and $\text{Na}_2\text{CoP}_2\text{O}_7$ can enhance the structural flexibility, thereby stabilizing the transition metal and promoting the OER activity,^{23,51,52} which is indicative of the importance of the relationship between the structure and catalytic properties.

Herein, we report an amorphous cobalt phyllosilicate (ACP) with layered crystalline motif as a new efficient OER catalyst. The ACP catalyst can be

prepared using a simple, fast, and low-cost precipitation method at room temperature and exhibits one of the highest OER activities among known Co-based catalysts. In our investigation to elucidate the origin of the catalysis, it is revealed that the OER activity stems from the layered crystalline motif in the ACP, which resembles the structure of CoOOH. Nevertheless, silicate groups present in the interlayer space of the layered crystalline motif significantly modulate the local environment of the active sites and substantially reduce the overall OER overpotential (η) compared with that of conventional layered metal (oxy)hydroxides, as demonstrated by density functional theory (DFT) calculations. This finding suggests that the structural modulation by introducing redox-inert groups in the layer space of metal (oxy)hydroxides can be a viable strategy to tune the catalytic activity and that transition-metal-based phyllosilicates may be new candidates for low-cost and efficient OER catalysts.

5.2 Experimental

Synthesis of ACP and annealed ACP: The ACP was prepared by a simple co-precipitation method by using cobalt chloride (CoCl_2 , Sigma-Aldrich) and sodium metasilicate (Na_2SiO_3 , Sigma-Aldrich). 10.7 mmol Na_2SiO_3 dissolved in 15 ml of deionized water was added to the 8 mmol CoCl_2 dissolved in 75 ml of deionized water aqueous solution under vigorous stirring for 30 min. Then, blue precipitates, ACP, were formed immediately. The ratio of cobalt and silicate precursor were 3:4 to match the stoichiometry of $\text{Co}_3\text{Si}_4\text{O}_{10}(\text{OH})_2$. Hydrothermal process was used to synthesize crystallized ACP. The mentioned above solution prepared for ACP was transferred into a sealed Teflon-lined stainless steel autoclave. The autoclave was annealed at 200 °C for 24 h in air atmosphere. All precipitates were washed by centrifugation with deionized water and ethanol several times and were dried in vacuum oven at 70 °C.

Preparation of CoOOH , Co_3O_4 , CoO and LiCoO_2 : The previously reported method was used for synthesis of CoOOH nanoplates by using air oxidation method.⁶⁶ The solution of 20 mmol $\text{Co}(\text{NO}_3)_2 \cdot 6\text{H}_2\text{O}$ dissolved in 100 ml of deionized water was added to the 100 ml of 5 M NaOH aqueous solution. Then, pink color precipitates were formed and the solution was diluted by pouring to 1800 ml of deionized water. The diluted solution was stirred for 8 h and the solution color changed to brown, meaning that the precipitated $\text{Co}(\text{OH})_2$ (pink) was oxidized to CoOOH (brown). The CoOOH nanoplates was washed by same condition as described above. The Co_3O_4 nanoparticles and CoO purchased

from Sigma Aldrich were directly used for comparison. LiCoO_2 bulk powder were synthesized by a conventional solid-state reaction method. Li_2CO_3 and Co_3O_4 purchased from Sigma Aldrich were used as the raw materials and were mixed by using high-energy ball mill at 400 rpm for 4 h. After mixing, the mixture was heated at 900 °C for 6 h under air atmosphere.

Materials characterizations: X-ray diffractometry (XRD, D8 advance, Bruker) with $\text{Cu K}\alpha$ radiation was used to investigate the crystal structure of prepared samples. The identification of the a-CoSi was carried out by Fourier transform infrared spectroscopy (FT-IR, Hyperion 3000, Bruker). Electron Probe Micro Analyzer (EPMA, JXA-8530F, JEOL) was performed for analysis of element composition. The morphology and the size of clusters were investigated using a high-resolution transmission electron microscope (HR-TEM, JEM-2100F, JEOL). The oxidation state and local environment of Co ion was investigated by X-ray absorption near edge structure (XANES) and X-ray absorption fine structure (EXAFS) analyses. The XANES and EXAFS analysis were performed at the 8C nano X-ray absorption fine structure (XAFS) beamline at the Pohang accelerator laboratory (PAL). All data were collected in the transmittance mode using electron energy of 2.5 GeV and current of 400 mA top-up mode. To examine the local structural properties around the Co atom, the EXAFS data were extracted from full XAFS spectra. The IFEFFIT software under a standard procedure is used to analyze the EXAFS data.⁶⁷⁻⁶⁹ After removing the atomic background via the AUTOBK code (a part of IFEFFIT),

the EXAFS was determined as a function of photoelectron wave number, $k = \sqrt{2m(E - E_0)}/\hbar$, where m is the electron mass, E is the incident X-ray energy, and E_0 is the absorption edge energy.

Electrode preparation: Carbon fiber paper (CFP) was used as substrate of working electrodes. 5 mg of active materials were dispersed in 1 ml of deionized water with 0.1 ml of neutralized Nafion solution and sonicated for 30 min to form homogeneous ink. Then, the ink was uniformly dropped onto CFP with a mass loading of 0.4 mg cm^{-2} . The prepared electrode was placed at 80°C oven for 30 minutes for drying. The Co_3O_4 nanoparticles and CoOOH electrodes were prepared by same condition.

Electrochemical characterization: Electrochemical measurements were performed using a three-electrode beaker cell system with an electrochemical potentiostat (CHI 608C, CH Instruments). In OER test, Hg/HgO electrode filled with 1 M NaOH solution and Pt were used as the reference electrode and the counter electrode, respectively. The potentials of all data were converted to the reversible hydrogen electrode (RHE) scale and overpotential (η) at the current density of 10 mA cm^{-2} was obtained by following equation, $\eta = E_{\text{vs RHE}} - 1.23 \text{ V}$. Ohmic resistance were automatically compensated. Cyclic voltammetry (CV) curves were recorded in 1 M KOH solution at a scan rate of 10 mV s^{-1} . The capacitive background current was removed by averaging of forward scan and backward scan. Tafel plots of samples were obtained by plotting overpotential against logarithm of current density via tafel equation ($\eta = a \log j + b$, η is the

overpotential, j is the current density and a and b are the slope and constant). Long-term stability test was performed at current density of 10 mA cm^{-2} for 24 h. ECSA was obtained from the capacitive charging current of electrochemical double layer. The potential range was 1.00~1.01 V versus RHE and scan rate were 10, 20, 40, 60, 80 and 100 mV sec^{-1} in 1 M KOH electrolyte. The double layer capacitance was determined from the plot of $\Delta j = j_a - j_c$ versus scan rate by following equation:

$$q = C_{dl}E$$

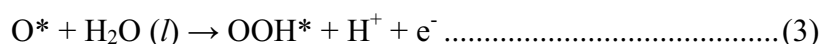
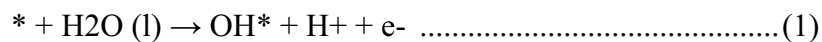
$$j = \frac{\partial q}{\partial t} = C_{dl} \left(\frac{\partial E}{\partial t} \right)$$

Where q is the charge, C_{dl} is the capacitance of electrochemical double layer, E is the potential and j is the current density. All electrochemical measurements were conducted at room temperature.

First principles calculation method: All the calculations presented in this work is performed based on plan-wave based density functional theory (DFT) by the Vienna ab initio simulation package (VASP).⁷⁰ The projector augmented wave (PAW) approach is used to depict the interactions between the valence electrons and the ionic cores.⁷¹ To describe the exchange and correlation, we adopted the generalized gradient approximation plus Hubbard U (GGA+U) method with the revised Perdew–Burke–Ernzerhof exchange-correlation functional (RPBE).^{72,73} The effective Hubbard-U parameter of 3.5 eV is used for a cobalt ion which is good agreement with values reported by other works.⁷⁴⁻⁷⁸ Bulk

structures are calculated within an energy cutoff of 550 eV and appropriate gamma-point centered k -points mesh to ensure that the total energies converged within 0.1 meV per each atom. Surface structure of a-CoSi (or CoOOH) is calculated from slab model consists of three (or four) Co sites per surface and thickness more than 15 Å with vacuum layer of 15 Å to obtain convergence in the adsorption energies and bulk properties of the center layers. Three topmost a-CoSi and CoOOH layers is allowed to relax below the maximum force threshold of 0.05 eV / Å within an energy cutoff of 550 eV and 3 x 3 x 1 gamma-point centered k -points mesh.

Thermodynamics in oxygen evolution reaction: Given the surficial model and active sites, we attempted to estimate the theoretical overpotential of the OER based on DFT calculations. While detailed OER mechanism is complex and not completely established, insight into the thermodynamics of the reaction can be obtained using the acid-base mechanism scheme that has been proposed by Nørskov *et al.*⁷⁹ In this scheme, OER is assumed to consist of four elementary reaction steps as follows (at acidic condition):



(where * denotes a surface site and X* denotes an adsorbed X species)

During the OER with acid-base mechanism, (1) water molecule in liquid phase first adsorb on the surficial active site and dissociate into a H^+ and OH^* . Then (2) OH^* splits into a H^+ and O^* . Then (3) the O^* combines with a water molecule and form an O-O bonding as hydroperoxo intermediate OOH^* and (4) finally evolves O_2 gas.

The free energy differences for OER steps are calculated using following equations:

$$\Delta G_1 = G(OH^*) - G(^*) - \mu_{OH} = E(OH^*) - E(^*) - E(H_2O) + 1/2E(H_2) - eU + \Delta G_{H^+}(pH) + \Delta(ZPE - T\Delta S) \dots\dots\dots (5)$$

$$\Delta G_2 = G(O^*) - G(OH^*) + \mu_H = E(O^*) - E(OH^*) + 1/2E(H_2) - eU + \Delta G_{H^+}(pH) + \Delta(ZPE - T\Delta S) \dots\dots\dots (6)$$

$$\Delta G_3 = G(OOH^*) - G(O^*) - \mu_{OH} = E(OOH^*) - E(O^*) - E(H_2O) + 1/2H_2 - eU + \Delta G_{H^+}(pH) + \Delta(ZPE - T\Delta S) \dots\dots\dots (7)$$

$$\Delta G_4 = 4 \times [1.23 \text{ eV} - eU + \Delta G_{H^+}(pH)] - (\Delta G_1 + \Delta G_2 + \Delta G_3) \quad (8)$$

where U is the potential measured against NHE at standard conditions. The Gibbs free energy change of proton relative to the pH is represented by Nernst equation as $\Delta G_{H^+}(pH) = -k_B T \log(pH)$. The Gibbs free energy differences for each step (ΔG_i) is calculated from DFT energy, zero-point energy(ZPE), and entropy correction according to $\Delta G_i = \Delta E_i + \Delta ZPE_i - T\Delta S_i$. To avoid the calculation including O_2 gas which is difficult to determine within GGA-DFT

scheme, the sum of ΔG_{1-4} is fixed to the 4.92 eV, which is the experimental Gibbs free energy changes in $2\text{H}_2\text{O} > 2\text{H}_2 + \text{O}_2$.

The theoretical overpotential η could be obtained from free energy differences at each step as

$$\eta = \max [\Delta G_1, \Delta G_2, \Delta G_3, \Delta G_4]/e - 1.23 \text{ V} \dots\dots\dots (9)$$

when we calculated all the reaction step energies. Else, overpotential is calculated from

$$\eta > \max [\Delta G_i/e, \{4.92 \text{ V} - \sum(\Delta G_i)/e\}/x] - 1.23 \text{ V} \dots\dots\dots (9-1)$$

where x is the number of the calculated steps. When overpotential for any particular step is higher than 0.6 V, we did not calculate energies for the further steps.

5.3 Results and Discussion

Phyllosilicate mineral is a class of earth abundant layered materials comprised of two different kinds of sheets; one is a polysilicate sheet with corner-shared silicate tetrahedra and the other is the sheet of edge-shared MO_6 (M: Mg, Fe, Co, Ni, and Al) octahedra as schematically shown in Figure 5-1 They are alternatively stacked with shared oxygen atoms, however, it is known that one or two polysilicate sheet can reside between two MO_6 sheets forming an overall layered structure.⁵³⁻⁵⁵ A rapid room temperature synthesis from a co-precipitation method yielded an amorphous phyllosilicate phase after the 30 minutes of vigorous stirring of stoichiometric CoCl_2 and Na_2SiO_3 in aqueous solution as shown in Figure 5-2.

X-ray diffraction (XRD) of ACP (top panel of Figure 5-3) shows a generally broad peak pattern, which represents an amorphous nature, however, hints of the diffraction are observable at around 35° and 60° corresponding to the characteristic peak position of ACP in accordance with Joint Committee on Powder Diffraction Standards (JCPDS, file numbers #21-0872 for $\text{Co}_3\text{Si}_2\text{O}_5(\text{OH})_4$ and #21-0871 for $\text{Co}_3\text{Si}_4\text{O}_{10}(\text{OH})_2$). In order to obtain more insight on the ACP phase, we prepared a hydrothermally annealed ACP treated at 200°C for 24 hours. The XRD of the annealed sample (bottom panel of Figure 5-3) shows a similar pattern to that of the pristine ACP, however, the peaks are notably sharper indicating a higher degree of crystallinity. These peaks well correspond to the XRD patterns of previously reported layered

cobalt phyllosilicates, $\text{Co}_3\text{Si}_2\text{O}_5(\text{OH})_4$ and $\text{Co}_3\text{Si}_4\text{O}_{10}(\text{OH})_2$. Note that both of the phases are structurally similar based on stacking of CoO_6 sheets but the number of the polysilicate sheet residing between two CoO_6 sheets is one and two for $\text{Co}_3\text{Si}_2\text{O}_5(\text{OH})_4$ and $\text{Co}_3\text{Si}_4\text{O}_{10}(\text{OH})_2$, respectively (See inset of Figure 5-1).

Fourier transform infrared (FT-IR) analysis in Figure 5-4 also confirms the characteristic local environment of layered cobalt phyllosilicates. The broad band at $\sim 3400\text{ cm}^{-1}$ and the peak at 1630 cm^{-1} are attributable to the vibration modes from the OH stretching and bending of water molecule.⁵⁶ The peaks at 3629 cm^{-1} and 1010 cm^{-1} correspond to the O-H vibration mode (ν_{OH}) of the OH-3Co group surrounded by three cobalt atoms and the Si-O vibration mode (ν_{SiO}). In addition, the peak at 663 cm^{-1} is attributed to the superimposition of δ_{OH} vibration of the OH-3Co group and ν_{SiO} vibration mode, and the peak located at 451 cm^{-1} is assigned to the asymmetric Si-O bending vibration.⁵⁷ Furthermore, the shoulder peak at 925 cm^{-1} arises from the vibration of silanol (Si-OH) groups,⁵⁸ which is, interestingly, more pronounced in the case of pristine ACP unlike other peaks. It is known that silanol groups do not exist in a perfect layered cobalt phyllosilicate, on the other hand, the defective structure can induce them by bonding four protons with oxygens surrounding Si^{4+} vacant site to compensate the charge imbalance which is called a hydrogarnet-type substitution.^{59,60} We expect that the rapid precipitation reaction causes the loss

of long range ordering with defective silicate chains in the ACP, which results in silanol groups at the basal plane of silicate oxygen.

The chemical composition of the ACP was examined by the electron probe micro-analysis (EPMA). The average atomic percentage of Co, Si and O is found to be 15.1, 16.6 and 68.3, respectively, indicating that the atomic ratio of Co:Si:O is approximately 1:1:4 (see Table 5-1). It suggests that the ACP cannot be solely assigned as either $\text{Co}_3\text{Si}_2\text{O}_5(\text{OH})_4$ or $\text{Co}_3\text{Si}_4\text{O}_{10}(\text{OH})_2$. Previous study suggested that non-stoichiometric phyllosilicate could be synthesized with Si vacancy in silicate layer.⁶⁰ Therefore, it is speculated that the ACP is a layered structure of CoO_6 sheets with non-stoichiometric polysilicate sheets between CoO_6 layers. Besides, the variation of the Co/Si atomic ratio with different precursor ratio was also investigated as shown in Figure 5-5. The Co/Si ratio of prepared samples, however, maintains a value of approximately 1. In addition, the XRD patterns in Figure 5-6 showed no particular change regardless of the precursor ratio. Furthermore, catalytic activities of the samples with different precursor ratio did not change in Figure 5-7, as will be discussed in detail later. These results suggest that regardless of the atomic ratio of the reactant, all the ACPs have similar properties with 1:1:4 atomic ratio of Co, Si, and O.

Based on the basic cobalt phyllosilicate structure ($\text{Co}_3\text{Si}_2\text{O}_5(\text{OH})_4$ and $\text{Co}_3\text{Si}_4\text{O}_{10}(\text{OH})_2$), the aforementioned experimental observations of the atomic ratio of 1:1:4 (Co:Si:O) and the existence of the silanol group originated from Si vacancy, a model crystal structure of the ACP could be constructed with a

possible molecular formula of $\text{Co}_3\text{Si}_3\text{O}_6(\text{OH})_6$. Figure 5-8 shows the optimized structure of $\text{Co}_3\text{Si}_3\text{O}_6(\text{OH})_6$ calculated by DFT. ACP (right panel) adopts a similar crystal structure to CoOOH (left panel) having a series of CoO_6 layers except for the silicate groups which only exist in the ACP between CoO_6 layers. While the perfect layered cobalt phyllosilicate structures have a complete interconnection of the silicates with hexagonal orderings in the layer, the ACP does not contain it because the ACP includes Si vacancy (See Figure 5-9 ~ Figure 5-11).

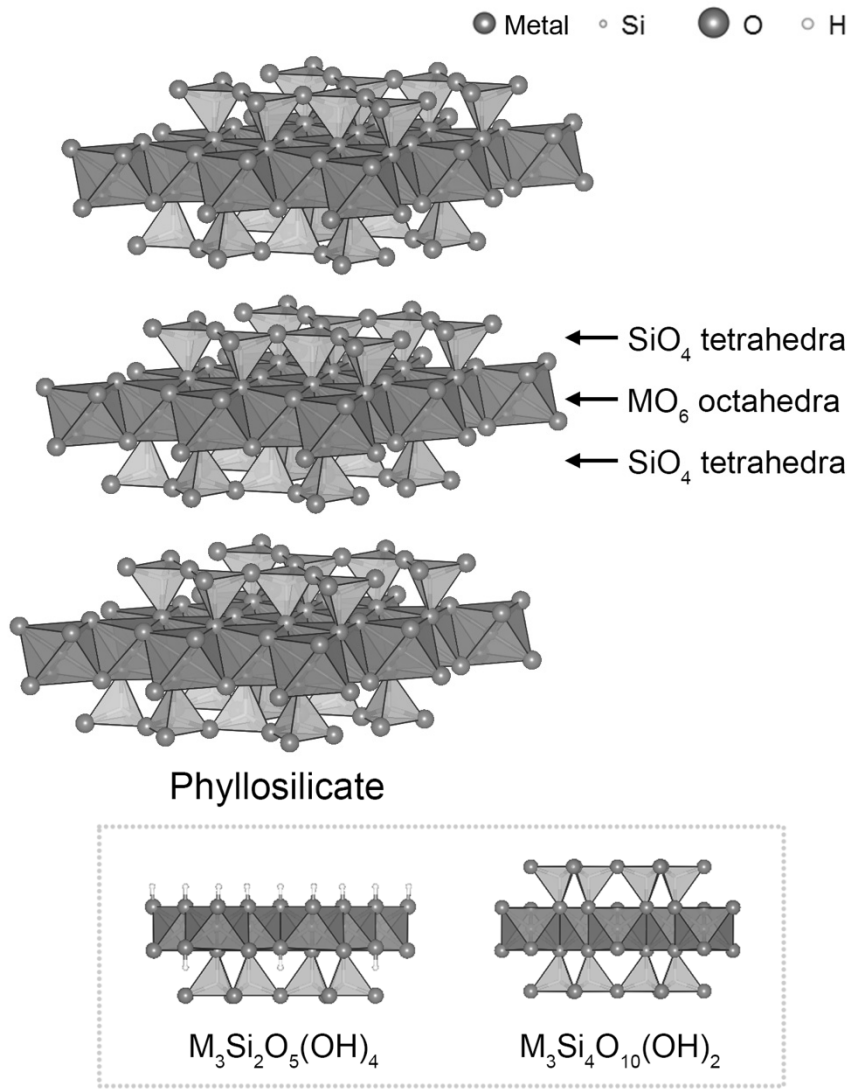


Figure 5-1. Crystal structure of phyllosilicate. (Inset: two kinds of phyllosilicate)

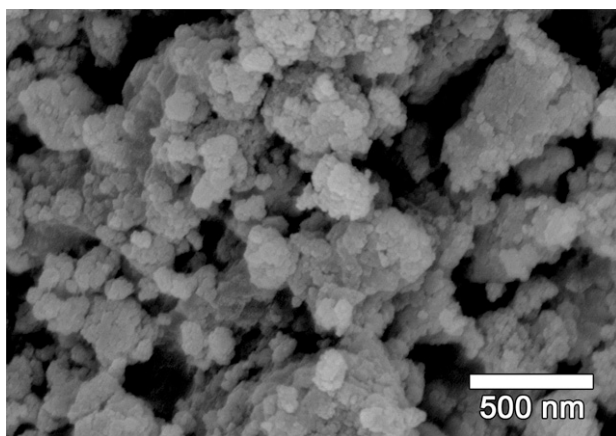


Figure 5-2. SEM image of ACP prepared by co-precipitation method

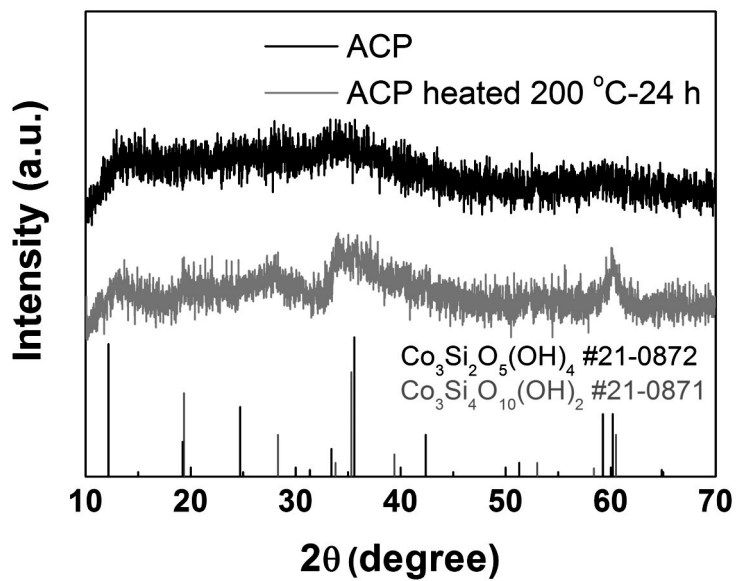


Figure 5-3. Powder X-ray diffraction patterns of the ACP and heated ACP by hydrothermal method.

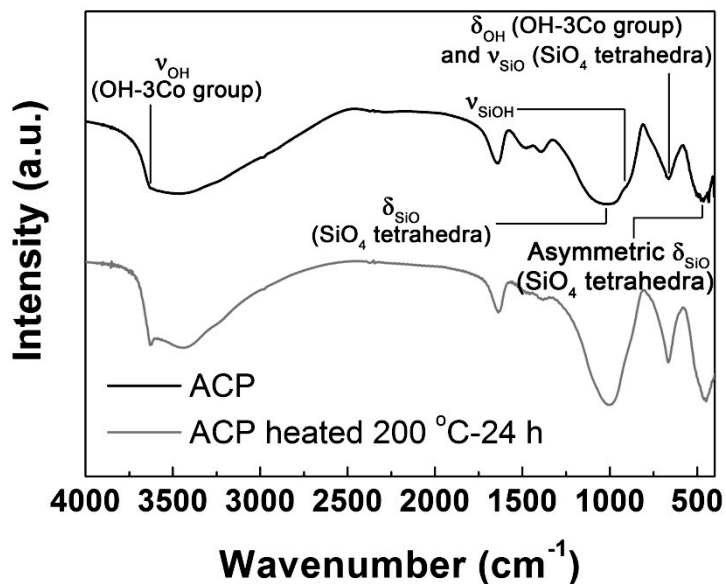


Figure 5-4. Fourier transform infrared (FT-IR) of the ACP and heated ACP by hydrothermal method.

Table 5-1. Element ratio of ACP prepared by Co/Si precursor ratio 3:4.

Atomic %	Co	Si	O	Total
1	15.2370	16.9800	67.7830	100
2	15.2880	16.7550	67.9570	100
3	14.9050	16.1720	68.9230	100
4	15.5140	16.2910	68.1950	100
5	14.1640	16.3480	69.4880	100
6	15.8550	16.1880	67.9570	100
7	15.8800	16.2280	67.8920	100
8	15.7460	16.6800	67.5740	100
9	14.6480	16.6420	68.7090	99.9991
10	13.6870	17.6050	68.7080	100
Minimum	13.6870	16.1720	67.5740	99.999
Maximum	15.8800	17.6050	69.4880	100
Average	15.0924	16.5889	68.3186	99.9999
Sigma	0.7405	0.4516	0.6089	0.0003

Table 5-2. Element ratio of ACP prepared by Co/Si precursor ratio 3:2.

Atomic %	Co	Si	O	Total
1	17.8052	16.6459	65.5488	99.9999
2	18.309	17.0327	64.6582	100
3	18.7051	17.0357	64.2591	100
4	18.4406	17.1022	64.4572	100
5	17.1556	17.0722	65.7721	100
6	17.9667	17.1461	64.8871	99.9999
7	17.8551	16.8829	65.2621	100.0001
8	17.2881	17.0903	65.6216	100
9	17.9226	17.0617	65.0157	100
10	18.1698	17.0738	64.7565	100
Minimum	17.1556	16.6459	64.2591	99.9999
Maximum	18.7051	17.1461	65.7721	100.0001
Average	17.96178	17.01435	65.02384	99.99999
Sigma	0.481532	0.14674	0.514176	0.0001

Table 5-3. Element ratio of ACP prepared by Co/Si precursor ratio 3:3.

Atomic %	Co	Si	O	Total
1	16.9444	17.2187	65.8369	99.9999
2	17.1050	17.2684	65.6266	100
3	16.9687	17.1843	65.8470	100
4	16.3455	16.9876	66.6669	100
5	16.9389	16.8475	66.2137	100
6	17.2813	17.7745	64.9442	99.9999
7	17.4824	17.3875	65.1301	100
8	17.6743	17.2714	65.0543	100
9	16.9067	16.9744	66.1189	100
10	16.3982	16.9100	66.6919	100
Minimum	16.3455	16.8475	64.9442	100
Maximum	17.6743	17.7745	66.6919	100
Average	17.00454	17.18243	65.81305	100
Sigma	0.419574	0.274238	0.631489	4.22E-05

Table 5-4. Element ratio of ACP prepared by Co/Si precursor ratio 3:5.

Atomic %	Co	Si	O	Total
1	13.8897	15.2299	70.8804	99.9999
2	13.6022	15.7910	70.6068	100
3	13.6276	15.5769	70.7955	100
4	13.7903	15.3951	70.8146	100
5	13.3143	15.2325	71.4532	100
6	13.6235	15.7465	70.6299	99.9999
7	13.5420	15.6710	70.7870	100
8	14.7059	16.0553	69.2387	100
9	13.6650	15.6270	70.7080	100
10	13.3806	14.9869	71.6324	100
Minimum	13.3143	14.9869	69.2387	99.9999
Maximum	14.7059	16.0553	71.6324	100
Average	13.71411	15.53121	70.75465	99.99999
Sigma	0.38753	0.318701	0.634056	3.16E-05

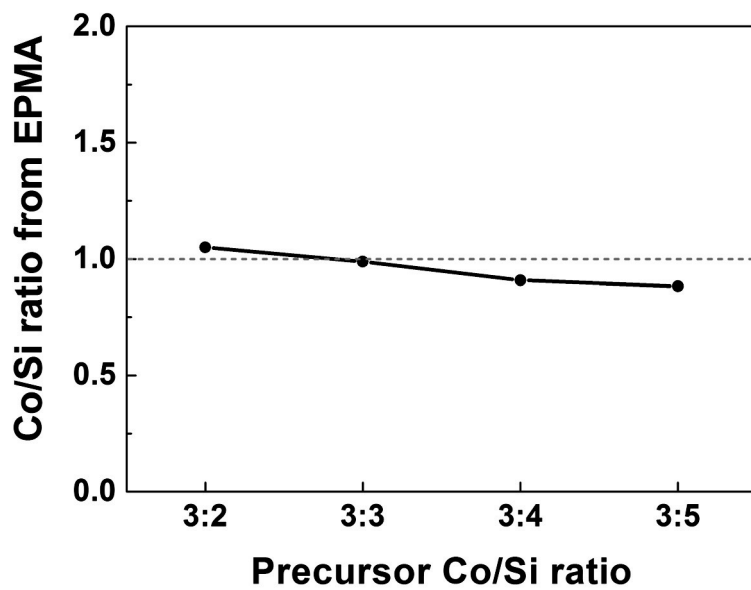


Figure 5-5. The variation of the Co/Si ratio with different precursor ratio.

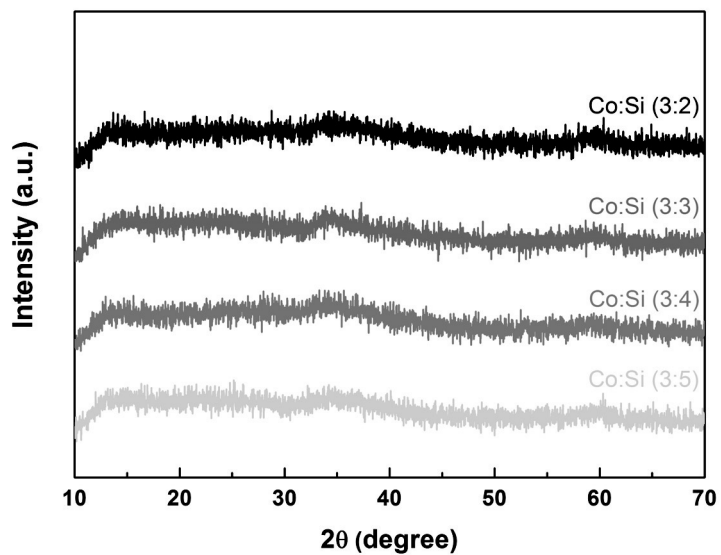


Figure 5-6. Powder X-ray diffraction patterns of ACP with different precursor ratio.

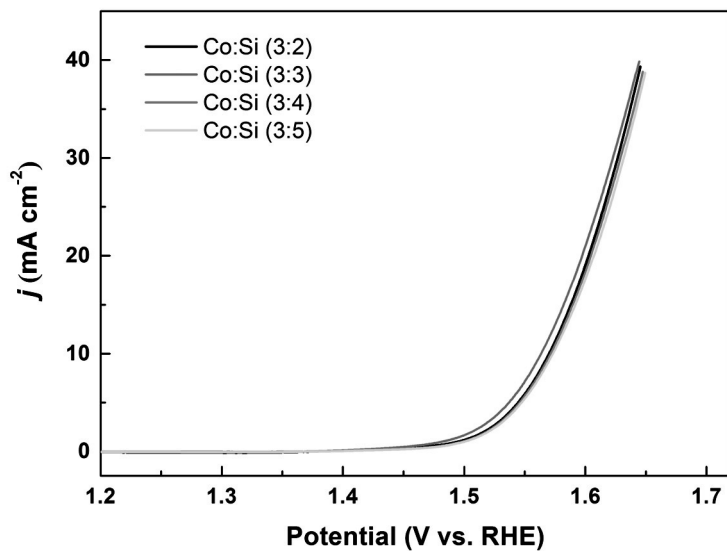


Figure 5-7. Polarization curves of ACP in 1 M KOH electrolyte with different precursor ratio.

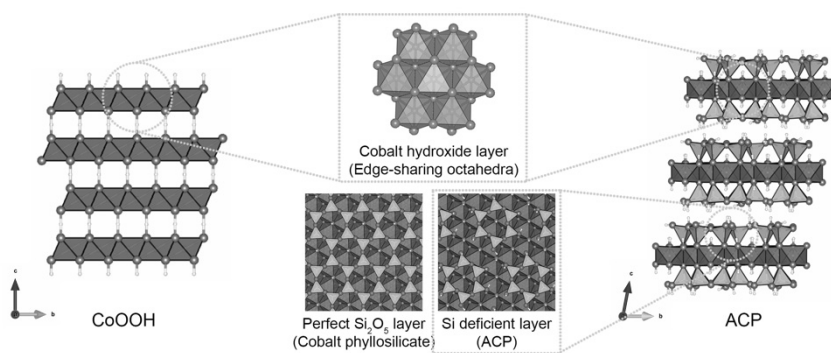


Figure 5-8. Schematic representation of CoOOH and ACP structure. CoOOH and the ACP consist of edge-sharing CoO_6 octahedra. The silicate layer of ACP features Si-deficient structure in contrast with the ideal phyllosilicate structure composed of hexagonal tetrahedral ring.

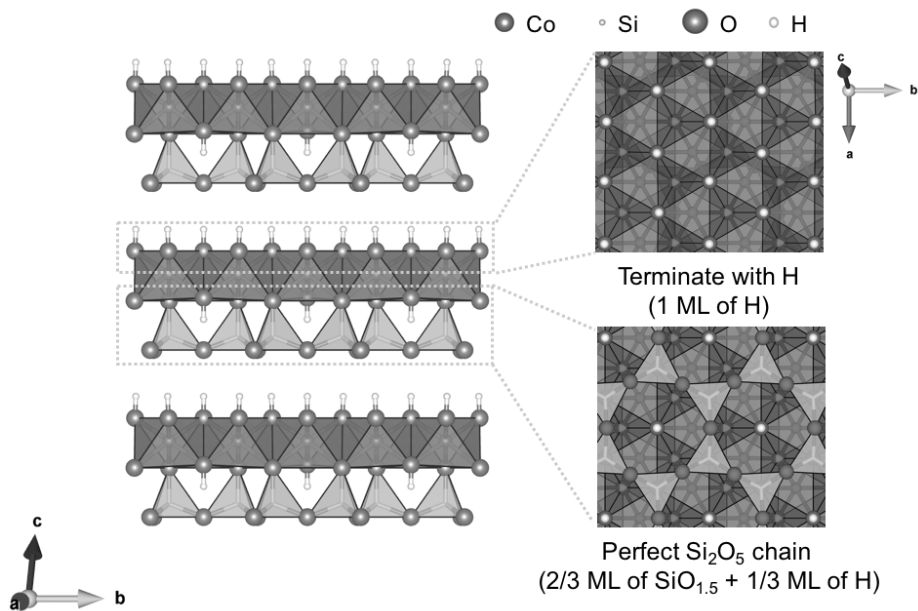


Figure 5-9. Structure of cobalt phyllosilicate $\text{Co}_3\text{Si}_2\text{O}_9\text{H}_4$. $\text{Co}_3\text{Si}_2\text{O}_9\text{H}_4$ consist of cobalt hydroxide layer and perfect hexagonal silicate chains at one sides of cobalt layers. The other side is terminated with hydrogen. Co, Si, O, and H are shown as blue, green, red and white spheres, respectively.

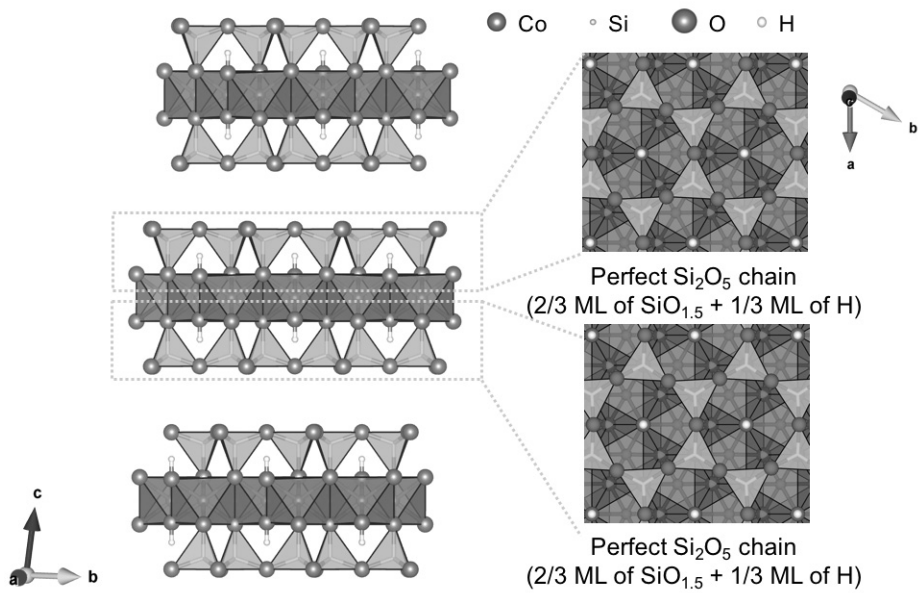


Figure 5-10. Structure of cobalt phyllosilicate $\text{Co}_3\text{Si}_4\text{O}_{12}\text{H}_2$. $\text{Co}_3\text{Si}_4\text{O}_{12}\text{H}_2$ consist of cobalt hydroxide layer and perfect hexagonal silicate chains at both sides of cobalt layers. Co, Si, O, and H are shown as blue, green, red and white spheres, respectively.

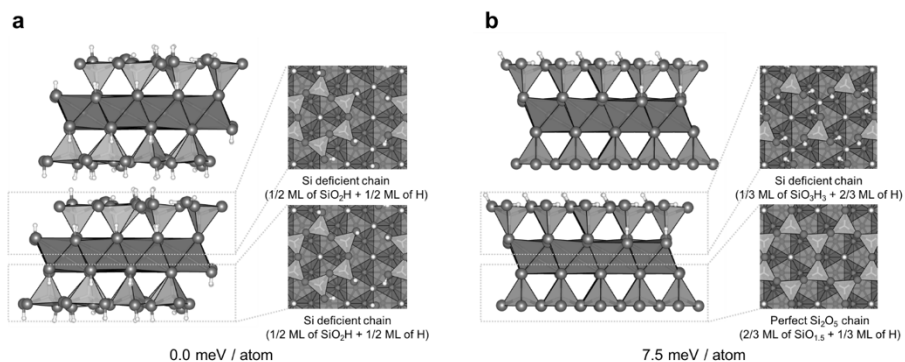


Figure 5-11. Calculated structure of ACP ($\text{Co}_3\text{Si}_3\text{O}_{12}\text{H}_6$). From reported structures of cobalt phyllosilicate ($\text{Co}_3\text{Si}_2\text{O}_9\text{H}_4$ and $\text{Co}_3\text{Si}_4\text{O}_{12}\text{H}_2$), we predicted structural motif of ACP with $\text{Co}:\text{Si}:\text{O} = 1:1:4$ using DFT calculations. Hydrogen atoms added to maintain Co oxidation state as 2+. (a) Homogeneous model with Si deficient chain at both side of cobalt hydroxide layer shows much stable energy (7.5 meV per atom) than that of (b) Inhomogeneous model with Si deficient chain at one side of cobalt hydroxide layer. Co, Si, O, and H are shown as blue, green, red and white spheres, respectively.

The OER catalytic activity of the ACP was evaluated by cyclic voltammetry (CV) under 1 M KOH alkaline solution in a three-electrode system and compared with well-known cobalt based catalysts such as CoOOH nanoplates (NLs) and Co₃O₄ nanoparticles (NPs) (See Figure 5-12a). XRD and SEM images of Co₃O₄ NPs and CoOOH NLs are provided in Figure 5-13 – Figure 5-16. *iR*-corrected CV curves of the ACP exhibit the lowest onset potential and overpotential (η) at the same current density, indicating a higher catalytic activity than CoOOH NLs and Co₃O₄ NPs. The overpotential of ACP for OER is approximately 367 mV for the current density of 10 mA cm⁻², whereas CoOOH NLs and Co₃O₄ NPs require 400 mV and 490 mV of overpotential, respectively, which are similar with previous reports.³⁷ (Figure 5-12b). The tafel slopes of ACP, CoOOH NLs and Co₃O₄ NPs are 60, 72 and 74 mV dec⁻¹, respectively, as shown in Figure 5-12c. For more precise comparison, we measured the double-layer capacitances (C_{dl}) of the samples to evaluate the electrochemically active surface area (ECSA) of the catalysts using cyclic voltammetry. Figure 5-12d shows the double layer charging current density differences ($\Delta j = j_a - j_c$ at 1.05 V vs RHE) of the catalysts with respect to the scan rate. The slope of the plot is proportional to the double layer capacitance which indicates the relative surface area. C_{dl} of the CoOOH shows larger value than ACP and Co₃O₄ NPs, as shown in Figure 5-12d. From this result, it can be deduced that higher current density of ACP is not from surface area. Furthermore, the long-term stability test under constant current density of 10

mA cm^{-2} shows that ACP maintains the constant voltage for 24 hours with only slight increase from 1.60 V to 1.66 V. (See Figure 5-12e).

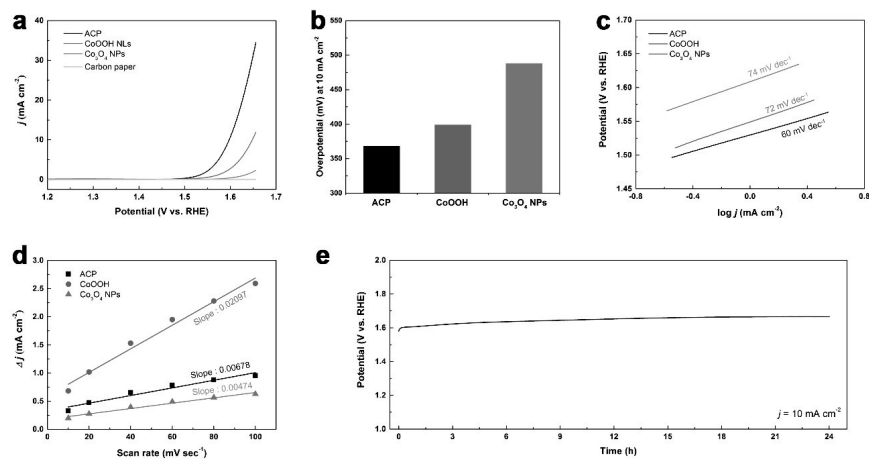


Figure 5-12. Oxygen evolution properties of prepared cobalt based catalysts. (a) *iR*-corrected polarization curves in 1 M KOH at scan rate of 10 mV s⁻¹ and (c) the corresponding tafel plots. (b) OER overpotentials required for 10 mA cm⁻². (d) The plots of differences in current density ($\Delta j = j_a - j_c$) at 1.05 V vs. RHE against scan rate due to evaluate electrochemical double layer capacitance. (e) Long-term stability of the ACP performed under constant current density at $j = 10$ mA cm⁻² for 24 h.

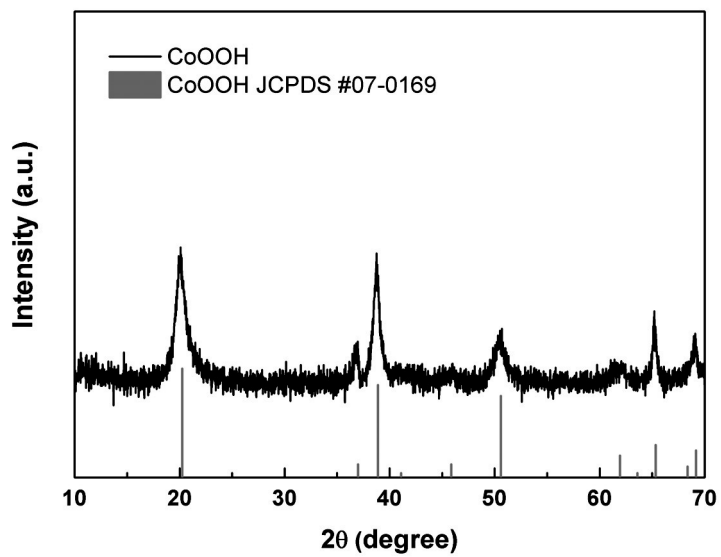


Figure 5-13. Powder X-ray diffraction pattern of CoOOH nanoplates.

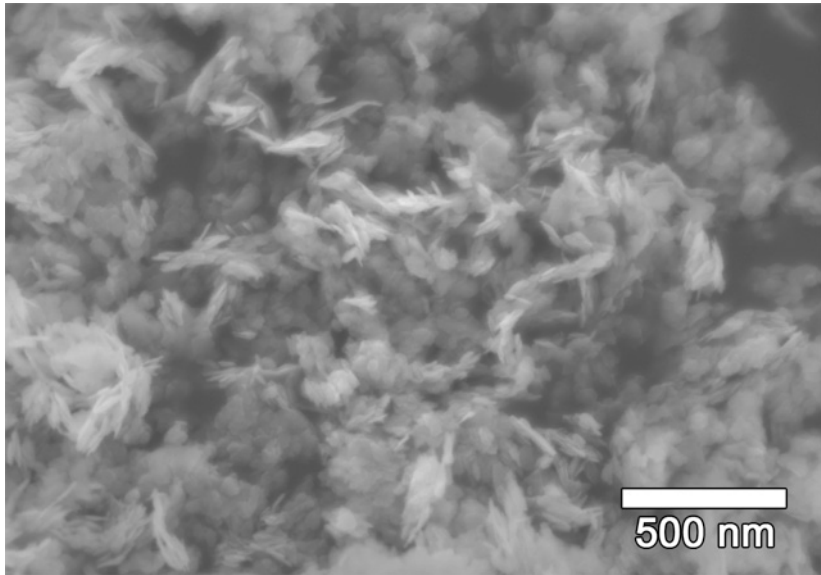


Figure 5-14. SEM image of CoOOH nanoplates.

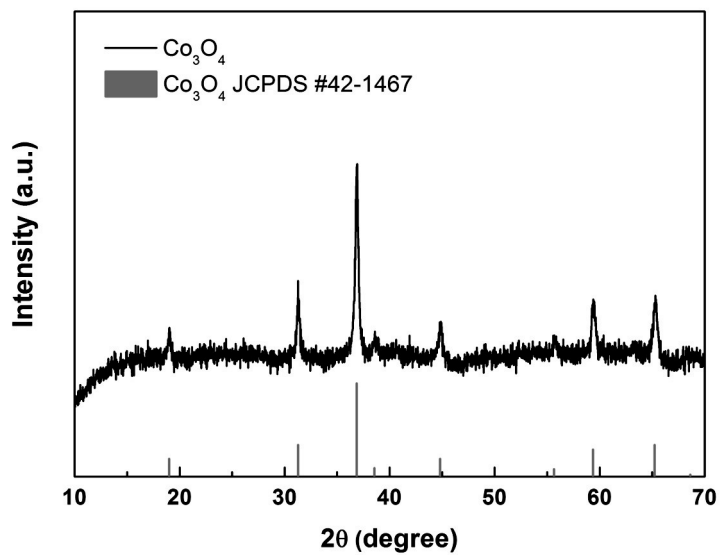


Figure 5-15. Powder X-ray diffraction pattern of Co_3O_4 nanoparticles.

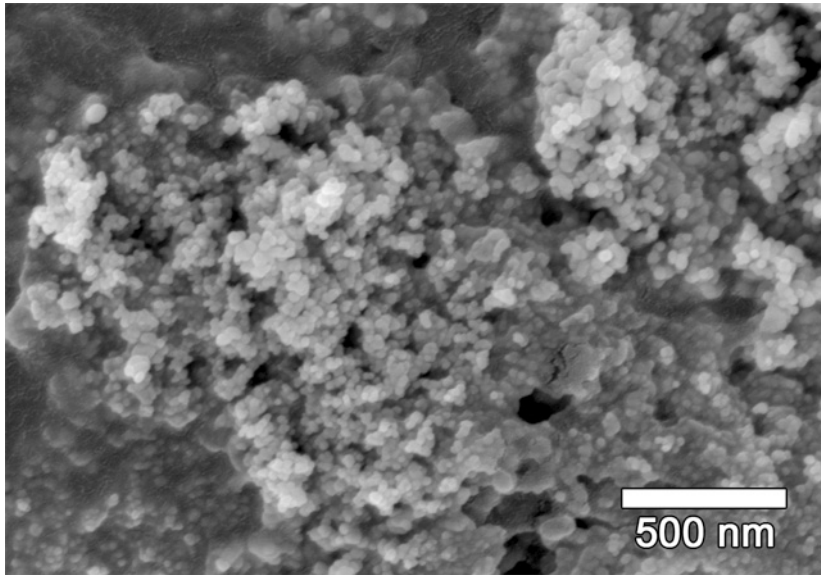


Figure 5-16. SEM image of Co₃O₄ nanoparticles.

In order to probe the changes in Co oxidation state and local structure after electrolysis, X-ray absorption fine structure (XAFS) analysis was carried out before and after the electrolysis. X-ray absorption near edge structure (XANES) analysis in Figure 3a provides the information on the oxidation state of cobalt ions. The edge position of the as-prepared ACP indicates that the initial oxidation state of the cobalt ion is 2+ consistent with that of the Co(II)O reference. However, it shifts toward a higher energy close to that of the LiCo(III)O₂ reference indicating the oxidation of the cobalt ion to 3+ after the electrolysis. This irreversible electrochemical oxidation of cobalt ion from 2+ to 3+ is well known in the case of the cobalt hydroxide catalysts such as the Co(OH)₂/CoOOH.⁶¹⁻⁶³ Although the reason for the irreversible electrochemical oxidation is not clear, it is attributable to more stable characteristic of Co³⁺ (low-spin configuration of *d*⁶) than Co²⁺ (low-spin configuration of *d*⁷) in the alkaline electrolytes and a poor diffusion rate of electrolyte to react reversible oxidation.^{61,64}

Based on the irreversible oxidation of cobalt ions, it can be expected that the oxidation of cobalt ions could accompany permanent changes in the crystal structure. Because the crystal structure around cobalt ion could affect water oxidation properties, it is important to clarify the crystal structure. However, the amorphous nature of ACP makes it difficult to analyze the crystal structure by conventional characterization methods such as XRD. Therefore, the structural information of ACP was further investigated by extended X-ray

absorption fine structure (EXAFS) which is an effective tool for probing the local structure of amorphous materials.^{40,41,49} Figure 3b and c show the k^3 -weighted EXAFS oscillations and their Fourier transformed (FT)-EXAFS spectra, respectively, for the as-prepared ACP, the ACP after electrolysis, and the CoOOH. Note that the x-axis in the FT spectra is the apparent distance, which is shorter than the real distance because the phase shift was not considered. The figures clearly display that the local structure of the ACP becomes similar to that of CoOOH after the electrolysis. All the spectra in Figure 3c show two notable peaks: the first peak (peak I) and second peak (peak II) are attributable to the Co-O shell and Co-Co shell, respectively, as indicated by the EXAFS fits (*vide infra*). For as-prepared ACP, these peaks are located at 1.6 Å and 2.8 Å and shrink to 1.5 and 2.5 Å after electrolysis. This suggests that the irreversible oxidation reaction within electrolysis accompanies the structural contraction due to the smaller ionic size of Co^{3+} . To study the quantitative structural properties around cobalt ions, the EXAFSs of samples are fitted to the EXAFS calculations as shown in Figure 3d, Table 1 and Supplementary Figure S11, S12. The range of more than 3.5 Å was not considered as fitting range due to the low amplitude. The obtained lengths of Co-O and Co-Co for the as-prepared ACP are 2.09 and 3.13 Å, respectively, which are similar to the values for reported $\text{Co}(\text{OH})_2$.⁶¹ After the electrolysis, they decrease to 1.89 and 2.83 Å. In order to investigate whether the silicate layers remain after electrolysis, the FT-EXAFS spectrum of ACP after

electrolysis is fitted with and without Co-Si shell. Adding the contribution of the Co-Si shell shows substantially better fit, indicating that silicate layer maintains structure after electrolysis.

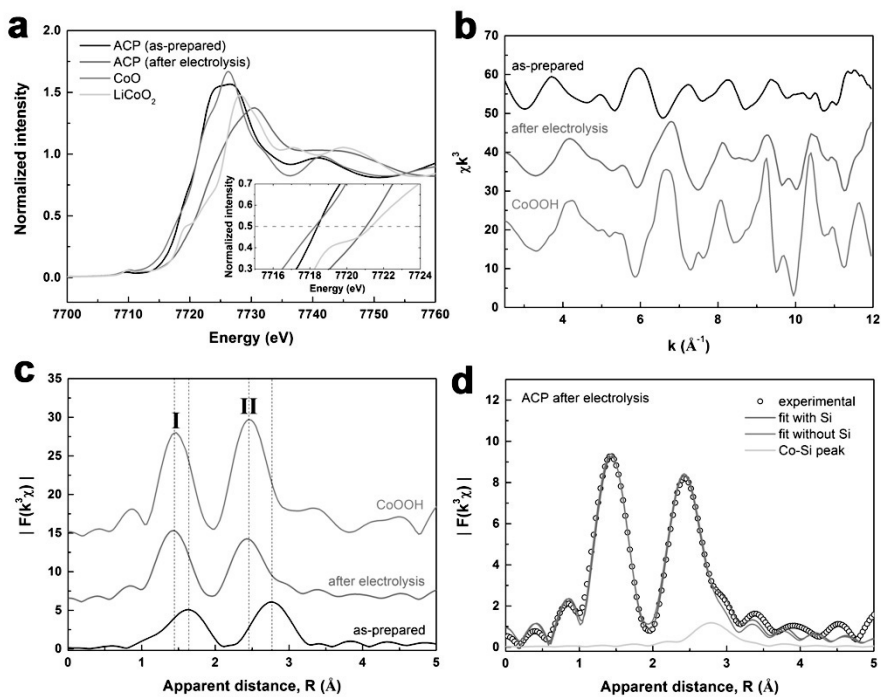


Figure 5-17. (a) XANES cobalt K-edge spectra of the as-prepared ACP and the after 1st CV ACP. For comparison, CoO and LiCoO₂ also shown for reference samples of Co²⁺ and Co³⁺, respectively. (b) Oscillations of the EXAFS spectra and (c) Fourier transformed k^3 -weighted EXAFS spectra of the as-prepared, after electrolysis ACP and CoOOH. (d) Comparison between experimental Fourier transformed EXAFS spectrum (dotted line) of the ACP after electrolysis and theoretical fit (red line).

Table 5-5. Structural parameters of the theoretically fitted FT-EXAFS in **Figure 5-17d**.

Sample	Co-O			Co-Co			Co-Si		
	N	d (Å)	σ^2 (Å ²)	N	d (Å)	σ^2 (Å ²)	N	d (Å)	σ^2 (Å ²)
As-prepared ACP	5.1(8)	2.089(6)	0.009(1)	5.4(8)	3.13(1)	0.011(1)	2.4(2)	3.41(2)	0.006(3)
After electrolysis	5.0(9)	1.893(1)	0.004(1)	5.0(6)	2.826(6)	0.006(1)	2.0(4)	3.296(14)	0.007(2)
CoOOH	6.0(7)	1.898(6)	0.003(1)	6.0(7)	2.853(6)	0.003(1)			

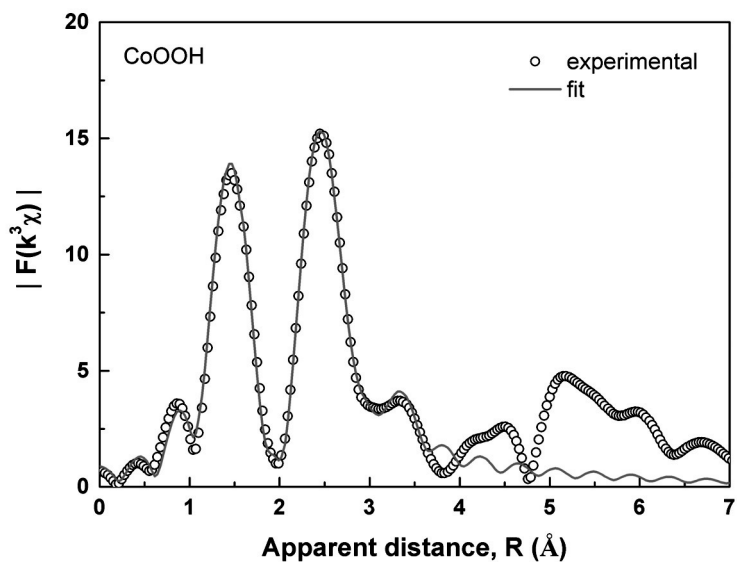


Figure 5-18. Comparison between experimental Fourier transformed EXAFS spectrum (dotted line) of the CoOOH nanoplates and theoretical fit (red line).

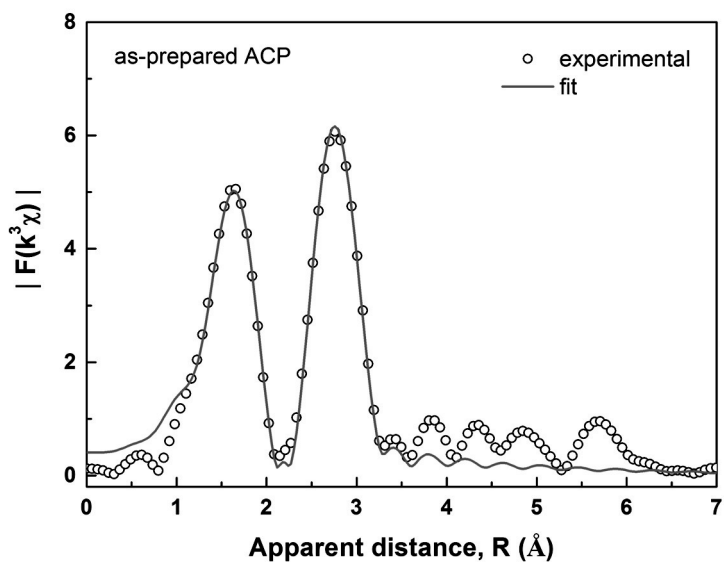


Figure 5-19. Comparison between experimental Fourier transformed EXAFS spectrum (dotted line) of as-prepared ACP and theoretical fit (red line).

It is noteworthy that the significant difference between ACP and CoOOH is the existence of the silicate in the structure only, while changes in the Co oxidation state and the local structure are almost identical. Thus, it is expected that the redox inactive silicate in the ACP could affect the catalytic reaction. In order to understand the role of the silicate in the catalytic reaction on an atomistic level, we comparatively investigated OER thermodynamics of CoOOH and ACP with DFT calculations. Figure 4 compares the surficial atomic geometry of (a, c) CoOOH and (b, d) ACP at OER operating voltage range. We closely examined the (10 $\bar{1}$ 4) surface of the CoOOH since it is the most OER active surface for cobalt hydroxide based on the previous work of Bell *et al.*⁶⁵ Due to the structural similarity between CoOOH and the ACP, we also could probe the ACP surface which has a similar atomic arrangement to the CoOOH (10 $\bar{1}$ 4) surface (See Supplementary Figure S13-S16 for detailed surface cleavage procedure). There are two major structural differences between the surface of CoOOH and the ACP. The first difference is the interlayer distance. Cobalt layers in CoOOH share hydrogen atoms via the hydrogen bonding between the layers. It makes possible for cobalt layers to closely bind with each other (See Figure 4a). In contrast, cobalt layers in ACP have longer interlayer distance because large silicate polyanions exist between the layers (See Figure 4b). As a result, the interaction between the cobalt layers in ACP is weaker than CoOOH. The second difference is the diversity of surficial reaction sites. Figure 4c shows oxygen sites on the surface of CoOOH.

There are only two kinds of active sites on the surface of CoOOH: on-top site of a single 5-fold coordinated cobalt ions (terminal site, denoted as O_t) and bridge di- μ -oxo site between two 5-fold coordinated cobalt ions (bridge site, denoted as O_b). On the other hand, ACP surface can have various active sites as shown in Figure 4d. Silicate groups which are bound to some fraction of oxygen site modulate the environments of active sites. Thus, the ACP surface has various surficial oxygen sites, *e.g.* terminal 1 site (denoted as O_{t1}) exists as OH_2 while terminal 2 site (denoted as O_{t2}) is bound with silicate. In addition, the bridge 1 site (denoted as O_{b1}) and the bridge 2 site (denoted as O_{b2}) are in different environments from each other. Therefore, these active sites could have unequal reactivity.

Silicate groups at the ACP surface modulate (either facilitate or prohibit) the OER reactivity of each active site depending on configurational relationship between silicate groups and active sites. Figure 5a shows the theoretical overpotential for OER occurring at various active sites on the ACP surface and the CoOOH. Note that terminal 3, terminal 4, bridge 3 and bridge 4 sites are not denoted from Figure 4d. These sites are found in another possible atomic configuration of the ACP (See Supplementary Figure S15). It is revealed that the bridge 1 site on the ACP surface exhibits much lower overpotential (340 mV) than the bridge site (570 mV) and the terminal site (530 mV) on the CoOOH surface,⁶⁵ while other active sites show comparable or much higher overpotential.

Figure 5b compares free energy landscape of OER occurring at bridge 1 site on the ACP surface (black line) to those of OER occurring at bridge site (cyan line) and the terminal site (blue line) on the CoOOH surface. Note that standard condition ($T = 298.15$ K, $P = 1$ bar, and $\text{pH} = 0$) and thermodynamic equilibrium potential for the water oxidation are assumed in this slab model calculations. OER pathways and the catalytic activities at the other sites on the ACP surface are shown in Supplementary Figure S17-S24. At the bridge 1 site on the ACP surface, the potential-limiting step for OER is the OOH* forming step which is the same to the active sites on the CoOOH surface.⁶² However, much stable OOH* adsorption is found for the bridge 1 site on the ACP surface than the CoOOH surface, which leads to much lower theoretical overpotential. The origin of this stabilization can be rationalized by the structural flexibility of ACP surface. Figure 5c-e show the atomic configurations around the active sites for the O* intermediate (left panel) and the OOH* intermediate (right panel) respectively for the bridge 1 site on the ACP surface, and the bridge site and terminal site on the CoOOH surface for comparison. Distance between the cobalt layers in the ACP is significantly longer, thus less interlayer O-H-O hydrogen bonds exist in case of the ACP. Therefore, atoms at the silicate layers could adjust their position and stabilize structure of ACP more easily compared to the oxide cases.

A remarkable difference in the structural adjustment between ACP and cobalt hydroxide is the change of the Co - O* bond lengths during OOH*

forming step. Trends in Co-O* distance by reaction coordinate are similar for all three cases: The O* intermediates show shorter Co-O* distances (*i.e.* stronger bonding) than the OOH* intermediates because of the stronger attraction between higher valence species in O* (*i.e.* Co⁴⁺ and O²⁻ for O* intermediate, Co³⁺ and O⁻ for OOH* intermediate). Despite those similar trends, we found a notable distinction of the Co - O* bond length adjustment between ACP and cobalt hydroxide cases. In the OOH* forming step, bridge 1 site on the ACP surface shows much greater changes in Co - O* distances than the CoOOH cases. Another structural difference is the changes occurring in the hydrogen bond length between oxygen and hydrogen atoms adjacent to the active sites (See Figure 5b-d). This structural difference is attributable to the lack of the interlayer O-H-O bonds in the silicate, which offers flexibility to OH₂ group. Thus, OOH* intermediate at bridge 1 site on the ACP surface could have more stable structure with short hydrogen bond length, leading to the low overpotential in overall OER reaction. These results suggest that interlayer distance between cobalt layers affects the OER thermodynamics while silicate in the ACP modulates active site reactivity and interlayer space between cobalt layers.

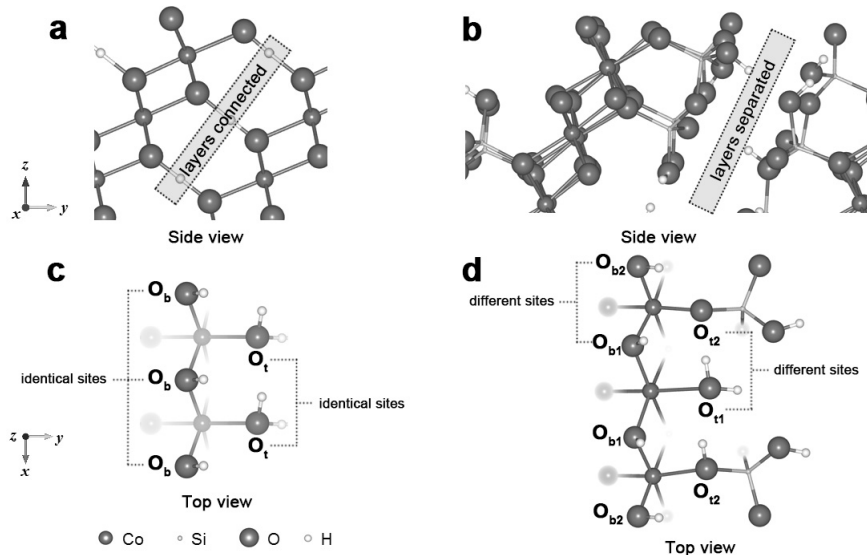


Figure 5-20. Surface structures of OER active surface from (a, c) CoOOH surface and (b, d) ACP surface. (a) Side view for the CoOOH ($10\bar{1}4$) surface which is most active surface for OER. (b) Side view for the CoOOH surface with similar atomic configuration to the CoOOH ($10\bar{1}4$) surface. The ACP surface has longer interlayer distance than CoOOH. Top view for active surface of (c) CoOOH and (d) ACP shows active sites for OER. Co, Si, O, and H are shown as blue, green, red and white spheres, respectively. To clarify, we reveal only topmost atoms.

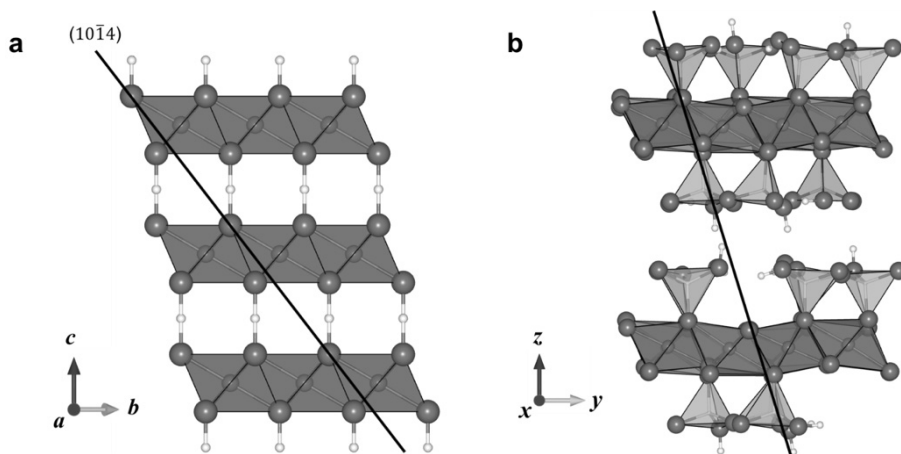


Figure 5-21. Crystal structure of (a) CoOOH and (b) ACP; Cleavage lines are given in black. Note that the $(10\bar{1}4)$ surface is the most OER active surface from CoOOH. Cleavage line for ACP has similar atomic configuration to the CoOOH $(10\bar{1}4)$ surface and silicate tetrahedron is preserved.

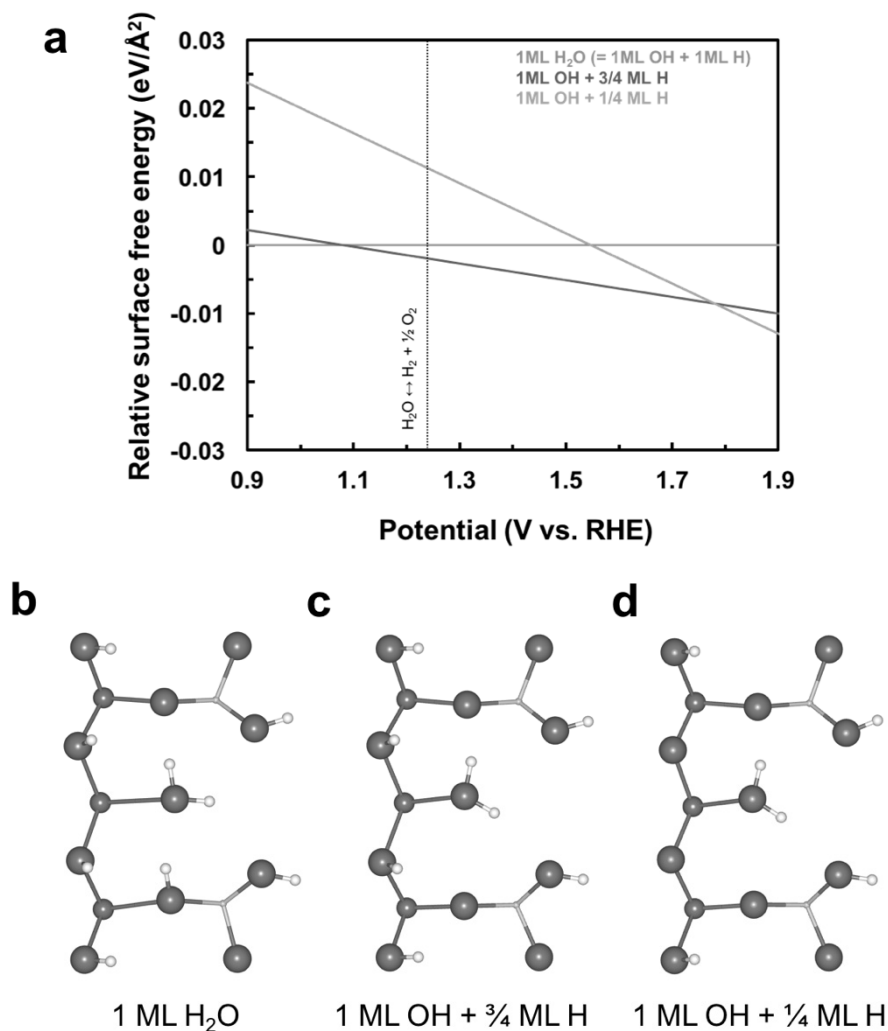


Figure 5-22. Surface termination of ACP surface (model 1) corresponds to the potential. (a) Surface phase diagram as a function of applied potential for ACP surface model. Stable surface structures with adsorbates corresponds to applied potential: (b) with 1 monolayer (ML) of co-adsorbed H₂O (below 1.1 V), (c) with 1 ML of OH and 3/4 ML of H (from 1.1 V to 1.8 V), and (d) with 1 ML of OH and 1/4 ML (above 1.8 V). To clarify, only topmost atoms are shown.

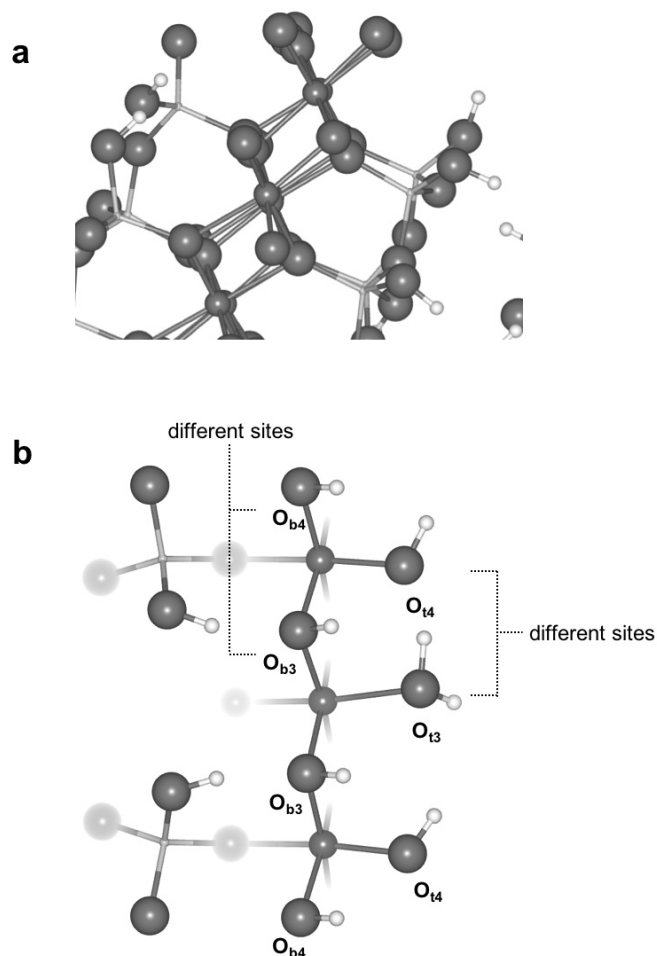


Figure 5-23. Surface structures of another surface of ACP model (model 2). Different from ACP surface model in the **Figure 5-20**, silicates are adsorbed at the bridge site rather than terminal site. (a) Side view for the CoOOH surface with similar atomic configuration to the CoOOH (101 $\bar{4}$) surface. (b) Top view for active surface of ACP shows active sites for OER. Co, Si, O, and H are shown as blue, green, red and white spheres, respectively. To clarify, only topmost atoms are shown.

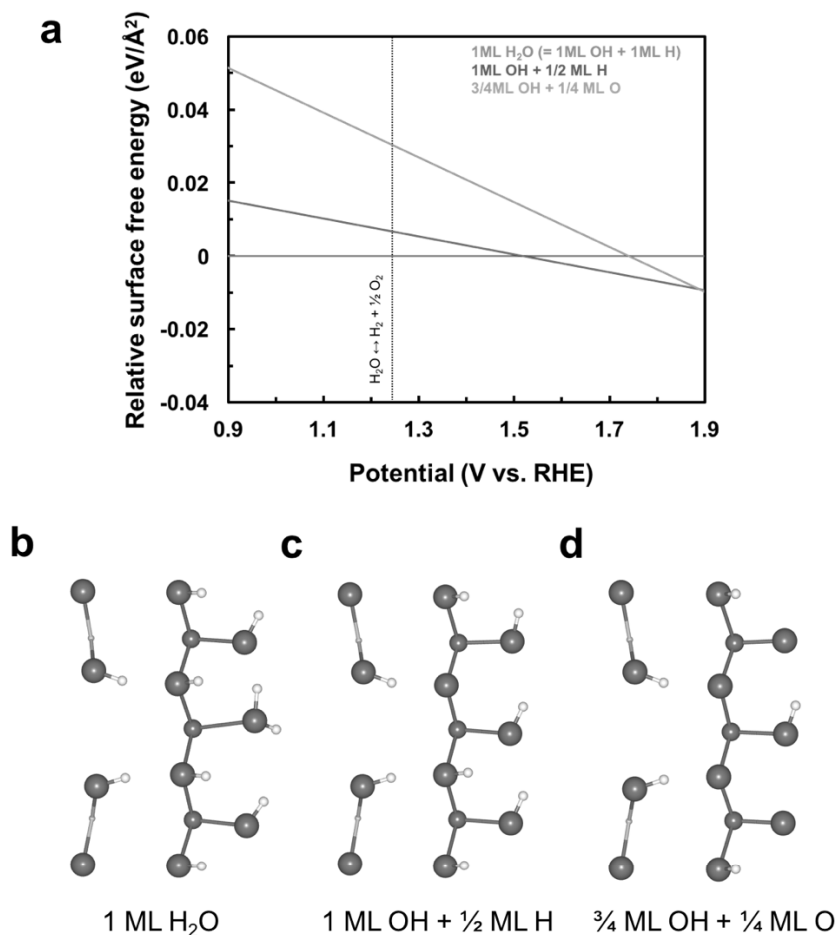


Figure 5-24. Surface termination of another ACP surface (model 2) corresponds to the potential. (a) Surface phase diagram as a function of applied potential for ACP surface model. Stable surface structures with adsorbates corresponds to applied potential: (b) with 1 monolayer (ML) of co-adsorbed H₂O (below 1.1 V), (c) with 1 ML of OH and 3/4 ML of H (from 1.1 V to 1.8 V), and (d) with 1 ML of OH and 1/4 ML (above 1.8 V). To clarify, only topmost atoms are shown.

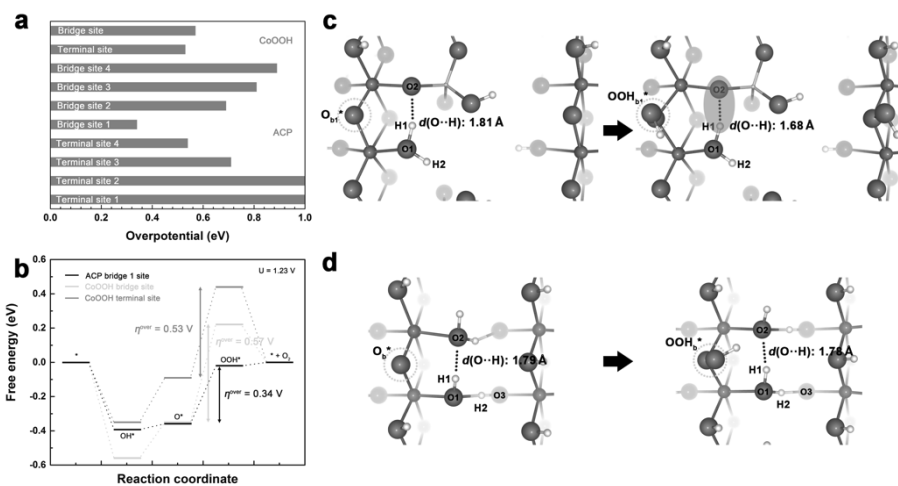


Figure 5-25. DFT calculation results for OER at CoOOH and ACP surfaces. (a) Theoretical overpotentials for OER of plausible sites. Some bridge site on ACP surface show much lower overpotential than active sites of CoOOH. (b) Free energy landscape for OER at 1.23 V (ideal potential for OER). Black, cyan and blue line indicate free energy of ACP bridge 1 site, CoOOH bridge site, and CoOOH terminal site, respectively. Comparison of the structures for OOH* forming step (rate-determining step for these cases) at the (c) ACP bridge 1 site, (d) CoOOH bridge site, and (e) CoOOH terminal site. More adjustment in bond-length at the ACP surface lower the OER overpotential.

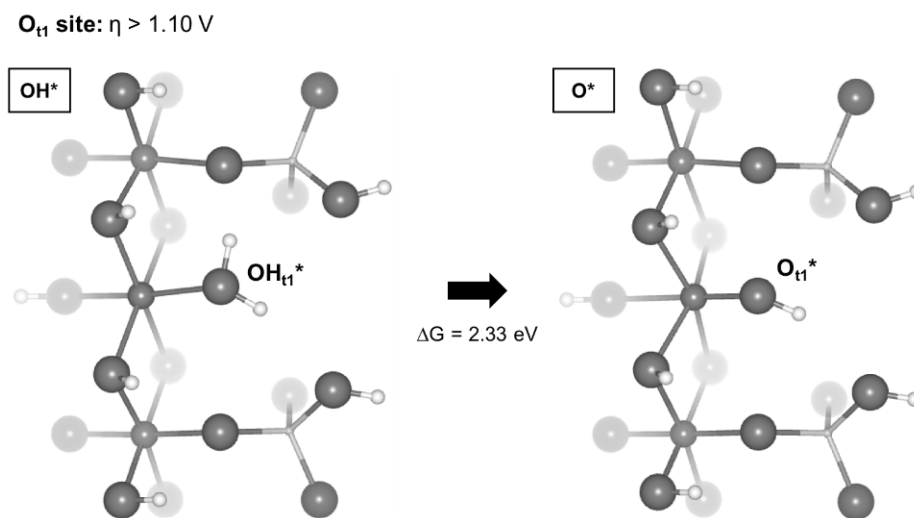


Figure 5-26. OER pathways and calculated minimum overpotential for terminal 1 site on ACP surface (model 1). Deprotonation from terminal 1 site needs more than 2.33 eV, therefore overpotential for OER is higher than 1.1 V.

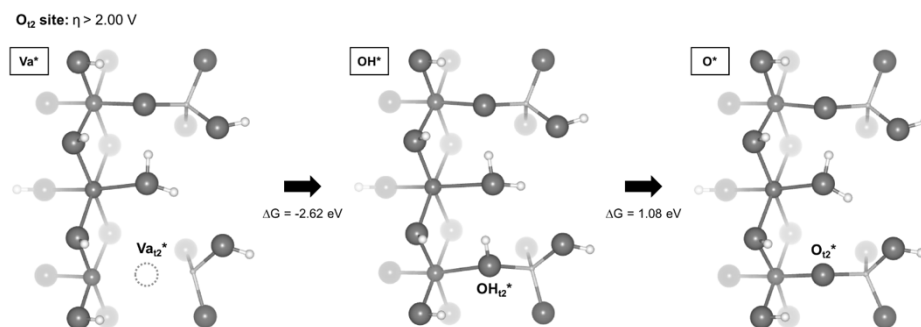


Figure 5-27. OER pathways and calculated minimum overpotential for terminal 2 site on ACP surface (model 1). Vacancy at terminal 2 site is unstable, therefore OH^* adsorption step is spontaneous with $\Delta G = -2.62$ eV. Because $\Delta G_1 + \Delta G_2$ is -1.54 eV, overpotential is higher than 2.00 V. ($\Delta G_3 + \Delta G_4 = 6.46$ eV)

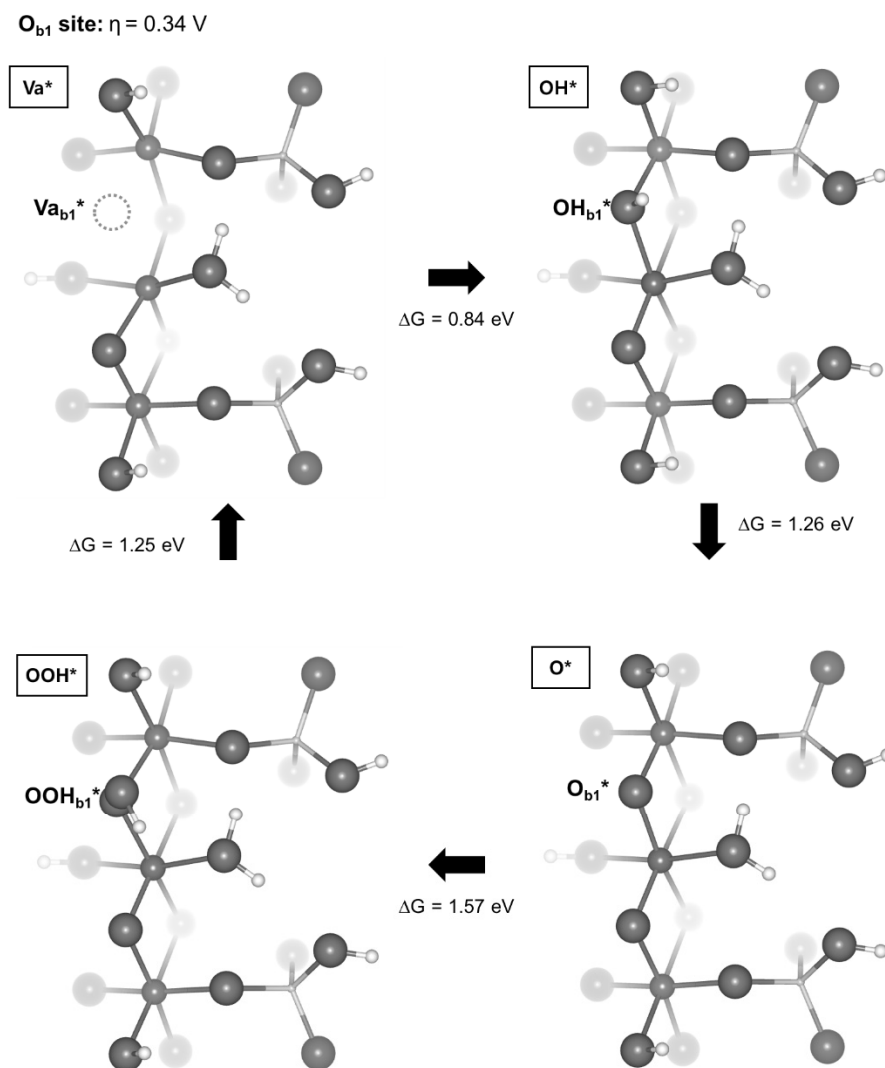


Figure 5-28. OER pathways and calculated minimum overpotential for bridge 1 site on ACP surface (model 1). All the reaction steps at bridge 1 site are stable, therefore OER at bridge 1 site has much lower overpotential than other sites on ACP surface or CoOOH surface.

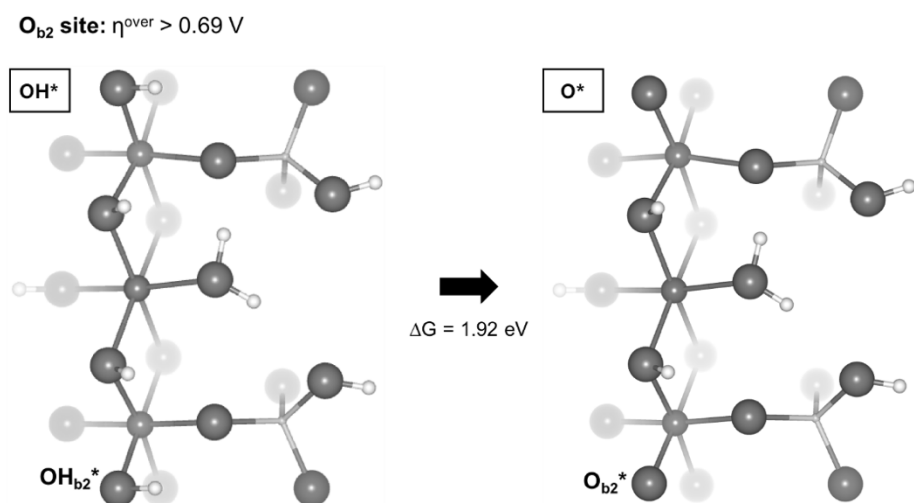


Figure 5-29. OER pathways and calculated minimum overpotentials for bridge 2 site on ACP surface (model 1). Different from that of bridge 1 site, deprotonation from bridge 2 site needs higher than 1.92 eV, therefore overpotential for OER is higher than 0.69 V.

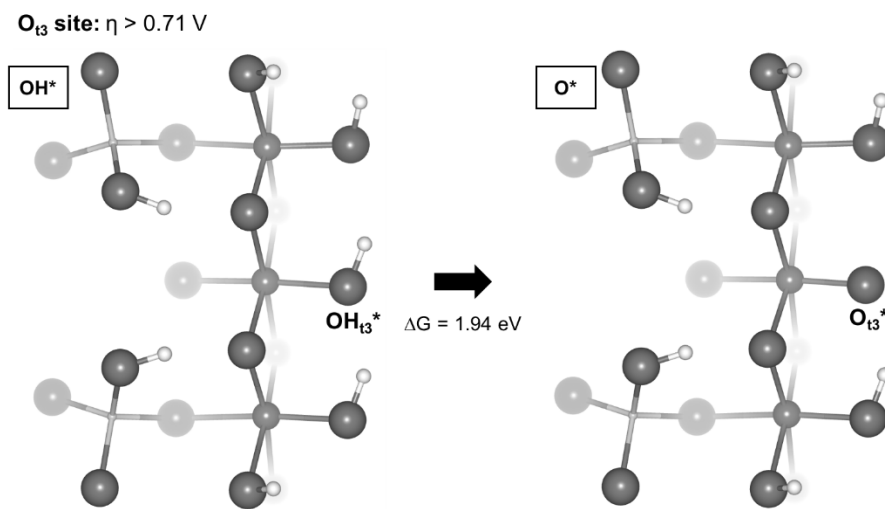


Figure 5-30. OER pathways and calculated minimum overpotential for terminal 3 site on ACP surface (model 2). Deprotonation from terminal 3 site needs high potential of 1.94 V, thus overpotential for OER is higher than 0.71 V.

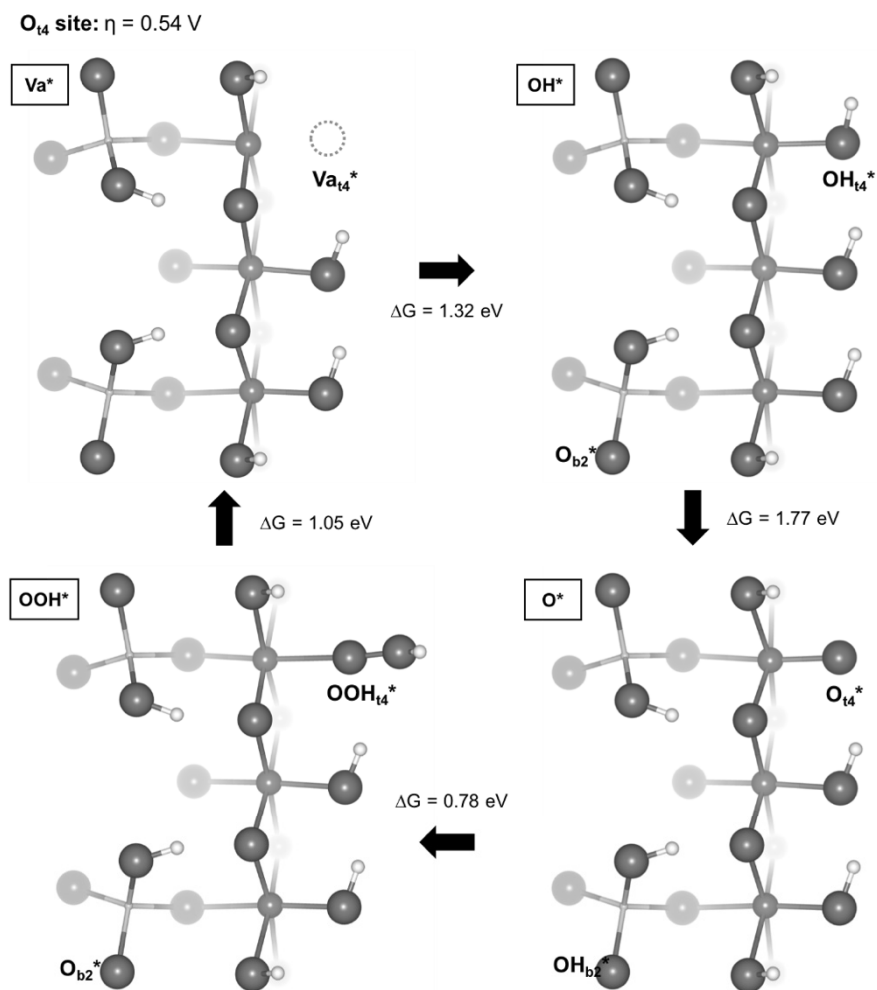


Figure 5-31. OER pathways and calculated minimum overpotential for terminal 4 site on ACP surface (model 2). OER from terminal 4 site shows moderate overpotential of 0.54 V which is similar to the CoOOH case.

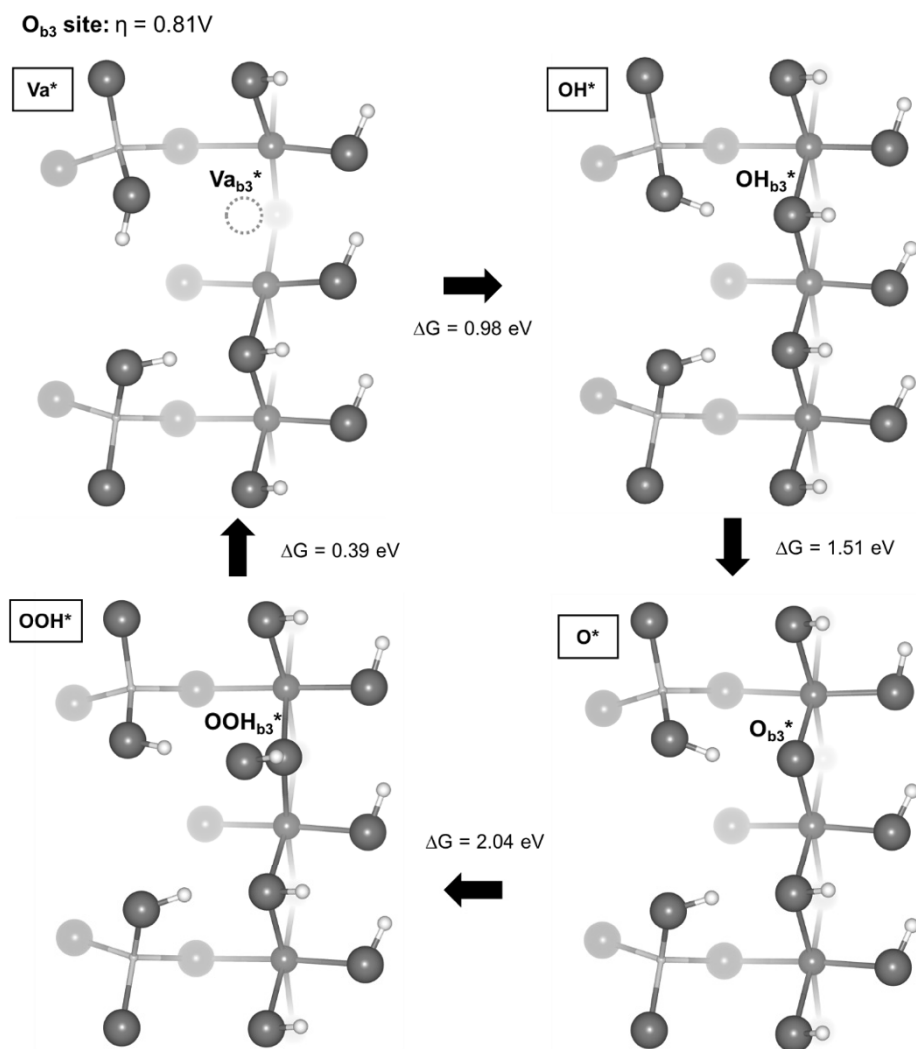


Figure 5-32. OER pathways and calculated minimum overpotential for bridge 3 site on ACP surface (model 2). OER at bridge 3 site shows overpotential of 0.81 V. Rate determining step is OOH* formation step because silicate group does not stabilize OOH* step while does stabilize OH* and O* steps.

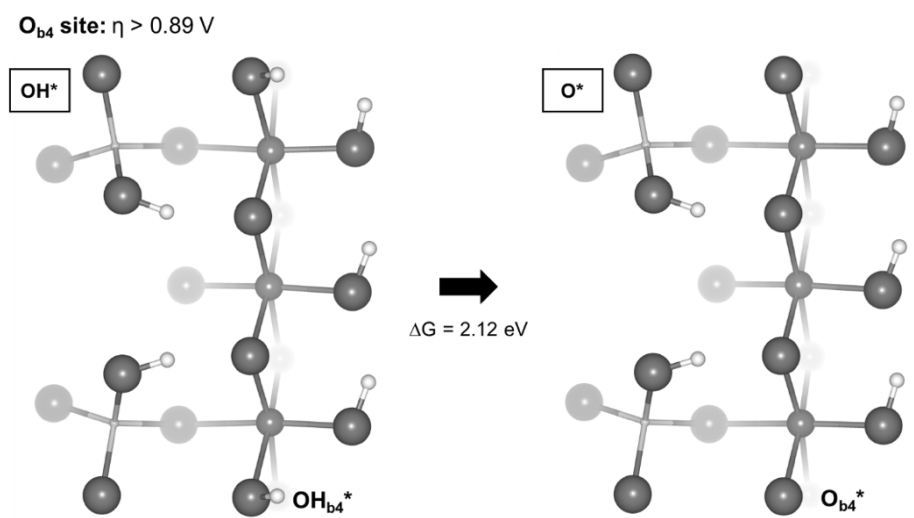


Figure 5-33. OER pathways and calculated minimum overpotential for bridge 4 site on ACP surface (model 2). Different from that of bridge 3 site, deprotonation from bridge 4 site needs higher than 2.12 eV, therefore overpotential for OER is higher than 0.89 V.

5.4 Conclusion

In summary, we report, for the first time, the amorphous cobalt phyllosilicate as an efficient OER catalyst with simple room temperature synthesis and propose its OER mechanism. ACP catalyst performs better than other cobalt based catalysts to evolve oxygen from water. Our DFT calculation suggests that the silicate part – redox inactive part in ACP – aid in substantially reducing the overpotential of catalytic active sites by introducing the modulation of the structure and adopting the structural flexibility. We believe that our findings on this new catalyst material with unexpected chemistry will be helpful for further investigations on efficient catalysts with activity modulation from inactive part.

5.5 References

- (1) Lewis, N. S.; Nocera, D. G. *Proc. Natl. Acad. Sci. U.S.A.* **2006**, *103*, 15729.
- (2) Grätzel, M. *Nature* **2001**, *414*, 338.
- (3) Gust, D.; Moore, T. A.; Moore, A. L. *Acc. Chem. Res.* **2009**, *42*, 1890.
- (4) Swierk, J. R.; Mallouk, T. E. *Chem. Soc. Rev.* **2013**, *42*, 2357.
- (5) Tachibana, Y.; Vayssieres, L.; Durrant, J. R. *Nat. Photonics* **2012**, *6*, 511.
- (6) Kudo, A.; Miseki, Y. *Chem. Soc. Rev.* **2009**, *38*, 253.
- (7) Faunce, T.; Styring, S.; Wasielewski, M. R.; Brudvig, G. W.; Rutherford, A. W.; Messinger, J.; Lee, A. F.; Hill, C. L.; Fontecave, M.; MacFarlane, D. R. *Energy Environ. Sci.* **2013**, *6*, 1074.
- (8) Hurst, J. K. *Science* **2010**, *328*, 315.
- (9) Kanan, M. W.; Nocera, D. G. *Science* **2008**, *321*, 1072.
- (10) Suntivich, J.; May, K. J.; Gasteiger, H. A.; Goodenough, J. B.; Shao-Horn, Y. *Science* **2011**, *334*, 1383.
- (11) Betley, T. A.; Wu, Q.; Van Voorhis, T.; Nocera, D. G. *Inorg. Chem.* **2008**, *47*, 1849.
- (12) Galizzioli, D.; Tantardini, F.; Trasatti, S. *J. Appl. Electrochem.* **1974**, *4*, 57.
- (13) Horkans, J.; Shafer, M. *J. Electrochem. Soc.* **1977**, *124*, 1202.
- (14) Tilley, S. D.; Cornuz, M.; Sivula, K.; Grätzel, M. *Angew. Chem., Int. Ed.* **2010**, *122*, 6549.

- (15) Youngblood, W. J.; Lee, S.-H. A.; Kobayashi, Y.; Hernandez-Pagan, E. A.; Hoertz, P. G.; Moore, T. A.; Moore, A. L.; Gust, D.; Mallouk, T. E. *J. Am. Chem. Soc.* **2009**, *131*, 926.
- (16) Tong, L.; Duan, L.; Xu, Y.; Privalov, T.; Sun, L. *Angew. Chem., Int. Ed.* **2011**, *50*, 445.
- (17) Gorlin, Y.; Jaramillo, T. F. *J. Am. Chem. Soc.* **2010**, *132*, 13612.
- (18) Wang, H.; Lee, H.-W.; Deng, Y.; Lu, Z.; Hsu, P.-C.; Liu, Y.; Lin, D.; Cui, Y. *Nat. Commun.* **2015**, *6*.
- (19) Luo, J.; Im, J.-H.; Mayer, M. T.; Schreier, M.; Nazeeruddin, M. K.; Park, N.-G.; Tilley, S. D.; Fan, H. J.; Grätzel, M. *Science* **2014**, *345*, 1593.
- (20) Kim, J.; Kim, J. S.; Baik, H.; Kang, K.; Lee, K. *RSC Adv.* **2016**, *6*, 26535.
- (21) Lee, S. W.; Carlton, C.; Risch, M.; Surendranath, Y.; Chen, S.; Furutsuki, S.; Yamada, A.; Nocera, D. G.; Shao-Horn, Y. *J. Am. Chem. Soc.* **2012**, *134*, 16959.
- (22) Chemelewski, W. D.; Lee, H.-C.; Lin, J.-F.; Bard, A. J.; Mullins, C. B. *J. Am. Chem. Soc.* **2014**, *136*, 2843.
- (23) Park, J.; Kim, H.; Jin, K.; Lee, B. J.; Park, Y.-S.; Kim, H.; Park, I.; Yang, K. D.; Jeong, H.-Y.; Kim, J. *J. Am. Chem. Soc.* **2014**, *136*, 4201.
- (24) Friebel, D.; Louie, M. W.; Bajdich, M.; Sanwald, K. E.; Cai, Y.; Wise, A. M.; Cheng, M.-J.; Sokaras, D.; Weng, T.-C.; Alonso-Mori, R. *J. Am. Chem. Soc.* **2015**, *137*, 1305.

- (25) Song, F.; Hu, X. *J. Am. Chem. Soc.* **2014**, *136*, 16481.
- (26) Dincă, M.; Surendranath, Y.; Nocera, D. G. *Proc. Natl. Acad. Sci. U.S.A.* **2010**, *107*, 10337.
- (27) Huynh, M.; Bediako, D. K.; Nocera, D. G. *J. Am. Chem. Soc.* **2014**, *136*, 6002.
- (28) Bergmann, A.; Martinez-Moreno, E.; Teschner, D.; Chernev, P.; Gliche, M.; de Araújo, J. F.; Reier, T.; Dau, H.; Strasser, P. *Nat. Commun.* **2015**, *6*.
- (29) Burke, M. S.; Zou, S.; Enman, L. J.; Kellon, J. E.; Gabor, C. A.; Pledger, E.; Boettcher, S. W. *J. Phys. Chem. Lett.* **2015**, *6*, 3737.
- (30) Burke, M. S.; Kast, M. G.; Trotochaud, L.; Smith, A. M.; Boettcher, S. W. *J. Am. Chem. Soc.* **2015**, *137*, 3638.
- (31) May, K. J.; Carlton, C. E.; Stoerzinger, K. A.; Risch, M.; Suntivich, J.; Lee, Y.-L.; Grimaud, A.; Shao-Horn, Y. *J. Phys. Chem. Lett.* **2012**, *3*, 3264.
- (32) Grimaud, A.; May, K. J.; Carlton, C. E.; Lee, Y.-L.; Risch, M.; Hong, W. T.; Zhou, J.; Shao-Horn, Y. *Nat. Commun.* **2013**, *4*.
- (33) Yagi, S.; Yamada, I.; Tsukasaki, H.; Seno, A.; Murakami, M.; Fujii, H.; Chen, H.; Umezawa, N.; Abe, H.; Nishiyama, N. *Nat. Commun.* **2015**, *6*.
- (34) Mefford, J. T.; Rong, X.; Abakumov, A. M.; Hardin, W. G.; Dai, S.; Kolpak, A. M.; Johnston, K. P.; Stevenson, K. J. *Nat. Commun.* **2016**, *7*.

- (35) Gong, M.; Li, Y.; Wang, H.; Liang, Y.; Wu, J. Z.; Zhou, J.; Wang, J.; Regier, T.; Wei, F.; Dai, H. *J. Am. Chem. Soc.* **2013**, *135*, 8452.
- (36) Long, X.; Li, J.; Xiao, S.; Yan, K.; Wang, Z.; Chen, H.; Yang, S. *Angew. Chem., Int. Ed.* **2014**, *126*, 7714.
- (37) Song, F.; Hu, X. *Nat. Commun.* **2014**, *5*.
- (38) Ma, W.; Ma, R.; Wang, C.; Liang, J.; Liu, X.; Zhou, K.; Sasaki, T. *ACS Nano* **2015**, *9*, 1977.
- (39) Liang, H.; Meng, F.; Cabán-Acevedo, M.; Li, L.; Forticaux, A.; Xiu, L.; Wang, Z.; Jin, S. *Nano Lett.* **2015**, *15*, 1421.
- (40) Kanan, M. W.; Yano, J.; Surendranath, Y.; Dincă, M.; Yachandra, V. K.; Nocera, D. G. *J. Am. Chem. Soc.* **2010**, *132*, 13692.
- (41) Bediako, D. K.; Lassalle-Kaiser, B.; Surendranath, Y.; Yano, J.; Yachandra, V. K.; Nocera, D. G. *J. Am. Chem. Soc.* **2012**, *134*, 6801.
- (42) Zaharieva, I.; Chernev, P.; Risch, M.; Klingan, K.; Kohlhoff, M.; Fischer, A.; Dau, H. *Energy Environ. Sci.* **2012**, *5*, 7081.
- (43) Robinson, D. M.; Go, Y. B.; Mui, M.; Gardner, G.; Zhang, Z.; Mastrogiovanni, D.; Garfunkel, E.; Li, J.; Greenblatt, M.; Dismukes, G. C. *J. Am. Chem. Soc.* **2013**, *135*, 3494.
- (44) Grimaud, A.; Carlton, C. E.; Risch, M.; Hong, W. T.; May, K. J.; Shao-Horn, Y. *J. Phys. Chem. C* **2013**, *117*, 25926.

- (45) Stoerzinger, K. A.; Choi, W. S.; Jeon, H.; Lee, H. N.; Shao-Horn, Y. *J. Phys. Chem. Lett.* **2015**, *6*, 487.
- (46) Bediako, D. K.; Surendranath, Y.; Nocera, D. G. *J. Am. Chem. Soc.* **2013**, *135*, 3662.
- (47) Surendranath, Y.; Kanan, M. W.; Nocera, D. G. *J. Am. Chem. Soc.* **2010**, *132*, 16501.
- (48) Ullman, A. M.; Brodsky, C. N.; Li, N.; Zheng, S.-L.; Nocera, D. G. *J. Am. Chem. Soc.* **2016**, *138*, 4229.
- (49) Risch, M.; Klingan, K.; Ringleb, F.; Chernev, P.; Zaharieva, I.; Fischer, A.; Dau, H. *ChemSusChem* **2012**, *5*, 542.
- (50) Farrow, C. L.; Bediako, D. K.; Surendranath, Y.; Nocera, D. G.; Billinge, S. J. *J. Am. Chem. Soc.* **2013**, *135*, 6403.
- (51) Jin, K.; Park, J.; Lee, J.; Yang, K. D.; Pradhan, G. K.; Sim, U.; Jeong, D.; Jang, H. L.; Park, S.; Kim, D. *J. Am. Chem. Soc.* **2014**, *136*, 7435.
- (52) Kim, H.; Park, J.; Park, I.; Jin, K.; Jerng, S. E.; Kim, S. H.; Nam, K. T.; Kang, K. *Nat. Commun.* **2015**, *6*.
- (53) McDonald, A.; Scott, B.; Villemure, G. *Microporous Mesoporous Mater.* **2009**, *120*, 263.
- (54) Alvarez-Ramírez, F.; Toledo-Antonio, J.; Angeles-Chavez, C.; Guerrero-Abreo, J.; López-Salinas, E. *J. Phys. Chem. C* **2011**, *115*, 11442.

- (55) Dumas, A.; Mizrahi, M.; Martin, F. o.; Requejo, F. G. *Cryst. Growth Des.* **2015**, *15*, 5451.
- (56) Domínguez, M.; Taboada, E.; Idriss, H.; Molins, E.; Llorca, J. *J. Mater. Chem.* **2010**, *20*, 4875.
- (57) Trujillano, R.; Lambert, J.-F.; Louis, C. *J. Phys. Chem. C* **2008**, *112*, 18551.
- (58) Melo Jr, M. A.; Airoidi, C. *Dalton Trans.* **2010**, *39*, 10217.
- (59) Pawley, A. R.; Jones, R. L. *Phys. Chem. Miner.* **2011**, *38*, 753.
- (60) Welch, M.; Pawley, A.; Ashbrook, S.; Mason, H.; Phillips, B. *Am. Mineral.* **2006**, *91*, 1707.
- (61) Totir, D.; Mo, Y.; Kim, S.; Antonio, M. R.; Scherson, D. A. *J. Electrochem. Soc.* **2000**, *147*, 4594.
- (62) Subbaraman, R.; Tripkovic, D.; Chang, K.-C.; Strmcnik, D.; Paulikas, A. P.; Hirunsit, P.; Chan, M.; Greeley, J.; Stamenkovic, V.; Markovic, N. M. *Nat. Mater.* **2012**, *11*, 550.
- (63) Koza, J. A.; Hull, C. M.; Liu, Y.-C.; Switzer, J. A. *Chem. Mater.* **2013**, *25*, 1922.
- (64) Smith, R. D.; Prévot, M. S.; Fagan, R. D.; Trudel, S.; Berlinguette, C. P. *J. Am. Chem. Soc.* **2013**, *135*, 11580.
- (65) Bajdich, M.; García-Mota, M.; Vojvodic, A.; Nørskov, J. K.; Bell, A. T. *J. Am. Chem. Soc.* **2013**, *135*, 13521.

- (66) Okubo, M.; Hosono, E.; Kim, J.; Enomoto, M.; Kojima, N.; Kudo, T.; Zhou, H.; Honma, I. *J. Am. Chem. Soc.* **2007**, *129*, 7444.
- (67) Newville, M. *J. Synchrotron Rad.* **2001**, *8*, 322.
- (68) Han, S.-W. *International journal of nanotechnology* **2006**, *3*, 396.
- (69) Han, S.-W.; Stern, E.; Haskel, D.; Moodenbaugh, A. *Physical Review B* **2002**, *66*, 094101.
- (70) Kresse, G.; Furthmüller, J. *Physical review B* **1996**, *54*, 11169.
- (71) Kresse, G.; Joubert, D. *Physical Review B* **1999**, *59*, 1758.
- (72) Dudarev, S.; Botton, G.; Savrasov, S.; Humphreys, C.; Sutton, A. *Physical Review B* **1998**, *57*, 1505.
- (73) Hammer, B.; Hansen, L. B.; Nørskov, J. K. *Physical Review B* **1999**, *59*, 7413.
- (74) García-Mota, M. n.; Bajdich, M.; Viswanathan, V.; Vojvodic, A.; Bell, A. T.; Nørskov, J. K. *J. Phys. Chem. C* **2012**, *116*, 21077.
- (75) Wang, L.; Maxisch, T.; Ceder, G. *Physical Review B* **2006**, *73*, 195107.
- (76) Jain, A.; Hautier, G.; Ong, S. P.; Moore, C. J.; Fischer, C. C.; Persson, K. A.; Ceder, G. *Physical Review B* **2011**, *84*, 045115.
- (77) Chen, J.; Wu, X.; Selloni, A. *Physical Review B* **2011**, *83*, 245204.
- (78) Bajdich, M.; García-Mota, M.; Vojvodic, A.; Nørskov, J. K.; Bell, A. T. *J. Am. Chem. Soc.* **2013**, *135*, 13521.

(79) Rossmeisl, J.; Dimitrievski, K.; Siegbahn, P.; Nørskov, J. K. *J. Phys. Chem.*

C **2007**, *111*, 18821.

Chapter 6. Summary

This thesis mainly relates to the design of polyanion type transition metal oxide materials as energy storage systems such as secondary battery electrodes and water oxidation catalysts. The contents are: (i) Anti-site reordering with charge carrier injection at the LiFePO_4 cathode for Li rechargeable batteries, (ii) a new iron-based mixed phosphate for Li and Na rechargeable batteries Cathode; (iii) the electrochemical mechanism of $\text{Na}_4\text{Fe}_3(\text{PO}_4)_2(\text{P}_2\text{O}_7)$ in Na rechargeable batteries; and (iv) amorphous cobalt phyllosilicate with layered crystal motifs as the water oxidation catalyst.

In the first part of this dissertation, I introduced a new method to reduce crystal defects with a case study of olivine LiFePO_4 . The defect elimination mechanism was proposed from the first principle calculation. This indicated that the introduction of vacancies and excess charge carriers reduces the activation barrier of defect recombination. We have demonstrated that this new method can be used to "heal" defective LiFePO_4 containing both micro- and nano-sized particles. The defect extinction mechanism suggested here is widely applicable to the production of defect free materials and is expected to help understanding the defect behavior of various materials.

In the second part of this paper, a new mixed polyanionic compound $\text{Li}_x\text{Na}_{4-x}\text{Fe}_3(\text{PO}_4)_2(\text{P}_2\text{O}_7)$ ($x = 0, 3$) was proposed as a new promising electrode for Li and Na secondary batteries. I have shown that the combination of $(\text{PO}_4)^{3-}$

and $(\text{P}_2\text{O}_7)^{4-}$ polyanion groups and low cost transition metal of Fe can provide a new crystal framework with promising electrochemical properties. This study suggests that there is an important opportunity to explore new low cost, high performance electrodes in mixed polyanion materials.

In the third part, structural evolution of $\text{Na}_{4-x}\text{Fe}_3(\text{PO}_4)_2(\text{P}_2\text{O}_7)$ during charge/discharge was examined by experiments and first-principles calculations. I revealed that the electrode operates *via* a one-phase reaction with a reversible structural evolution that includes P_2O_7 distortion. Furthermore, the structural stability of partially desodiated phases at high temperature was examined.

In the final part, I proposed that the amorphous cobalt phyllosilicate as an efficient OER catalyst with simple room temperature synthesis and propose its OER mechanism. ACP catalyst performs better than other cobalt based catalysts to evolve oxygen from water. My DFT results suggest that the silicate part – redox inactive part in ACP – aid in substantially reducing the overpotential of catalytic active sites by introducing the modulation of the structure and adopting the structural flexibility. I believe that the findings on this new catalyst material with unexpected chemistry will be helpful for further investigations on efficient catalysts with activity modulation from inactive part.

Abstract in Korean

초 록

에너지 수요가 끊임없이 증가하고 화석 연료가 고갈되면 대체 에너지원 개발이 가속화되고 있다. 증가하는 에너지 요구에 대처하고 지속 가능한 에너지를 제공하기 위해, 대형 에너지 저장 시스템은 최근 몇 년간 중요한 연구 분야가 되었다. 다양한 에너지 저장 시스템 후보 중에서 화학 에너지 저장 시스템은 공해없는 작동, 높은 효율, 긴주기 수명, 낮은 유지 비용, 다양한 수요를 충족시키는 유연한 전력 및 에너지 특성으로 인해 이러한 응용 분야에 최적의 선택으로 간주된다. 이러한 맥락에서, 에너지저장소재를 위한 새로운 소재의 개발은 중요한 연구이다. 본 연구에서는 에너지저장소재를 위한 더 나은 재료를 위해, 우수한 특성을 지닌 새로운 다중산 이온계 전이금속 화합물에 대한 연구를 진행하였다.

제 2 장에서는 상온에서 전기 화학적 전하 캐리어 주입 공정을 사용하여 리튬 이온 배터리 (LIB) 용 올리빈 결정의 안티 사이트 결함을 제거하는 새로운 방법을 소개한다. 올리빈의 안티 사이트 결함은 Li / Fe 안티 사이트의 전기 화학적 재조합에 의해 효과적으로 감소되었다. 올리빈의 치유된 결정 구조는 용량과 고전력 기능을 회복하였다.

제 3 장에서는 소듐 이온 배터리를 위한 새로운 철 기반 혼합 다중산 이온계 화합물인 $\text{Na}_4\text{Fe}_3(\text{PO}_4)_2(\text{P}_2\text{O}_7)$ 를 소개한다. 3 차원 Na 이동 경로를 갖는 신규 화합물의 구조적 특성 분석은 X 선 및 중성자 회절 연구를 사용하여 수행되었다. 전극은 평균 전위 ~ 3.2V (Na + / Na 대비)와 320 Wh^{-1} 의 에너지 밀도를 보였다. 또한

리튬 이온 전지에서 $\text{Li}_3\text{NaFe}_3(\text{PO}_4)_2(\text{P}_2\text{O}_7)$ 이온 교환 시료를 사용하여 가역 전극 운전을 수행 하였다. 전극은 평균 전압 3.4V (Li^+ / Li)의 이론 용량 ($\sim 140 \text{ mAh g}^{-1}$)의 약 92 %를 보였다. 이 연구는 최초로 $(\text{PO}_4)^{3-}$ 및 $(\text{P}_2\text{O}_7)^{4-}$ 다중산 이온 조합에 의해 높은 전기 화학적 성능을 갖는 소듐 이온 배터리를 위한 새로운 오픈 프레임 워크 전극을 제안했다.

제 4 장에서, 제일원리계산과 실험을 사용하여 소듐 이온 배터리 소재인 $\text{Na}_x\text{Fe}_3(\text{PO}_4)_2(\text{P}_2\text{O}_7)$ ($1 \leq x \leq 4$)의 전기 화학적 메커니즘을 소개한다. 본 연구에서는 $\text{Na}_x\text{Fe}_3(\text{PO}_4)_2(\text{P}_2\text{O}_7)$ 전극의 충방전이 가역적인 $\text{Fe}^{2+}/\text{Fe}^{3+}$ 산화 환원 반응을 수반하는 단일상 반응을 통해 일어난다는 것을 발견했다. 전극은 전기 화학 사이클 동안 4 % 미만의 매우 작은 부피 변화를 수반하며, 이것은 구조에서 유연한 P_2O_7 이합체를 갖는 다중 음이온 화합물의 개방된 구조에 기인한다. $\text{NaFe}_3(\text{PO}_4)_2(\text{P}_2\text{O}_7)$ 의 구조 변화는 Na의 삽입탈리반응의 속도를 늦춰 Na의 불완전한 사용을 초래하나 (이론 용량의 $\sim 82 \%$), 높은 파워밀도가 C/20 부터 C/5 까지 확인되었다. 또한 20 사이클까지 안정하게 유지 되었다. 실시간 X 선 회절과 시차 주사 열량계를 이용하여 부분 충전된 전극인 $\text{Na}_x\text{Fe}_3(\text{PO}_4)_2(\text{P}_2\text{O}_7)$ ($1 \leq x \leq 4$)가 530 °C까지 열적으로 안정함을 확인하였다. 본 연구의 $\text{Na}_x\text{Fe}_3(\text{PO}_4)_2(\text{P}_2\text{O}_7)$ ($1 \leq x \leq 4$)의 전기 화학적 메커니즘 이해는 향후 이 소재의 최적화 방향을 제시할 것으로 보인다.

제 5 장에서, 간단한 실온 침전에 의해 제조 된 층상 결정 모티프를 갖는 비정질의 코발트 필로실리케이트를 수소 연료용 새로운 OER 촉매로 소개한다. 이 물질은 코발트계 촉매 중에서 장기간 안정성 뿐만 아니라 현저히 낮은 과전압 (η)을 나타낸다. X 선 흡수 분광학 및 푸리에 변환 적외선 스펙트럼을 기반으로 한 구조 조사는 규산염 층이 전기 분해 후에 구조를 유지함을 보였다. 또한, 제일원리계산은 CoOOH 에서와 유사한 ACP의 층상 결정

모티프가 OER 메커니즘을 담당함을 나타내었다. 그러나 활성 부위의 환경은 실리케이트 그룹에 의해 크게 조절되어 과전압의 감소를 가져온다. 이 연구는 필로 실리케이트의 새로운 물질 그룹이 효율적인 OER 촉매가 될 수 있으며 산화 환원 불활성 그룹을 제어함으로써 촉매 활성을 조정하면 새로운 고성능 촉매의 설계 방향을 모색 할 수 있음을 제안한다.

주요어: 에너지 저장 소재, 리튬이온전지, 소듐이온전지, 촉매, 제일원리계산, 다중산 이온

학번 : 2012-30157